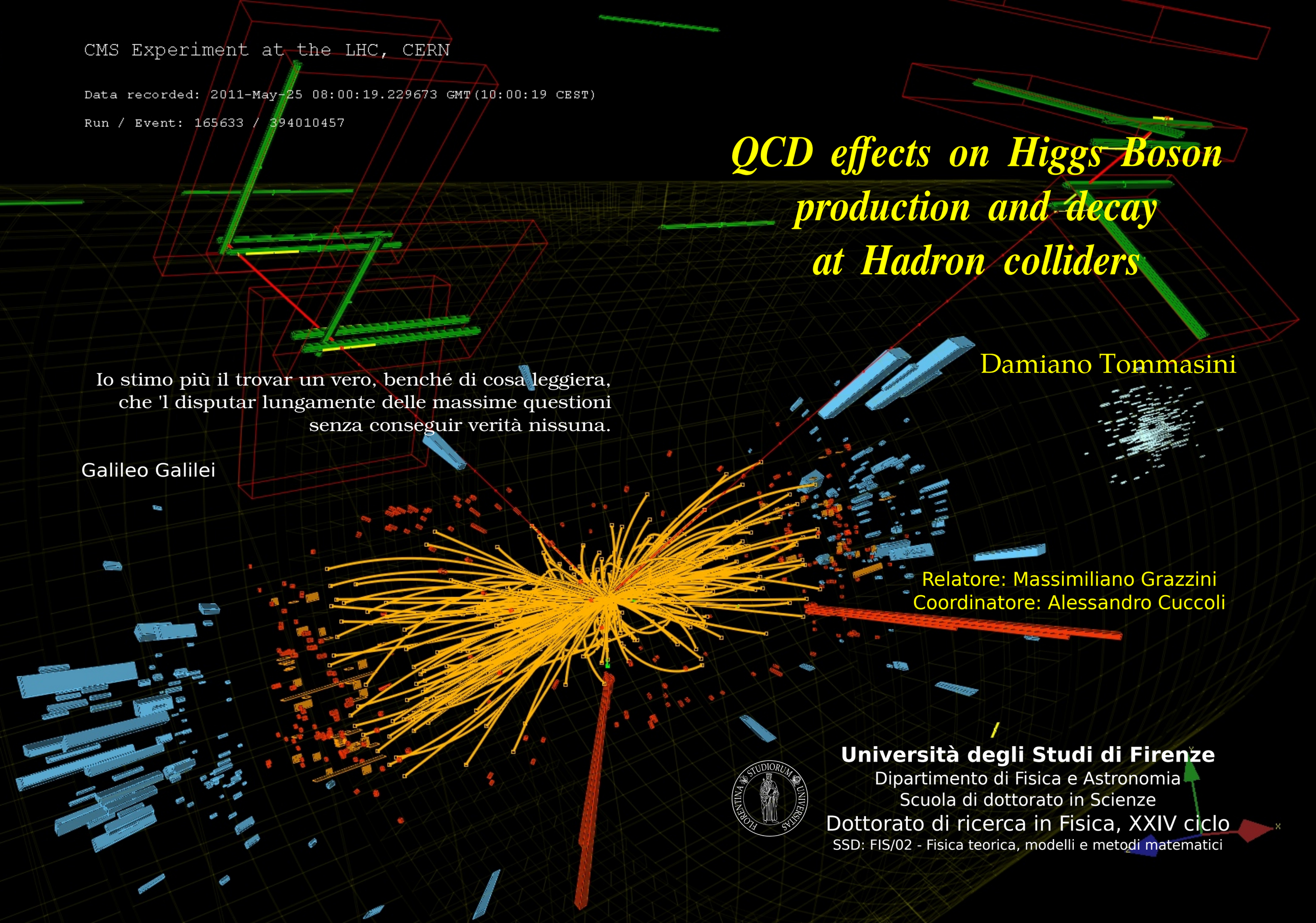

QCD effects on Higgs Boson production and decay at Hadron colliders

Damiano Tommasini

Io stimo più il trovar un vero, benché di cosa leggiera,
che 'l disputar lungamente delle massime questioni
senza conseguir verità nissuna.

Galileo Galilei

Relatore: Massimiliano Grazzini
Coordinatore: Alessandro Cuccoli

Università degli Studi di Firenze
Dipartimento di Fisica e Astronomia
Scuola di dottorato in Scienze
Dottorato di ricerca in Fisica, XXIV ciclo
SSD: FIS/02 - Fisica teorica, modelli e metodi matematici

UNIVERSITÀ DEGLI STUDI FIRENZE
Dipartimento di Fisica e Astronomia

QCD effects on Higgs Boson production and decay at Hadron colliders

Tesi di Dottorato

Damiano Tommasini

Tutor:
Dr. Massimiliano Grazzini

Coordinatore:
Prof. Alessandro Cuccoli

Scuola di Dottorato in Scienze
Dottorato di Ricerca in Fisica, XXIV ciclo
Settore disciplinare: FIS/02 - Fisica teorica, modelli e metodi matematici

Gennaio 2012

Alla mia famiglia
e a tutte le persone che mi vogliono bene...

Contents

Introduction **iii**

1 Overview on the Standard Model **1**
1.1 Main features of the Standard Model 1
1.2 Spontaneous symmetry breaking and the Higgs boson 4
1.3 Experimental validations of the Standard model and status of the Higgs boson searches 6

2 Perturbative QCD at hadron colliders **11**
2.1 Redundant degrees of freedom in the SM Lagrangian and gauge fixing . . 11
2.2 Ultraviolet divergences, renormalization and running coupling constant . . 12
2.3 Perturbation theory at high energies 15
2.4 Infrared divergences and their cancellation 16
2.5 Deep inelastic scattering and hadron collisions 19
2.6 DGLAP evolution equation and splitting functions 21

3 Higgs boson at hadron colliders **25**
3.1 Factorisation of the Higgs production and decay partonic cross section . . 25
3.2 Higgs production mechanisms at hadron colliders 27
3.2.1 Gluon-gluon fusion process 27
3.2.2 Overview on other Higgs production channels 33
3.3 Higgs boson decay modes 35
3.4 Main search strategies at hadron colliders 38

4 Transverse momentum spectrum of the Higgs boson **41**
4.1 Production: rapidity and PDFs 43
4.2 Production: transverse momentum spectrum 45
4.3 Fixed order failure in the low q_T region 47
4.4 Resummation: general features 49

4.5 Transverse momentum resummation . . . 51
4.6 Process-independent transverse momentum resummation . . . 54
4.7 Small and large b region, q_T integrated cross section and non perturbative effects . . . 58
4.8 Double differential cross section: q_T resummation and rapidity dependence 61
4.9 Decay products: rapidity, transverse momenta and experimental acceptances . . . 63

5 Resummed q_T spectrum of the Higgs boson: HqT predictions 65
5.1 Mellin transform of the hard coefficients $\mathcal{H}^{H,(2)}$ . . . 66
5.2 The q_T spectrum of the Higgs boson at the Tevatron and the LHC . . . 68
5.3 Perturbative uncertainties of the Higgs q_T spectrum . . . 70
5.3.1 Separate contributions of scale uncertainties . . . 71
5.3.2 Total perturbative uncertainties of the q_T spectrum . . . 73
5.3.3 Shape uncertainty, Non Perturbative effects and PDFs dependence of the Higgs q_T spectrum . . . 76
5.4 Monte Carlo event generators and QCD corrections: the reweighting technique . . . 78
5.5 Switching in the q_T distribution between resummed and fixed order predictions . . . 80

6 Higgs boson signals in the electroweak decay channels 83
6.1 $H \to \gamma\gamma$ decay channel . . . 85
6.2 $H \to WW \to l\nu l\nu$ decay channel . . . 88
6.3 $H \to ZZ \to 4l$ decay channels . . . 91

Conclusion 95

A Acronyms 97

B Hard coefficients $\mathcal{H}_{gg}^{H,(2)}$ 99

Bibliography 101

Cover image 111

Ringraziamenti 113

Introduction

The Standard Model (SM) of particle physics is a $G = SU(3)_C \times SU(2)_I \times U(1)_Y$ gauge theory that describes the strong and electroweak interactions of the known subatomic particles at an impressive level of accuracy. The validity of the SM has been established during the last 30 years. The experimental facilities that played a major role in validating the model are SPS at CERN, where the W and Z bosons were first observed, HERA, where the proton structure was studied in detail, LEP and SLC, where accurate tests of the SM were performed, and the Fermilab Tevatron, where the top quark was discovered.

Despite its success, the SM has some well known problems. In particular the mechanism that gives masses to the particles remains to be understood. Gauge boson mass terms are forbidden because they violate gauge invariance. Moreover, contrary to what happens in vector theories like QED and QCD, also fermion mass terms are not permitted: the $SU(2) \times U(1)$ electroweak sector is in fact a *chiral* theory: left and right handed fermions couple differently to the gauge group. The most accepted/accredited solution to this problem is based on the concept of Spontaneous Symmetry Breaking mechanism (SSB), which is borrowed from statistical mechanics. Through SSB the Lagrangian remains gauge invariant but the gauge symmetry is broken by the vacuum.

There are several possibilities to realize SSB: the standard one, which is implemented in the minimal version of the SM, is to introduce a complex scalar $SU(2)$ doublet endowed with a symmetry breaking potential. Three out of the four degrees of freedom go to give mass to the W and Z bosons, leaving the photon massless, and the fourth remains in the spectrum and is the so called Higgs boson [1]. More involved models imply the existence of more than one Higgs doublet, and thus more than one Higgs boson exist in the spectrum. It is clear that such Higgs boson(s) plays a central role in giving masses and couplings to SM particles, therefore the corresponding experimental search is one of the most important tasks of modern high energy particle physics. In the minimal version of the SM, on which we will focus in this thesis, the important unknown parameter is the Higgs boson mass M_H, which, together with fermion masses, completely determine the Higgs sector.

Even if the Higgs boson is not yet observed, if it exists, it must manifest itself in loop corrections. In particular, it will affect the self energies of the W and Z bosons, and thus precision electroweak data provide indirect information on the Higgs mass, as it happened for the top quark. As a consequence, a precise knowledge of the electroweak parameters (such as gauge boson masses M_W, M_Z, Weinberg angle θ_w), can be used to constrain the Higgs mass. The top mass appears quadratically in the radiative contributions. For this reason the top mass was predicted with good precision before its discovery. Unfortunately the Higgs mass enters only logarithmically at one-loop order, and it is difficult to obtain stringent constraints. The present electroweak data [2] suggest that the Higgs boson should be light ($M_H \lesssim 200$ GeV).

Up to now the Higgs boson has not yet been observed. LEP experiments have put a lower limit to the Higgs mass at $M_H > 114.4$ GeV [2]. Tevatron experiments recently excluded the SM Higgs in the mass region 156 GeV $< \mathrm{M_H} <$ 177 GeV and $M_H < 108$ GeV [3]. Higgs searches are being currently carried out at the ATLAS and CMS experiments at the LHC; their preliminary combined results exclude at 95% CL a SM Higgs boson in the mass range 141 GeV $< \mathrm{M_H} <$ 476 GeV [4]. Very recently (13 December 2011), in a seminar held at CERN, the ATLAS and CMS experiments presented the status of their searches for the Standard Model Higgs boson [5]. The main conclusion is that the Standard Model Higgs boson is most likely to have a mass constrained to the range $116 - 130$ GeV by ATLAS and $115 - 127$ GeV by CMS. Some excesses have been seen by both experiments in the mass region around 125 GeV, but these are not yet strong enough to claim a discovery.

The main production mechanism of the SM Higgs boson at hadron colliders is the gluon-gluon fusion process. At the leading order (LO) in the QCD perturbative expansion the process occurs through a heavy-quark loop [6]. The computation of QCD radiative corrections is important to have a reliable estimate of the production rate, but it is complicated since already at next-to-leading corrections (NLO) it involves the evaluation of two-loop diagrams. Despite this fact, the NLO corrections to the total cross section have been computed already about 20 years ago [7, 8, 9] and found to be very large (80-100%), thus casting doubts on the reliability of the perturbative expansion. In the past ten years the next-to-next-to-leading order (NNLO) has been computed [10, 11, 12, 13, 14, 15] and the corrections turn out to be moderate (10-25% at LHC); thus, now, the predictions for the total cross section appear to be under control.

The decay of the Higgs boson is driven by the strength of its interaction with other particles, that grows with the particle mass itself. Thus the decay into heavy particles ($W^{\pm}, Z^0, t, b$) will be dominant when kinematically allowed. Unfortunately QCD backgrounds may give the same observable final state. In order to distinguish Higgs

boson events from the background, a good knowledge of both signal and background cross sections is needed, and this applies not only to total rates, but also to differential distributions.

One of the most important distribution in Higgs boson production is the transverse-momentum (q_T) spectrum of the Higgs boson. A precise knowledge of this observable can help to improve and optimise the search strategies and the statistical significance in the data analysis.

The first part of my PhD activity was mostly devoted to the study of this distribution in QCD perturbation theory. To study the transverse momentum distribution for Higgs production, it is convenient to separate the q_T spectrum in the high ($q_T \sim M_H$) and small ($q_T \ll M_H$) regions. In the large-q_T region, the perturbative expansion is controlled by the small expansion parameter $\alpha_s(M_H^2)$, and the calculations based on the truncation of the series at a fixed-order in α_s are theoretically justified. Here perturbative fixed-order predictions are available up to NLO. The bulk of events, however, is expected to lie in the small transverse momentum region, where the emission of collinear and soft radiation from incoming partons enhances the coefficients of the perturbative expansion by powers of the logarithmic terms $\ln\left(M_H^2/q_T^2\right)$. Therefore $\alpha_s(M_H^2)\ln\left(M_H^2/q_T^2\right) \sim 1$ and the validity of the perturbative expansion is spoiled. To solve this problem, the logarithmic terms have to be resummed to all orders in α_s. For the Higgs boson, this resummation has been explicitly done up to the next-to-leading-logarithms (NLL) [16] and the next-to-next-to-leading-logarithms (NNLL)[17, 18, 19, 20, 21]. In order to obtain a reliable theoretical prediction over the entire transverse momentum spectrum, the resummed and fixed order calculations have to be consistently matched, to avoid double counting. Such a calculation up to NNLL+NLO has been performed, and is implemented in the code named `HqT` [22]. This program provides the most advanced perturbative information available at present for this observable and, for this reason, it is currently used to correct (reweight) the transverse momentum spectrum generated with Monte Carlo event simulations in the Tevatron and the LHC analysis. In the first version of `HqT` an approximation is used in the resummed component at NNLL accuracy. We have made available a new updated version of the code named `HqT2.0` [23] that implements the exact expressions of the coefficients controlling the resummation at full NNLL accuracy.

The results of perturbative QCD computations at hadron colliders usually depend on two unphysical scales, the renormalization and factorization scales. The central values of these scales are chosen to be the hard scale of the process, and variations of the scales around the central value are used to estimate perturbative uncertainties. In the new version of `HqT`, besides the usual dependence on renormalization and factorization scales, we have also implemented the exact dependence on an auxiliary scale (*resummation*

scale) introduced through the resummation procedure. Independent variations of these three scales allow a more reliable assessment of the theoretical uncertainties affecting the resummed Higgs transverse momentum spectrum.

The program `HqT` computes the inclusive transverse momentum spectrum of the Higgs boson, but such spectrum is not directly measurable at the experiments. In fact, the Higgs boson is an unstable particle that (after its production) will decay into the final state that will be observed in the detectors. It is thus important to extend the program `HqT` to include the most relevant Higgs decay modes. The second part of my PhD activity is devoted to the inclusion of such decays, in particular the decay into two photons and into WW and ZZ to leptons. These decays are the most useful for the Higgs boson searches in the gluon fusion production mode, because they are expected to provide the most clear signatures in the detectors. The calculations of such decays can be implemented in an extension of `HqT` that allows us to retain the full kinematical information of the decay products. In particular I worked to obtain such program that allows to apply arbitrary cuts on the momenta of the final particles. This is essential in order to correctly take into account the effects of the geometrical acceptances of the detectors.

This thesis is organized in two main parts.

The *first part* is a general introduction on high energy physics with particular emphasis on Higgs physics. In Chapter 1, I will give a concise review of the Standard Model, with particular emphasis on the Spontaneous Symmetry Breaking mechanism and the Higgs field. Then in Chapter 2, I will discuss some technical aspects concerning the Standard Model, perturbation theory and the parton model. In Chapter 3, I will treat the general features of Higgs boson production and decay at hadron colliders and the related search strategies. Then in Chapter 4, I will discuss the most relevant differential distributions concerning Higgs boson production and decay, with particular emphasis on the fixed order failure in describing the small transverse momentum region and the all-order resummation of the logarithmically enhanced terms that spoil the convergence of the fixed order expansion.

The *second part* of this thesis the main results of my work are presented. In Chapter 5, I discuss the upgrade of `HqT` and the related phenomenological studies. In Chapter 6, I present the new code `HRes` that includes the Higgs decay in the di-photon and four-leptons channels, with detailed studies of observables on the Higgs decay products.

In Appendix A, I report the list of acronyms used in the thesis and in Appendix B the explicit expression of the coefficients entering transverse momentum resummation at NNLL accuracy.

The results presented in this thesis are the subject of two publications. The predictions for the Higgs boson transverse momentum spectrum and detailed study on the theoretical uncertainties are presented in

Transverse-momentum resummation: Higgs boson production at the Tevatron and the LHC, Daniel de Florian, Giancarlo Ferrera, Massimiliano Grazzini, Damiano Tommasini; **JHEP** 1111 (2011) 064, arXiv:hep-ph/1109.2109.

A detailed analysis of the impact of transverse momentum resummation in the Higgs boson production and decay will be presented in a forthcoming paper:

Transverse momentum resummation for Higgs boson production and decay, Daniel de Florian, Giancarlo Ferrera, Massimiliano Grazzini, Damiano Tommasini, in preparation[1].

[1] **PS**: the final published paper is *Higgs boson production at the LHC: transverse momentum resummation effects in the H->2gamma, H->WW->lnu lnu and H->ZZ->4l decay modes.*, Daniel de Florian, Giancarlo Ferrera, Massimiliano Grazzini, Damiano Tommasini; **JHEP** 1206 (2012) 132, arXiv:hep-ph/1203.6321.

Chapter 1

Overview on the Standard Model

The mathematical framework for describing the physics of subatomic particles is provided by relativistic quantum field theory. Using this framework, we can properly describe the elementary particles and their interactions combining the features of quantum mechanics and special relativity. In order to describe the interactions and the field dynamics we introduce the gauge principle: a gauge theory is a field theory in which the Lagrangian is invariant under a continuous group of local transformations; for each group generator there is a corresponding gauge field. Gauge theories can be spontaneously broken: in this case the local symmetry of the Lagrangian is preserved, but it is broken by the vacuum, and thus it is not respected in the spectrum of the physical states.

Among the models that it is possible to build using the framework of relativistic quantum field theory, gauge principle and SSB, an excellent description of available data is provided by the so called *Standard Model of elementary particles* (SM). In this chapter I will give a short overview of the Standard Model [24, 25, 26, 27, 28, 29, 30] with particular emphasis on the SSB mechanism leading to the Higgs boson [1, 31, 32, 33].

1.1 Main features of the Standard Model

The Standard Model of elementary particles is a non-abelian gauge theory based on the symmetry group $SU(3)_C \times SU(2)_I \times U(1)_Y$. The subscripts stand for Colour, Isospin and Hypercharge, respectively, and the related gauge fields are eight gluons interacting with the $SU(3)_C$ colour quantum number, three weak fields interacting with the $SU(2)_I$ isospin quantum number and an abelian field that interacts with the $U(1)_Y$ weak hypercharge.

The matter fields consist of three generations of fermions together with their corresponding antiparticles: $(e, \bar{\nu}_e, u, d)$, $(\mu, \bar{\nu}_\mu, c, s)$ and $(\tau, \bar{\nu}_\tau, t, b)$; for each fermion generation there are one charged lepton, one neutrino, one positive-charged quark and one negative-charged quark.

The group $SU(3)_C$ is the gauge group of the Quantum Chromo Dynamics (QCD), i.e. the strong interacting sector of the SM. The QCD Lagrangian density is

$$\mathcal{L}_{QCD} = -\frac{1}{4}F^a_{\mu\nu}F^{a\mu\nu} + i\sum_r \bar{q}^{\mathtt{i}}_{r\alpha}\,(\gamma^\mu)^\alpha_\beta (D_\mu)_{\mathtt{ij}}\, q^{\mathtt{j}\beta}_r + h.c., \tag{1.1}$$

where $q^{\mathtt{i}}_{r\alpha}$ are the quark fields, r is the quark flavour index ($r = 1, 2, 3$), $\mathtt{i}, \mathtt{j}$ are the colour indices in the fundamental representation of the group $SU(3)_C$, the greek indices α, β, μ are Lorentz indices, γ^μ are the Dirac matrices defined by the relation $\{\gamma^\mu, \gamma^\nu\} = 2g^{\mu\nu}$ and $g^{\mu\nu}$ is the metric tensor. The field strenght tensor $F^a_{\mu\nu}$ for the gluon field G^a_μ is

$$F^a_{\mu\nu} = \partial_\mu G^a_\nu - \partial_\nu G^a_\mu - g_s f_{abc} G^b_\mu G^c_\nu, \tag{1.2}$$

where $a = 1, \ldots, 8$ is the colour index in the adjoint representation of the group $SU(3)_C$, g_s is the QCD coupling constant and the constants f_{abc} are the structure constants of $SU(3)$ and define the Gell-Mann matrices λ_a

$$[\lambda_a, \lambda_b] = 2i f_{abc}\lambda_c. \tag{1.3}$$

In the Lagrangian (1.1), the quadratic term in the field tensor leads to three and four-point gluon self-interactions whereas the covariant-derivative

$$(D_\mu)_{\mathtt{ij}} = \delta_{\mathtt{ij}}\partial_\mu + i g_s G^a_\mu (\lambda_a/2)_{\mathtt{ij}} \tag{1.4}$$

leads the quark-gluon interactions.

The group $SU(2)_I \times U(1)_Y$ is the gauge group of the electroweak sector (EW), which has a Lagrangian density

$$\mathcal{L}_{EW} = -\frac{1}{4}B_{\mu\nu}B^{\mu\nu} - \frac{1}{4}W^i_{\mu\nu}W^{i\mu\nu} + i\sum_r \left(\overline{\psi}^r_L\,\gamma_\mu D^\mu_L\,\psi^r_L + \overline{\psi}^r_R\,\gamma_\mu D^\mu_R\,\psi^r_R\right) + h.c.; \tag{1.5}$$

from now on, for simplicity, we omit the Lorentz and colour indices in the fermion fields ψ. $W^i_{\mu\nu}, B_{\mu\nu}$ are the field strength tensor for the W^i_μ Weak Isospin and B_μ Hypercharge gauge fields ($i = 1, 2, 3$) and now r is the fermion family index ($r = 1, 2, 3$)

$$B_{\mu\nu} = \partial_\mu B_\nu - \partial_\nu B_\mu, \tag{1.6}$$

$$W^i_{\mu\nu} = \partial_\mu W^i_\nu - \partial_\nu W^i_\mu - g\epsilon_{ijk}W^j_\mu W^k_\nu, \tag{1.7}$$

where g is the $SU(2)$ gauge coupling and ϵ_{ijk} is the fully antisymmetric tensor.

A relevant feature of the electroweak sector is the fact that it is a chiral theory, that is fermions couple differently in their right-handed and left-handed components; they transform as singlets and doublets under $SU(2)_I$, respectively, and they have different $U(1)_Y$

charges. By the use of $\gamma^5 \equiv i\gamma^0\gamma^1\gamma^2\gamma^3$, one can define the left and right components of the fermionic fields

$$\psi_L \equiv \frac{1-\gamma^5}{2}\psi \qquad \psi_R \equiv \frac{1+\gamma^5}{2}\psi \tag{1.8}$$

and one can construct the weak-isospin left doublets: lepton L_L and quark Q_L,

$$L_L = \begin{pmatrix} (\nu_l)_L \\ l_L \end{pmatrix} \qquad Q_L = \begin{pmatrix} q_L^+ \\ \hat{q}_L^- \end{pmatrix}, \tag{1.9}$$

where the index l runs over the leptons e, μ, τ, the index q^+ runs over the positive-charged quarks u, c, t and $\hat{q}^-$ over d, s, b (the negative-charged ones). The negative-charged quarks are expressed in the electroweak basis ($\hat{q}$) that is connected to the mass eigenstates basis (q) via the CKM matrix V ($\hat{q}_i = V_{ij}q_j$).

Experimentally we know that all the left-handed fermions have a right-handed counterpart, except neutrinos [34, 30].

The interactions between fermions and vector fields are now incorporated in the theory generalizing the covariant derivative (1.4), including the terms related to the various gauge groups

$$D_{L\mu} = \partial_\mu + ig_s G_\mu^a \frac{\lambda^a}{2} + igT^i W_\mu^i + ig'\frac{Y}{2}B_\mu, \tag{1.10}$$

$$D_{R\mu} = \partial_\mu + ig_s G_\mu^a \frac{\lambda^a}{2} + ig'QB_\mu, \tag{1.11}$$

where T^i, Y are the generators of $SU(2), U(1)$ respectively with couplings g, g' and $Q = T_3 + \frac{Y}{2}$ is the electric charge in units of $(-e)$, T_3 is the third component of the weak-isospin and Y the hypercharge.

A peculiar property of the electroweak $SU(2)\times U(1)$ group is the fact that the physical gauge bosons we observe experimentally are mixture of the electroweak eigenstates W^i, B: the vector bosons $Z^0, W^\pm$ and A (the photon). They are given by the following linear combinations

$$W_\mu^\pm = \frac{W_\mu^1 \mp iW_\mu^2}{\sqrt{2}}, \tag{1.12}$$

$$Z_\mu^0 = \cos\theta_w W_\mu^3 - \sin\theta_w B_\mu, \tag{1.13}$$

$$A_\mu = \sin\theta_w W_\mu^3 + \cos\theta_w B_\mu, \tag{1.14}$$

where θ_w is the Weinberg mixing angle ($\theta_w \equiv \arctan\frac{g'}{g}$) and $e = g\sin\theta_w$ is the electromagnetic coupling.

1.2 Spontaneous symmetry breaking and the Higgs boson

Defining the SM Lagrangian by combining the EW and QCD Lagrangian, we obtain

$$\mathcal{L} = -\frac{1}{4}B_{\mu\nu}B^{\mu\nu} - \frac{1}{4}W^i_{\mu\nu}W^{i\mu\nu} - \frac{1}{4}F^a_{\mu\nu}F^{a\mu\nu} + i\sum_r \left(\overline{\psi}^r_L\,\gamma_\mu D^\mu_L\,\psi^r_L + \overline{\psi}^r_R\,\gamma_\mu D^\mu_R\,\psi^r_R\right) + h.c. \tag{1.15}$$

With this Lagrangian, it is possible to obtain interaction vertices and particle propagators that are needed to calculate scattering amplitudes in high energy interactions.

At this level, all fields representing different types of particles are treated as massless. However, from the experiments, we have definitive evidence that all the fermions and the $W^\pm, Z^0$ bosons are massive. On the other hand, we can not directly include mass terms in the Lagrangian. For example, if we introduce in the Lagrangian naive gauge boson mass terms of the type $m^2 B_\mu B^\mu$, we explicitly violate even the simplest $U(1)$ gauge symmetry. Furthermore, as we discussed above, the theory is chiral, while a fermionic mass term is of the form $m(\bar{\psi}_L\psi_R + \bar{\psi}_R\psi_L)$. This term mixes fermions of different chirality and thus it is not allowed. In both the cases, an explicit mass term is forbidden in the theory.

The solution to this problem is provided by the SSB mechanism. This mechanism is realised when, given a symmetry of the Lagrangian, the ground state is not invariant under the action of this symmetry. Historically, the concept of SSB first emerged in the theory of ferromagnets. Although the theory is rotationally invariant by hypothesis, below the critical Curie temperature T_C the ground state has the spins all aligned along some particular direction, thus not respecting the initial rotational symmetry. The same picture can be generalized to quantum field theory (QFT), with the ground state becoming the vacuum state[1].

In the minimal version of the SM the SSB is achieved as follows. We introduce a new field Φ whose dynamic is described by the Lagrangian

$$\mathcal{L}_\Phi = (D_\mu\Phi)^\dagger(D^\mu\Phi) - V(\Phi), \tag{1.16}$$

where the potential $V(\Phi)$ is chosen to be gauge invariant, but with a minimum which breaks the symmetry, i.e. despite we preserve the gauge invariance of the Lagrangian at the same time the vacuum is not invariant under the symmetry group.

In the SM, Φ is a doublet of complex fields with four new degrees of freedom, which can be parametrized as follows

$$\Phi \equiv \frac{1}{\sqrt{2}}\begin{pmatrix}\phi_1 + i\phi_2\\ \phi_3 + i\phi_4\end{pmatrix}; \tag{1.17}$$

the covariant derivative takes into account the EW interaction terms

$$D_\mu \;=\; \partial_\mu - igT^iW^i_\mu - ig'\frac{Y}{2}B_\mu \tag{1.18}$$

[1]It is well known that there is a formal analogy between statistical mechanics and QFT.

and the potential of the Higgs self-interactions is

$$V(\Phi) = \lambda(\Phi^\dagger\Phi)^2 - \mu^2\Phi^\dagger\Phi; \tag{1.19}$$

if the parameters μ^2, λ are positive, this potential has a classical minimum which is not $|\Phi| = 0$: we obtain a circle of degenerate minima $|\Phi| = \sqrt{\frac{\mu^2}{2\lambda}} \equiv \frac{v}{\sqrt{2}}$ leading to an infinite number of degenerate ground states. By choosing as ground state:

$$\langle\Phi\rangle \equiv \frac{1}{\sqrt{2}}\begin{pmatrix}0\\v\end{pmatrix} \tag{1.20}$$

the $SU(2)_I \times U(1)_Y$ symmetry is spontaneously broken (with $U(1)_{em}$ symmetry left over) and the field Φ can be parametrized in terms of the the Higgs field H, as follows (in the unitary gauge)

$$\Phi \equiv \frac{1}{\sqrt{2}}\begin{pmatrix}0\\v+H\end{pmatrix}. \tag{1.21}$$

Now writing down the explicit expression obtained substituting the covariant derivative Eq. (1.18) in the kinetic part of Lagrangian Eq. (1.16) and applying the linear transformation of Eq. (1.14) on the vector boson fields, we obtain a sum of terms as $2\mu^2H^2$, $\frac{1}{4}g^2v^2W_\mu W^\mu$ or $\frac{g^2}{2}H^2Z_\mu Z^\mu$ and so on. These terms can be interpreted as mass terms for the particles and interactions with the Higgs boson. In this procedure, three degrees of freedom in (1.17) are absorbed to provide the longitudinal modes to the electroweak gauge bosons Z^0 and $W^\pm$ giving them mass as well as the interaction strengths $\lambda_{HVV}, \lambda_{HHVV}$ between Higgs and vector bosons ($V = Z^0, W^\pm$). At the same time, the Yukawa-type couplings of the form $g_f\overline{\psi}\psi\Phi$, between fermions and Higgs doublet, leads to terms $g_f v\overline{\psi}\psi$ giving masses to leptons and quarks ($M_f = g_f v$) and residual interactions $\lambda_f\overline{\psi}\psi H$.

Summarizing the SSB mechanism provides particle masses and interaction strengths as in table (1.1)

$M_W = \frac{1}{2}gv$	$M_Z = \frac{1}{2}v\sqrt{g^2+g'^2}$	$M_\gamma = 0$	$M_H = \sqrt{2}\mu$
$M_f = g_f v$	$\lambda_{H\overline{\psi}\psi} = \sqrt{2}g_f$	$\lambda_{HVV} = 2\frac{M_V^2}{v}$	$\lambda_{HHVV} = 2\frac{M_V^2}{v^2}$

Table 1.1: SM particle masses and couplings with Higgs boson

The vacuum expectation value v is related to the Fermi coupling constant $G_F = \frac{g^2\sqrt{2}}{8M_W^2} = \frac{1}{\sqrt{2}v^2}$ and its experimental value is $v = 246.220(4)$ GeV [30]. Since all fermion and vector boson masses are known, all the Higgs properties are fixed by its mass (or equivalently μ) which is the only unknown parameter of the SM Higgs sector.

1.3 Experimental validations of the Standard model and status of the Higgs boson searches

The Standard Model is an elegant theoretical framework that describes the phenomenology of high-energy elementary particles to a remarkable level of accuracy. Several observables can be computed as function of few important parameters: the fine structure constant $\alpha_{em} = e^2/(4\pi)$, the strong coupling constant $\alpha_s = g_s^2/(4\pi)$, the Fermi constant G_F and the masses of elementary particles.

The validity of the SM has been precisely tested for its electroweak sector. A collection of accurate measurements is shown in Figs. 1.1 and 1.2 (respectively non-Z pole and Z pole observables). The column denoted Pull gives the standard deviations for the principal fit with M_H free, while the column denoted Dev. (Deviation) is for $M_H = 117$ GeV. From Fig. 1.1 and 1.2 we see that only the measurements of the muon $g-2$ from BNL and of the hadronic asymmetry $A_{FB}^{(0,b)}$ are currently showing large discrepancies with the corresponding SM prediction. Moreover, A_{LR}^0 from SLD differs by 1.8 sigma from the SM prediction. The discrepancies in the asymmetries are hardly explained in terms of a new physics effect, which should appear already at tree level and involve preferentially the third generation. However, the agreement between SM theoretical predictions and the experimental data is over all excellent, and it is fair to say that no clear evidence for new physics effects has been observed.

Quantity	Value	Standard Model	Pull	Dev.
m_t [GeV]	173.1 ± 1.3	173.2 ± 1.3	-0.1	-0.5
M_W [GeV]	80.420 ± 0.031	80.384 ± 0.014	1.2	1.5
	80.376 ± 0.033		-0.2	0.1
g_L^2	0.3027 ± 0.0018	0.30399 ± 0.00017	-0.7	-0.6
g_R^2	0.0308 ± 0.0011	0.03001 ± 0.00002	0.7	0.7
$g_V^{\nu e}$	-0.040 ± 0.015	-0.0398 ± 0.0003	0.0	0.0
$g_A^{\nu e}$	-0.507 ± 0.014	-0.5064 ± 0.0001	0.0	0.0
$Q_W(e)$	-0.0403 ± 0.0053	-0.0473 ± 0.0005	1.3	1.2
Q_W(Cs)	-73.20 ± 0.35	-73.15 ± 0.02	-0.1	-0.1
Q_W(Tl)	-116.4 ± 3.6	-116.76 ± 0.04	0.1	0.1
τ_τ [fs]	291.09 ± 0.48	290.02 ± 2.09	0.5	0.5
$\frac{\Gamma(b\to s\gamma)}{\Gamma(b\to Xe\nu)}$	$\left(3.38^{+0.51}_{-0.44}\right) \times 10^{-3}$	$(3.11 \pm 0.07) \times 10^{-3}$	0.6	0.6
$\frac{1}{2}(g_\mu - 2 - \frac{\alpha}{\pi})$	$(4511.07 \pm 0.77) \times 10^{-9}$	$(4509.13 \pm 0.08) \times 10^{-9}$	2.5	2.5

Figure 1.1: Principal non-Z pole observables and their SM predictions [30].

The only element of the framework still to be discovered is the Higgs boson and in order to have a complete picture of the SM, the only missing parameter is its mass. More generally, the discovery of the Higgs boson is one of the fundamental open problems of the SM and something missing to reveal the dynamics of the SSB of the Electroweak sector.

Quantity	Value	Standard Model	Pull	Dev.
M_Z [GeV]	91.1876 ± 0.0021	91.1874 ± 0.0021	0.1	0.0
Γ_Z [GeV]	2.4952 ± 0.0023	2.4954 ± 0.0009	−0.1	0.1
Γ(had) [GeV]	1.7444 ± 0.0020	1.7418 ± 0.0009	—	—
Γ(inv) [MeV]	499.0 ± 1.5	501.69 ± 0.07	—	—
$\Gamma(\ell^+\ell^-)$ [MeV]	83.984 ± 0.086	84.005 ± 0.015	—	—
$\sigma_{\rm had}$[nb]	41.541 ± 0.037	41.484 ± 0.008	1.5	1.5
R_e	20.804 ± 0.050	20.735 ± 0.010	1.4	1.4
R_μ	20.785 ± 0.033	20.735 ± 0.010	1.5	1.6
R_τ	20.764 ± 0.045	20.780 ± 0.010	−0.4	−0.3
R_b	0.21629 ± 0.00066	0.21578 ± 0.00005	0.8	0.8
R_c	0.1721 ± 0.0030	0.17224 ± 0.00003	0.0	0.0
$A_{FB}^{(0,e)}$	0.0145 ± 0.0025	0.01633 ± 0.00021	−0.7	−0.7
$A_{FB}^{(0,\mu)}$	0.0169 ± 0.0013		0.4	0.6
$A_{FB}^{(0,\tau)}$	0.0188 ± 0.0017		1.5	1.6
$A_{FB}^{(0,b)}$	0.0992 ± 0.0016	0.1034 ± 0.0007	−2.7	−2.3
$A_{FB}^{(0,c)}$	0.0707 ± 0.0035	0.0739 ± 0.0005	−0.9	−0.8
$A_{FB}^{(0,s)}$	0.0976 ± 0.0114	0.1035 ± 0.0007	−0.6	−0.4
$\bar{s}_\ell^2(A_{FB}^{(0,q)})$	0.2324 ± 0.0012	0.23146 ± 0.00012	0.8	0.7
	0.2316 ± 0.0018		0.1	0.0
A_e	0.15138 ± 0.00216	0.1475 ± 0.0010	1.8	2.2
	0.1544 ± 0.0060		1.1	1.3
	0.1498 ± 0.0049		0.5	0.6
A_μ	0.142 ± 0.015		−0.4	−0.3
A_τ	0.136 ± 0.015		−0.8	−0.7
	0.1439 ± 0.0043		−0.8	−0.7
A_b	0.923 ± 0.020	0.9348 ± 0.0001	−0.6	−0.6
A_c	0.670 ± 0.027	0.6680 ± 0.0004	0.1	0.1
A_s	0.895 ± 0.091	0.9357 ± 0.0001	−0.4	−0.4

Figure 1.2: Principal Z pole observables and their SM predictions [30].

Precision electroweak measurements can be used to constrain the Higgs mass. Fig. 1.3 shows the $\Delta\chi^2$ curve derived from high-Q^2 precision electroweak measurements, performed at LEP and by SLD, CDF, and D0, as a function of the Higgs mass. The preferred value for M_H, corresponding to the minimum of the curve, is at 92 GeV, with an experimental uncertainty of +34 and -26 GeV (at 68 percent confidence level derived from $\Delta\chi^2 = 1$ for the black line, thus not taking the theoretical uncertainty shown as the blue band into account). This result is only little affected by the low-Q^2 results such as those from NuTeV [35]. The precision electroweak measurements tell us that the mass of the Standard-Model Higgs boson is lower than about 161 GeV. This limit increases to 185 GeV when including the LEP2 direct search limit.

Up to now (December 2011) the Higgs boson is not yet been observed. LEP experiments have put a lower limit to the Higgs mass at $M_H > 114.4$ GeV at the 95% C.L. [2]. The Tevatron experiments recently published a combined analysis on direct searches for

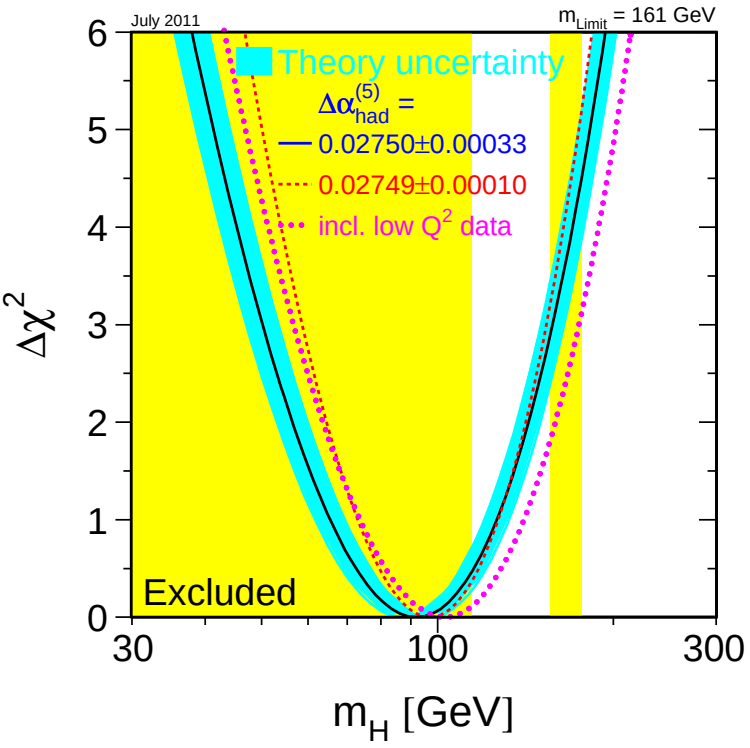

Figure 1.3: $\Delta\chi^2 = \chi^2 - \chi^2_{min}$ vs. M_H curve. The line is the result of the fit using all data; the band represents an estimate of the theoretical error due to missing higher order corrections. The vertical band shows the 95% CL exclusion limit on M_H from the direct search.

the SM Higgs boson in $p\bar{p}$ collisions at a centre-of-mass energy of 1.96 TeV, with up to 8.2 fb^{-1} of data analysed at CDF and up to 8.6 fb^{-1} at DØ. The combined result of this search is reported in Fig. 1.4. The plot displays the ratio of the 95% CL limit on the cross section over the SM cross section as a function of the Higgs mass. When the solid line crosses unity a SM Higgs with the corresponding mass is excluded at 95% CL.

The CDF and DØ combined result shows that the SM Higgs boson is excluded in the mass region $156 < M_H < 177$ GeV (in addition, the constraint $M_H > 108$ GeV confirms part of the LEP limit) [3].

After the shutdown of the Tevatron at the end of september 2011 the Higgs searches are currently being carried out by the ATLAS and CMS experiments at the LHC. The LHC collides protons at a centre-of-mass energy of 7 TeV. The integrated luminosity accumulated in the 2010-2011 run is ∼5.20 fb^{-1} per experiment, and the data analysis is

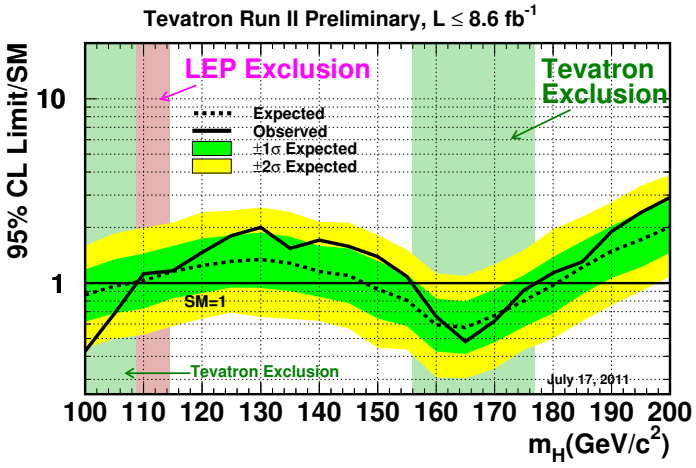

Figure 1.4: Observed and expected 95% C.L. upper limits on the ratios to the SM cross section, as functions of the Higgs boson mass for the combined CDF and DØ analyses.

currently in progress. A first combined exclusion limit (with 1-2.3 fb^{-1} of analysed data) was presented at the HCP conference in Paris and it excluded the region $141 < M_H < 476$ GeV [4]. This combination includes searches using the following Higgs boson decay signatures: $H \to \gamma\gamma, H \to bb, H \to \tau\tau, H \to WW(l\nu l\nu)$ and $H \to ZZ(4l, 2l2\nu, 2l2q, 2l2\tau)$ (see Fig. 1.5).

In a seminar held at CERN on December 13, 2011, the ATLAS and CMS experiments presented the updated status of their searches for the SM Higgs boson. Significant progress in the search for the Higgs boson has been achieved, but not enough to make any conclusive statement on the existence or non-existence of the Higgs. As we can see from Fig. 1.6, the main conclusion is that the SM Higgs boson, if it exists, is most likely to have a mass constrained to the range $116 - 130$ GeV by the ATLAS and $115 - 127$ GeV by the CMS experiment. Both the experiments extended the upper exclusion limit as well, up to ~ 600 GeV.

Both ATLAS and CMS have analysed several decay channels, and the experiments see small excesses of events in the low mass region around $M_H \sim 125$ GeV. Such excesses are not strong enough to claim a discovery. A definitive statement on the existence or non-existence of the Higgs boson will require more data, and is not likely until later in 2012.

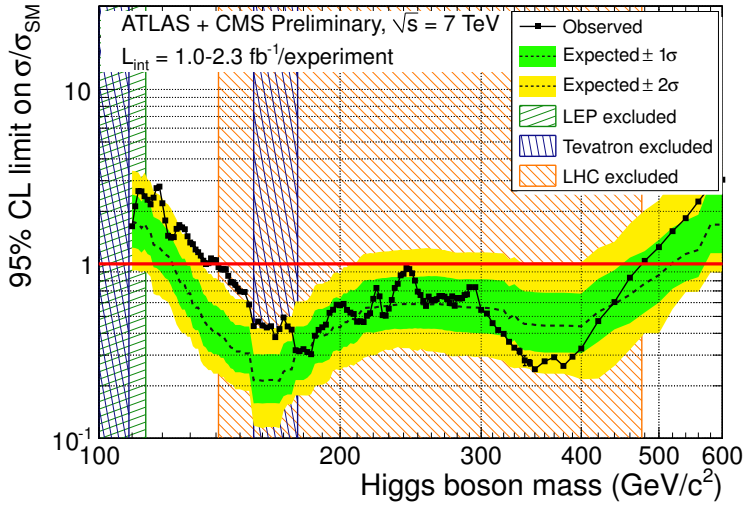

Figure 1.5: The experimental status of the SM Higgs boson searches [4], combining the best results of all the experiments (November 14, 2011).

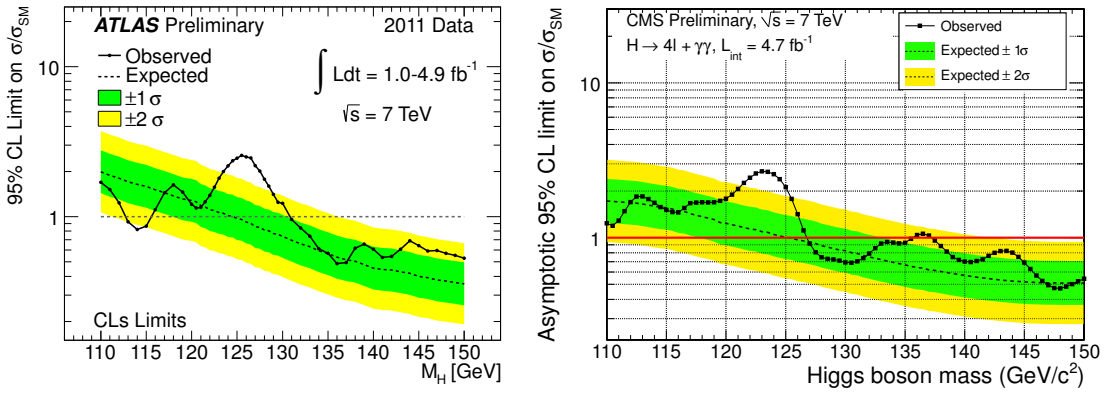

Figure 1.6: The last update of SM Higgs exclusion limit at 95% confidence level for $1-4.9$ fb^{-1} proton-proton data collected by CERN experiments, showing the lower mass region ([5] December 13, 2011). On the left the ATLAS and on the right CMS exclusion plot in the low mass region.

Chapter 2

Perturbative QCD at hadron colliders

In order to test the Standard Model of elementary particles, we have to calculate observables that have to be measured by experiments. The calculations of such observables are made by combining calculations of Feynman diagrams with the use of general features of the theory. At hadron colliders we are studying collisions of composite particles, bound states of quarks and gluons, it is thus necessary to use the parton model framework or, more precisely, the QCD factorisation theorem.

In this chapter we briefly review some general aspects that have to be taken into account in order to provide quantitative predictions.

2.1 Redundant degrees of freedom in the SM Lagrangian and gauge fixing

In a gauge theory the fields are defined with redundant degrees of freedom. In order to calculate physical quantities, we have to take into account the degrees of freedom of the fields in the Lagrangian and the physical degrees of freedom, in order to avoid the non-physical ones. In particular, in QCD we cannot quantize the theory without adding a new gauge-fixing term, i.e. we have to choose the gauge. The key point is that it is impossible to define the propagator of the gauge fields without making a gauge choice [36, 37].

For example, we can solve the problem for the gluon field introducing a *physical* gauge fixing term (2.1), loosing the explicit Lorentz invariance of the Lagrangian

$$\mathcal{L}_{GF}^{phys} = -\frac{1}{2\xi}\sum_{a=1}^{N_c^2-1}\left(\eta^\mu G_\mu^a\right)^2, \tag{2.1}$$

where η^μ is a fixed vector and ξ is a constant. Another choice, in order to preserve the explicit Lorentz invariance is the *covariant* gauge fixing (2.2)

$$\mathcal{L}_{GF}^{cov} = -\frac{1}{2\xi}\sum_{a=1}^{N_c^2-1}\left(\partial^\mu G_\mu^a\right)^2, \tag{2.2}$$

but in this case there are some residual non-physical longitudinal degrees of freedom that have to be cancelled through another contribution [38]: an anticommuting scalar field χ, called ghost, with Faddeev-Popov Lagrangian $\mathcal{L}_{FP}$

$$\mathcal{L}_{FP} = (\partial^\mu \chi^{a*})\,(\delta^{ab}\partial_\mu - g_s f^{abc} G_\mu^c)\chi^b. \tag{2.3}$$

We obtain the gluon propagator

$$(i\delta^{ab} d_{\mu\nu}^i(k))/(k^2 + i\epsilon), \tag{2.4}$$

where the polarization tensor $d_{\mu\nu}^i(k)$ in the two gauges is:

$$d_{\mu\nu}^{phys}(k) = -g_{\mu\nu} + \frac{k_\mu\eta_\nu + k_\nu\eta_\mu}{\eta\cdot k} - \eta^2\frac{k_\mu k_\nu}{(\eta\cdot k)^2}, \tag{2.5}$$

$$d_{\mu\nu}^{cov}(k) = -g_{\mu\nu} + (1-\xi)\frac{k_\mu k_\nu}{k^2}. \tag{2.6}$$

Note that in the covariant gauge we have also to introduce the ghost propagator $i\delta^{ab}\frac{1}{k^2+i\epsilon}$.

In general, we are free to choose between the two gauge fixing terms (or also other gauge fixing), and the obtained predictions must be equivalent. Typically the physical gauge makes lowest-order and approximate higher-order calculations easier, but in general the best choice depends on the actual calculations that have to be performed.

2.2 Ultraviolet divergences, renormalization and running coupling constant

Let us consider the quantum corrections that affect a physical observable in a general hard scattering process. Considering radiative corrections to the leading order terms, we easily obtain divergent contributions.

For instance, from loop-contributions like the one-loop correction to a gauge boson propagator with momentum k (see Fig. 2.1), we obtain integrals that are divergent in the Ultraviolet region (UV), i.e. where the loop momentum p is much larger than the vector boson momentum[1] k. In our example in the limit $p \to \infty$ we obtain

$$\int d^4p \frac{1}{p^2}\frac{1}{(k+p)^2} \overset{|p|\gg|k|}{\longrightarrow} \int d^4p \frac{1}{p^4}. \tag{2.7}$$

[1] A loop integral could be also divergent in the Infra-Red region (IR) for a vanishing loop momentum $|p|$. We will discuss later this divergence.

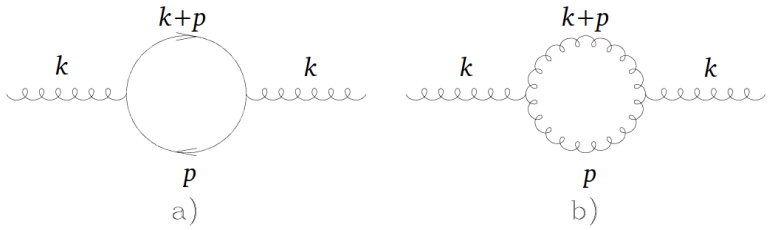

Figure 2.1: One loop correction at the vector boson propagator.

In order to build a self-consistent theory, we have to remove these divergences. This task can be completed through the *renormalization procedure* [39], that is carried out in three main steps. First of all the loop integrals must be properly defined. This is done through the *regularisation procedure*, which can be accomplished for example by introducing an UV cut-off in the loop integrals, or by continuing the number of dimensions to $D = 4 - 2\epsilon$. Then the divergent terms can be isolated. Finally order by order in perturbation theory we introduce in the Lagrangian suitable counterterms, in order to cancel the divergences arising from UV momenta above a certain arbitrary renormalization scale μ_R. The gauge invariance guarantees that these divergent terms have the same structure of the original (bare) ones. Finally we define new renormalized parameters ($g(\mu_R)$, $m(\mu_R)$, ...) related to the bare ones (g, m, ...) through the following relations

$$g(\mu_R) = g \cdot Z_g^{-1}(\mu_R), \tag{2.8}$$

$$m(\mu_R) = m \cdot Z_m^{-1}(\mu_R), \tag{2.9}$$

where the renormalization constant Z embodies the infinities. The renormalized quantities are finite and useful to calculate measurable physical quantities.

The original Lagrangian is independent on the unphysical scale μ_R, thus any physical measurable quantity $A(\alpha_s)$ must be independent on the variable μ_R.

The dependence of the QCD coupling α_s on the renormalisation scale is controlled by the renormalisation group equation

$$\beta(\alpha_s) \equiv \frac{\partial \alpha_s}{\partial \log \mu_R^2}, \tag{2.10}$$

The beta-function is characteristic of the theory and can be calculated by the following perturbative expansion

$$\beta(\alpha_s) = -\alpha_s \sum_{n=0}^{\infty} \beta_n \left(\frac{\alpha_s}{\pi}\right)^{n+1}, \tag{2.11}$$

in QCD the first coefficients are[2]

$$\beta_0 = \frac{33 - 2n_f}{12} \tag{2.12}$$

$$\beta_1 = \frac{153 - 19n_f}{24} \tag{2.13}$$

$$\beta_2 = \frac{2857}{128} - \frac{5033n_f}{1152} + \frac{325n_f^2}{3456} \tag{2.14}$$

If the coupling is in the perturbative region, i.e. $\alpha_s(\mu_R) \ll 1$, it makes sense to truncate the series (2.11) at the first order $\beta \simeq -\beta_0\alpha_s^2/\pi$ and solve the differential equation (2.10) obtaining

$$\alpha_s(\mu_R) = \frac{\alpha_s(\mu_0)}{1 + \alpha_s(\mu_0)\beta_0 \log(\mu_R^2/\mu_0^2)} \tag{2.15}$$

by this equation, it is possible to calculate the value of the coupling constant at any scale μ_R knowing only one experimental value of $\alpha_s(\mu_0)$ at a given reference scale μ_0. The mass of the Z^0 vector boson is the typical choice for the reference scale: $\mu_0 = M_{Z^0} \sim 91.2$ GeV.

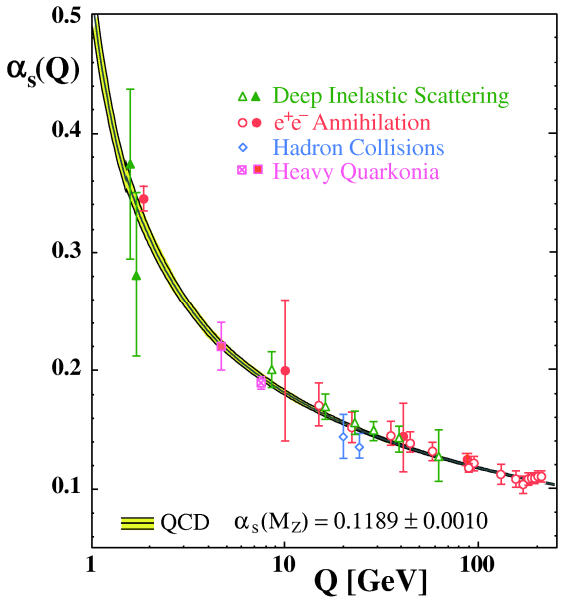

Figure 2.2: Various measurements of the strong coupling constant α_s at different energy scales [40].

Eq. (2.15) implies that the coupling α_s increases if the scale μ_R decreases and vice-

[2]Often in the literature the perturbative expansion of the β function in Eq. (2.11) is organized in powers of $\left(\frac{\alpha_s}{2\pi}\right)$ or $\left(\frac{\alpha_s}{4\pi}\right)$. In these cases the factor 2 or 4 are embedded in the definition of the coefficients β_n.

versa diverges at the scale $\mu_R = \Lambda_{QCD} \simeq 200$ MeV, i.e.

$$\Lambda_{QCD} \simeq \mu_0 \exp\left(-\frac{\pi}{2\beta_0 \alpha_s(\mu_0)}\right) \quad \Rightarrow \quad \lim_{\mu_R \to \Lambda_{QCD}} \alpha_s(\mu_R) = \infty. \tag{2.16}$$

Λ_{QCD} can be used to define the reference scale for the region where α_s becomes too large to perform perturbation calculations.

The results in Eqs. (2.15,2.16) are obtained approximating the beta function at the first order. Considering higher order corrections we substantially obtain the same behaviour.

From Fig. 2.2 we see that the strong coupling constant asymptotically decreases when the energy scale increases

$$\lim_{\mu_R \to \infty} \alpha_s(\mu_R) = 0. \tag{2.17}$$

The behaviour in Eqs. (2.16,2.17) reflects two important features of QCD: *confinement* and *asymptotic freedom*. The former concerns the fact that quarks and gluons cannot be observed as asymptotic free states that propagate at large distances (low energies) due to increasing coupling strength; the latter reflects that quarks and gluons inside hadrons or mesons behave as free at short distances (high energies);

2.3 Perturbation theory at high energies

In high energy processes the coupling α_s is small, thus we can calculate a generic physical observable A as perturbative expansion of the coupling.

$$A = \sum_{i=0}^{\infty} A_i \, \alpha_s^i \tag{2.18}$$

By definition, the Leading-Order calculation (LO) is made taking into account only the first non-zero coefficient A_p times α_s^p. Then in the Next-to-Leading Order (NLO) calculation we take into account the coefficient A_{p+1} and one additional power of α_s, the Next-to-Next-to Leading Order (NNLO) carries A_{p+2} and another additional power of α_s, and so on:

$$\begin{aligned} A_{LO} &= \alpha_s^p A_p, \\ A_{NLO} &= \alpha_s^p \left(A_p + \alpha_s A_{p+1}\right), \\ A_{NNLO} &= \alpha_s^p \left(A_p + \alpha_s A_{p+1} + \alpha_s^2 A_{p+2}\right). \end{aligned} \tag{2.19}$$

Sometimes it is useful to write the expansion as follows

$$A = \alpha_s^p \left(A^{(0)} + \alpha_s A^{(1)} + \alpha_s^2 A^{(2)} + \dots\right). \tag{2.20}$$

In this case $A^{(n)}$ is the contribution necessary to the A_{N^nLO} calculation, where now we use the following alternative notation

$$A_{N^nLO} = \alpha_s^p \sum_{i=0}^{n} A^{(i)}\, \alpha_s^i. \tag{2.21}$$

Typical QCD observables are dependent on the energy scale Q of the scattering process and the strong coupling is dependent on the renormalization scale μ_R. Thus we generalize Eq. (2.20) writing the explicit dependence of both the scales

$$A(Q^2) = \alpha_s^p(\mu_R^2)\left(A^{(0)}(Q^2) + \alpha_s(\mu_R^2)A^{(1)}(Q^2,\mu_R^2) + \alpha_s^2(\mu_R^2)A^{(2)}(Q^2,\mu_R^2) + \dots\right). \tag{2.22}$$

Beyond the LO, also the coefficients $A^{(n)}$ depend on μ_R; at the NLO the dependence on μ_R can be written as follows [41]

$$A^{(1)}(Q^2,\mu_R^2) = A^{(1)}(Q^2=\mu_R^2) - p\frac{\beta_0}{\pi}A^{(0)}(Q^2)\log(Q^2/\mu_R^2) + \dots \tag{2.23}$$

Since physical observables do not know anything about renormalization, if we calculate $A(Q^2)$ to all orders the dependence on μ_R would completely cancel through α_s and the perturbative contributions, while truncating the series to some finite order makes the results scale dependent. The amount of the scale dependence can be used to estimate the uncertainty and the reliability of the theoretical predictions. As we can see from Eq. (2.23) the presence of the logarithmic term suggests that we have to choose $\mu_R \simeq Q$. Choosing μ_R too different from Q introduces large logarithms that spoil the convergence of the series. The typical choice is to set $\mu_R \sim Q$, and study the perturbative uncertainties by varying the scale μ_R of a factor of two, in the range $(\mu_R/2, 2\mu_R)$.

2.4 Infrared divergences and their cancellation

In section 2.2 we discussed the UV divergences and their regularisation procedure through renormalisation. UV divergences are an important feature of QCD and of most of quantum field theories. Nevertheless the UV is not the only possible divergence of a quantum field theory. Loop contributions as Eq. (2.7) are typically divergent in the high energy region, and also in the low energy limit. They suffer of other divergences related to long distance phenomena (IR divergences).

In order to study the IR divergences, we consider as an example the calculation of the inclusive cross section for the inclusive production of a quark-antiquark pair $q\bar{q}$ in a electron-positron e^+e^- annihilation. We have to calculate σ for the process $e^+e^- \to \gamma^* \to q\bar{q} + X$, where X denotes some unobserved final state radiation

$$\sigma = \left(\sigma^{(0)} + \alpha_s\sigma^{(1)} + \dots\right). \tag{2.24}$$

At the LO we have a tree level Feynman diagram and we can graphically represent the process as in Fig. (2.3); the calculation gives the finite result

$$\begin{aligned} \sigma &\simeq \sigma_{LO} = \sigma_B \cdot 3 \sum_{n_f} Q_q^2, \\ \sigma_B &\equiv \frac{4\pi\alpha_{em}^2}{3s} \end{aligned} \tag{2.25}$$

where $s = 4E^2$ and E is the energy of the incoming electrons, Q_q the electric charge of the quarks and σ_B is named Born cross section; the sum runs over the kinematically accessible flavours n_f at the energy E and the factor 3 in front of the sum is the colour factor; σ_B is named *Born cross section.*

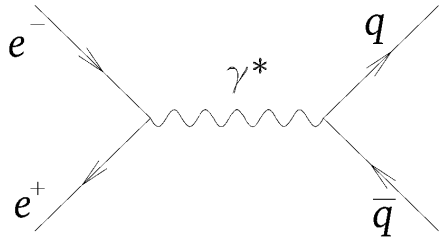

Figure 2.3: The LO Feynman diagram for the process $e^+e^- \to \gamma^* \to q\bar{q} + X$. In this case $X = 0$ because there is no real emission.

The NLO contribution is made of two parts: the *virtual* contribution that includes one loop diagrams as in Fig. (2.4a) and the *real* contribution as in Fig. (2.4b) that takes into account the emission of a final state gluon

The virtual contribution in Fig. (2.4a) is IR divergent. Also the real contribution is divergent tanks to the emission of a soft and/or collinear gluon. This is due to a term in the fermion propagator of the form

$$\frac{1}{2E_1E_k(1-\cos\theta)}, \tag{2.26}$$

where E_1, E_k are respectively the energies of the quark and the gluon and θ is the emission angle of the gluon. For $E_k \to 0$ we have the soft divergence and for $\theta \to 0$ the collinear divergence (and for both $E_k, \theta \to 0$ the soft-collinear divergence).

In order to isolate and remove the divergences a variety of methods are used. For example one can give the gluon a small mass or take off-shell by a small amount the final state quark-antiquark; with these procedure we are regularizing the integral through a small cut-off and the singularities are isolated as logarithms of the cut-off mass. A more elegant procedure is provided by the dimensional regularization: we evaluate the diagrams in d-dimensions ($d \equiv 4 - 2\epsilon$) instead of the 4-dimensional physical space-time.

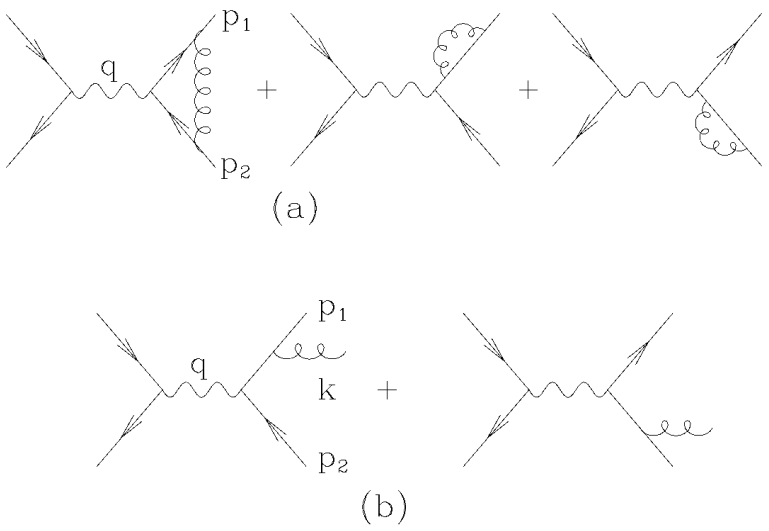

Figure 2.4: The NLO Feynman diagram for the process $e^+e^- \to \gamma^* \to q\bar{q} + X$: the diagrams represent the virtual (a) and the real-emission (b) contributions. In this case X corresponds to the emitted gluon in the final state.

The singularities appear as poles at $d = 4$, see [37, 42]. We obtain

$$\begin{aligned} \sigma_{NLO}^{virt} &= \sigma_B 3 \sum_{n_f} Q_q^2 \frac{2\alpha_s}{3\pi} H(\epsilon) \left[-\frac{2}{\epsilon^2} + \frac{3}{\epsilon} - 8 + o(\epsilon) \right], \\ \sigma_{NLO}^{real} &= \sigma_B 3 \sum_{n_f} Q_q^2 \frac{2\alpha_s}{3\pi} H(\epsilon) \left[\frac{2}{\epsilon^2} - \frac{3}{\epsilon} + \frac{19}{2} + o(\epsilon) \right], \end{aligned} \tag{2.27}$$

where $H(\epsilon) = 1 + o(\epsilon)$.

Adding together the virtual and real contributions the poles exactly cancel and in the limit $\epsilon \to 0$ we obtain a finite result.

From (2.25) and (2.27) the cross section at the NLO accuracy is

$$\sigma \simeq \sigma_B \cdot 3 \sum_{n_f} Q_q^2 \left[1 + \frac{\alpha_s}{\pi} + o(\alpha_s^2) \right]. \tag{2.28}$$

The cancellation of the IR divergences is not accidental. The Bloch-Nordsieck [43] and Kinoshita-Lee-Nauenberg [44] theorems guarantee (in the massless limit) the cancellation order by order of IR singularities for suitably defined inclusive quantities. An observable for a final state consisting of m particles is called *infrared and collinear safe* if it satisfies the following two requirements. If two particles in the final state have collinear momenta, the observable should allow to consider the two particles as one particle with momentum equal to the sum of the two original ones. This is the so called *collinear safety* criterion.

If one particle in the final state has vanishing energy, the observable should allow to neglect it. This is the so called *infrared safety* criterion.

Thanks to the IR cancellation theorems, we know that order by order the divergences arising separately from virtual and real Feynman diagrams cancel each other.

2.5 Deep inelastic scattering and hadron collisions

In the previous section, we discussed the IR divergences in case of e^+e^- collisions. These divergences are closely related to the long-distance effects or equivalently the confinement in the low energy limit, see Eq. (2.16).

For e^+e^- collisions the total cross section is free of IR divergences, but in the case of high energy lepton-hadron collisions (DIS) or hadron-hadron collisions, the calculation of cross sections is more complicate. First of all, hadrons are bound states of many partons (i.e. quarks and gluons). Since partons are confined into such colliding hadrons, additional large distance effect play an important role.

In order to describe the collision process, we can imagine that only one parton (and not the whole hadron) collides with the lepton in the DIS collision or only one parton from each hadron in hadron-hadron collision. In this case, we can perturbatively calculate the lepton-parton or parton-parton hard cross section. This is the main idea for the so called *parton model*.

In practice we are decoupling the large-distance physics effects with the hard scattering process and a simple heuristic argument supports this picture. At sufficient high energies, colliding hadrons are highly Lorentz-contracted in the centre of mass frame and the interactions between internal partons (which are separated in the transverse direction) are time dilated. The hard process takes place in a much shorter time scale, so that the two phenomena can be considered to a good extent independent. Sometimes this argument is referred to "incoherence" of long and short distance effects. For the most important processes there exist *factorization theorems* that, order by order in perturbation theory, rigorously prove this separation of short-long distance physics (see [45] and references therein).

In the DIS collision, we can write the cross section between an hadron $h_1(P_1)$ and a lepton $l(P_2)$ (with respectively momenta P_1, P_2) to a final state F (plus possible radiation X) at the hard scattering energy scale Q^2, as a convolution between the *partonic cross section* $\hat{\sigma}_{a_1 l \to F+X}(x_1 P_1, P_2, \mu_F^2, \alpha_s(Q^2))$ and the *Parton Distribution Functions* (PDFs) $f_{a_1}(x, Q, \mu_F)$. The PDFs are process independent (universal) and give the probability of finding a parton a_1 in the hadron h_1 with momentum fraction $0 \leq x_1 \leq 1$, at the energy

scale Q. In practice we have

$$\sigma_{h_1 l\to F+X}(P_1,P_2,Q^2)=\sum_{a_1}\int_0^1 dx_1\ f_{a_1}(x_1,\mu_F)\ \hat{\sigma}_{a_1 l\to F+X}(x_1P_1,P_2,\mu_F^2,\alpha_s(Q^2)), \quad (2.29)$$

for most of the physical observables at the experiments, we cannot distinguish the original parton from the observed final state. In that cases we have to sum over all the allowed partons in the initial state, thus we must sum over all the partons a_1 that can produce the same final state $F+X$ at the given perturbative order.

In hadron-hadron collisions we have to take into account all the combinations from the possible partons in the initial state of both the colliding hadrons and the respective PDFs. We generalize the Eq. (2.29) as follows

$$\begin{aligned}\sigma_{h_1h_2\to F+X}(P_1,P_2,Q^2) &= \sum_{a_1a_2}\int_0^1 dx_1\int_0^1 dx_2\ f_{a_1}(x_1,\mu_F)\ f_{a_2}(x_2,\mu_F)\\ &\cdot\ \hat{\sigma}_{a_1a_2\to F+X}(x_1P_1,x_2P_2,\mu_F^2,\alpha_s(Q^2)) \quad (2.30)\end{aligned}$$

Defining $s=(P_1+P_2)^2$ as the square of the centre of mass energy of the colliding hadrons and $\hat{s}$ as the same quantity for the colliding partons, they are related as follows

$$\hat{s}=x_1x_2s. \quad (2.31)$$

For a typical collision $x_1\sim x_2$; thus at the LHC with energy 7/14 GeV and for $\sqrt{\hat{s}}\simeq$ 100/200 GeV we can estimate the typical value of the Bjorken x as

$$x\simeq\sqrt{\hat{s}/s}\simeq 10^{-2}. \quad (2.32)$$

Another important aspect, that we have not discussed, is the role of the scales Q,μ_F. In the *naïve parton model* the partonic cross section is calculated at the LO and PDFs are independent of the Q scale. This follows from the *Bjorken scaling* of the structure functions of the proton: it is well verified by experiments that the structure functions turns out be almost independent on the Q^2 energy scale for $Q\gtrsim 2$ GeV and x finite, then the PDFs are independent on the energy scale Q. Considering perturbative corrections the incoming partons could emit some QCD radiation, leading to a dependence of the PDFs on the energy scale Q, giving rise to a *Bjorken scaling violation.*

In the calculation of the perturbative corrections to the partonic cross section, we encounter the IR divergences discussed in Fig. 2.4 and in Eq. (2.26). The exact cancellation between real and virtual divergences happen only for the ones in the final state. Initial state divergences do not cancel in this case and there are some remnant collinear divergences due to the collinear emission from the initial state partons. We can deal with the problem and obtain the *improved parton model* in a similar way as we do for

the UV divergences: we define some bare-PDFs and we absorb the remnant collinear IR divergences in the definition of the PDFs, in such a way that the physical PDFs are finite. At the end of the regularization procedure the renormalized PDFs depend on the factorisation scale μ_F, analogously to what happens in the UV renormalisation, where we introduced the μ_R scale.

It is important to notice that the PDFs are independent on the partonic process, they are universal. This universality is of crucial importance because we can measure[3] the PDFs in a particular collision process and then we can use them to calculate other process (see [45] and in particular [47]). Such universality is not accidental. It is a consequence of the universality of the remnant collinear divergence due to partonic initial state emission(s) (that is adsorbed by the universal bare-PDFs).

The factorisation scale μ_F can be interpreted as a separation between the low energy physics inside the hadron and the high energy physics of the partonic collision. This is an unphysical separation and the results of the calculations must be independent on the factorisation scale (this is analogous as for the renormalization scale μ_R): the PDF dependence on the factorisation scale has to be compensated by the partonic cross section that is also dependent on μ_F (see in Eqs. (2.29,2.30)). The cancellation is exact only if all the quantities are calculated to all orders: truncating the perturbative expansion at a given fixed order makes the results scale dependent (exactly as for the μ_R dependence). As for μ_R, it is usual to set $\mu_F \sim Q$ and to vary μ_F by a factor two around the central value, to estimate the uncertainty of the theoretical predictions.

2.6 DGLAP evolution equation and splitting functions

The μ_F scale dependence of the PDFs can be predicted by the Dokshitzer-Gribov-Lipatov-Altarelli-Parisi (DGLAP) evolution equation [48]; it is the analogous of the renormalization group equation (2.10) describing the μ_R scale dependence of the α_s coupling. In order to emphasize this analogy, we are going to provide a simple heuristic derivation of the DGLAP equation.

First of all we have to define the *Mellin transform* $f(n) \equiv f_n$ of a function $f(x)$:

$$f(n) \equiv \int_0^1 x^{n-1} f(x) dx. \tag{2.33}$$

Now we write in a symbolic form the DIS cross section σ of Eq. (2.29) as $\sigma = f \otimes \hat{\sigma}$, where $\otimes$ represents the convolution between the PDF f and the partonic cross section

[3] At present there is not a theoretical model that can predict these functions from first principles. Also the Lattice QCD is not able to predict the PDFs with enough precision. These functions can only be obtained by fitting the experimental data [46].

$\hat{\sigma}$. In the Mellin space the convolution is a simple product of functions $\sigma_n = f_n \hat{\sigma}_n$ and we can easily calculate the derivative with respect to μ_F

$$\mu_F^2 \frac{\partial \sigma}{\partial \mu_F^2} = \mu_F^2 \left(\frac{\partial f_n}{\partial \mu_F^2} \right) \hat{\sigma}_n + \mu_F^2 f_n \left(\frac{\partial \hat{\sigma}_n}{\partial \mu_F^2} \right) \equiv 0; \tag{2.34}$$

this is the analogous of Eq. (2.10) (that follows from the μ_R scale independence), and we directly obtain the following

$$\mu_F^2 \frac{1}{f_n} \left(\frac{\partial f_n}{\partial \mu_F^2} \right) = -\mu_F^2 \frac{1}{\hat{\sigma}_n} \left(\frac{\partial \hat{\sigma}_n}{\partial \mu_F^2} \right), \tag{2.35}$$

the left and right side of the previous equation are two different functions of the same variable μ_F, then they must be equal to a same function of μ_F: the *anomalous dimension* $\gamma_n(\mu_F)$. Considering only the right side of Eq. (2.35) we can give a definition of $\gamma_n(\mu_F)$ expressed in the Mellin space

$$-\mu_F^2 \frac{1}{\hat{\sigma}_n} \left(\frac{\partial \hat{\sigma}_n}{\partial \mu_F^2} \right) = \frac{\alpha_s}{\pi} \gamma_n, \tag{2.36}$$

By convention, we factorize out the α_s/π factor from the definition of the anomalous dimension γ_n. Calculating $\hat{\sigma}$ at a given perturbative order, we can obtain the expression for the anomalous dimension at the same perturbative order.

Considering the left side of Eq. (2.35) we obtain the DGLAP equation, in the Mellin space

$$\mu_F^2 \left(\frac{\partial f_n}{\partial \mu_F^2} \right) = \frac{\alpha_s}{\pi} \gamma_n f_n. \tag{2.37}$$

Inverting the Mellin transform and restoring omitted details of Eq. (2.37), we obtain the DGLAP evolution equation for the PDFs

$$\mu_F^2 \frac{\partial}{\partial \mu_F^2} f(x, \mu_F) = \frac{\alpha_s(\mu_F)}{\pi} \int_x^1 \frac{dy}{y} P\left(\frac{y}{x}, \alpha_s(\mu_F) \right) f(y, \mu_F). \tag{2.38}$$

The above derivation is not rigorous, for example we did not discuss the introduction of the μ_F dependence in the coupling, but a more detailed derivation based on the operator product expansion and the renormalization group equation confirms this result [49, 28].

The $P(y)$ is known as *Altarelli-Parisi splitting function* and (at this level) describes only the evolution of *non-singlet* PDFs, defined as differences between quark distributions, e.g. $f_{NS} \equiv f_a - f_b$. More generally the DGLAP equation is a $(2n_f+1)$-dimensional matrix equation in the space of gluons, quarks and antiquarks:

$$\mu_F \frac{\partial}{\partial \mu_F^2} \begin{Bmatrix} f_g(x, \mu_F) \\ f_{q_i}(x, \mu_F) \end{Bmatrix} = \tag{2.39}$$

$$\frac{\alpha_s(\mu_F)}{\pi} \sum_{q_j} \int_x^1 \frac{dy}{y} \begin{bmatrix} P_{gg}\left(\frac{y}{x}, \alpha_s(\mu_F)\right) & P_{gq_j}\left(\frac{y}{x}, \alpha_s(\mu_F)\right) \\ P_{q_i g}\left(\frac{y}{x}, \alpha_s(\mu_F)\right) & P_{q_i q_j}\left(\frac{y}{x}, \alpha_s(\mu_F)\right) \end{bmatrix} \begin{Bmatrix} f_g(y, \mu_F) \\ f_{q_j}(y, \mu_F) \end{Bmatrix}$$

where f_{q_j} is a vector with all the PDFs for quarks and antiquarks and the sum over q_j runs over all of them.

We recall that the splitting functions are related to the anomalous dimension by Mellin transform

$$\gamma_{ab}(n, \alpha_s) = \int_0^1 dx\, x^{n-1} P_{ab}(x, \alpha_s), \tag{2.40}$$

and can be calculated as perturbative expansion in terms of α_s

$$P_{ab}(x, \alpha_s) = P_{ab}^{(0)}(x) + \frac{\alpha_s}{\pi} P_{ab}^{(1)}(x) + \dots \tag{2.41}$$

Not all the splitting functions are independent: the charge conjugation invariance and $SU(n_f)$ flavour symmetry imply the following relations

$$\begin{aligned} P_{q_i q_j} &= P_{\bar{q}_i \bar{q}_j} \qquad & P_{q_i \bar{q}_j} &= P_{\bar{q}_i q_j} \\ P_{q_i g} &= P_{\bar{q}_i g} \qquad & P_{g q_i} &= P_{g \bar{q}_i} \end{aligned} \tag{2.42}$$

At the leading order, the splitting functions P_{ab} can be interpreted as the probabilities that a parton of type a evolves into a parton of type b, where the final parton carries a momentum fraction x of the parent parton; the interpretation as probability implies that the splitting functions are positive definite for $0 \leq x < 1$ (this is true if we do not include the virtual corrections which give a negative contribution in $x = 1$) and satisfy the sum rules

$$\begin{aligned} \int_0^1 dx\, P_{qq}^{(0)}(x) &= 0 \\ \int_0^1 dx\, x \left[P_{qq}^{(0)}(x) + P_{gq}^{(0)}(x) \right] &= 0 \\ \int_0^1 dx\, x \left[2 n_f P_{qg}^{(0)}(x) + P_{gg}^{(0)}(x) \right] &= 0 \end{aligned} \tag{2.43}$$

which corresponds to the momentum conservation and the quark number conservations in the splitting of quarks and gluons respectively.

In QCD the sum rules remain valid up to perturbative corrections because of the vanishing of the first momentum of the non-singlet anomalous dimension, and in practice the sum rules provide a variety of informations: from constraints on the PDFs to tests of conservation law to precision measurement of α_s.

We conclude this chapter with a quantitative example of the PDFs, that at present are obtained from data fits of a variety of different experiments (DIS, Drell-Yan, and jet production). A number of groups have produced publicly available PDFs using analysis frameworks and different data sets [46]. Here in Fig. 2.5, we show the 68% C.L. results obtained by the MSTW group [50]; the PDFs are plotted at two different energy scales ($Q^2 = 10/10^4$ GeV^2).

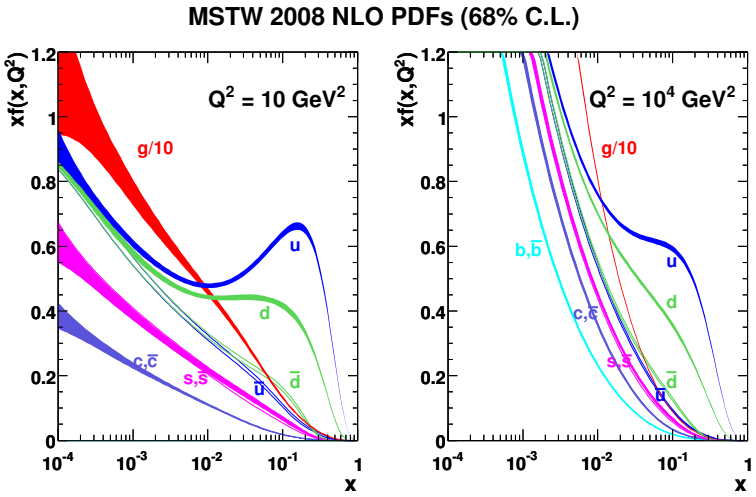

Figure 2.5: The MSTW PDFs at 68% C.L. [50], on the left at the energy scale $Q^2 = 10$ GeV^2 and on the right $Q^2 = 10^4$ GeV^2.

As we can see, the large x region is dominated by the valence quark PDFs distributions (u, d), whereas the low x region is dominated by the gluon PDF. This is an important feature: increasing the collision energy as Eq. (2.32), we explore the low-x region and the processes sensitive to the gluon PDF are strongly enhanced. This is the case for Higgs production through gluon-gluon fusion and we will discuss this point with more detail in the next chapter.

Chapter 3

Higgs boson at hadron colliders

The study of the electroweak symmetry breaking sector of the SM or its equivalent in theories beyond the SM is one of the main goals of the LHC. It is thus of crucial importance to find the Higgs boson and to study its properties, in particular to determine its mass, width and couplings.

In hadron-hadron collisions several Higgs production mechanisms exist and the Higgs boson can eventually decay into several modes. Unfortunately the same final states can be also created by large amount of other processes (called background processes). In order to exploit the LHC potential we need (from the experimental side) high performance detectors and accurate data analysis, and (from the theoretical side) very precise predictions for both the Higgs signals and the corresponding background processes.

In this chapter we will discuss the main production channels of the Higgs boson at hadron colliders, and the corresponding decay modes. Finally we will discuss the Higgs boson search strategies at the LHC and the Tevatron.

3.1 Factorisation of the Higgs production and decay partonic cross section

In a generic hadron collision cross sections are calculated according to the factorisation theorem in Eq. (2.30), by convoluting the partonic cross section with the PDFs. Here we concentrate on the calculation of the partonic cross section for two partons a_1, a_2 producing the Higgs that decays into a final state F_i. This partonic cross section can be expressed as follows

$$\hat{\sigma}_{a_1 a_2 \to H \to F_i} = \frac{1}{4\text{Flux}} \overline{|M_{a_1 a_2 \to H \to F_i}|^2} PS_{F_i}, \tag{3.1}$$

where $\frac{1}{\text{Flux}}$ is the flux factor of two incoming particles, PS_{F_i} is the phase space measure for the final state particles and $\overline{|M_{a_1 a_2 \to H \to F_i}|^2}$ is the squared matrix element, averaged

over the spin and colour of the initial state particles.

The standard model Higgs boson is a scalar neutral particle, thus the Higgs propagator does not carry spinorial or Lorentz indices. In hadron colliders the Higgs boson is produced by strong interacting particles such as gluons and quarks, and we are interested in electroweak decays. These features allow us to study separately the production and the decay processes: we can factorise the matrix element as follows

$$\overline{|M_{a_1a_2\to H\to F_i}|^2} \simeq \overline{|M_{a_1a_2\to H}|^2} \left(\frac{1}{(\hat{s}-M_H^2)^2 + M_H^2\Gamma_H^2} \right) \overline{|M_{H\to F_i}|^2}, \tag{3.2}$$

where $\overline{|M_{a_1a_2\to H}|^2}$ and $\overline{|M_{H\to F_i}|^2}$ are the squared matrix elements respectively related to the Higgs boson production and decay; they are joint by the Breit-Wigner distribution centred at Higgs mass M_H and total Higgs decay width Γ_H.

In some calculations it is useful to adopt the *narrow-width approximation* (where it is considered the limit $\Gamma_H \to 0$), obtaining:

$$\frac{1}{(\hat{s}-M_H^2)^2 + M_H^2\Gamma_H^2} \simeq \frac{\pi}{M_H\Gamma_H}\delta(\hat{s}-M_H^2); \tag{3.3}$$

the narrow-width approximation is particularly justified in the low Higgs mass region $M_H \lesssim 150$ GeV, where the total width is small if compared with Higgs mass (see Fig. 3.1). In practice we can separate the calculation in two parts: the Higgs boson production and its decay.

The cross section for Higgs *production* is

$$\hat{\sigma}_{a_1a_2\to H} = \frac{1}{4\text{Flux}} \overline{|M_{a_1a_2\to H}|^2} PS_H \tag{3.4}$$

where the phase space for the on-shell Higgs boson is $2\pi\delta(\hat{s}-M_H^2)$; the *decay* can be described through the *Branching Ratios*, defined as the fraction of decays in an individual decay mode $\Gamma_{H\to F_i}$ with respect to the total decay width Γ_H:

$$Br_{H\to F_i} = \frac{\Gamma_{H\to F_i}}{\Gamma_H} \tag{3.5}$$

The partonic cross section of Eq. (3.1) can be thus approximated by the Higgs production cross section times the branching ratio, as follow

$$\hat{\sigma}_{a_1a_2\to H\to F_i} \simeq \hat{\sigma}_{a_1a_2\to H} \cdot Br_{H\to F_i}. \tag{3.6}$$

In the next sections we firstly concentrate on the Higgs production mechanisms at hadron colliders and then on the decays widths.

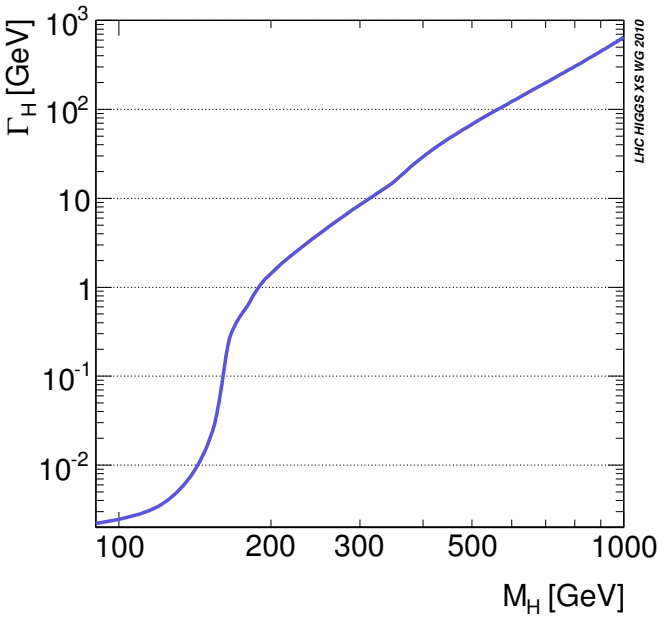

Figure 3.1: The SM Higgs boson total decay width, obtained with the `HDECAY` numerical code [51], as function of M_H [52].

3.2 Higgs production mechanisms at hadron colliders

In this section we are going to discuss the Higgs boson production at hadron colliders. In Fig. 3.2 we report the cross sections $\hat{\sigma}_{pp\to H}$ in the various production channels (over the entire Higgs mass range) currently under investigation at the LHC. As we can see, thanks to the small-x enhancement of the gluon PDF as shown in Fig. 2.5 and Eq. (2.32), the main production channel at high energy hadron colliders is the gluon-gluon fusion. In the following sections we will discuss in more detail the gluon fusion process, that is the main subject of this thesis, and we will give only a short overview about the other production channels (they have a smaller cross section and also they are not related to the main topic of this thesis).

3.2.1 Gluon-gluon fusion process

Gluons are massless particles and they do not couple to the Higgs boson; their interaction whit the Higgs boson is mediated by a triangular loop of massive quarks, which is shown in Fig. 3.3.

The cross section for the Higgs production by gluon fusion is given in terms of its

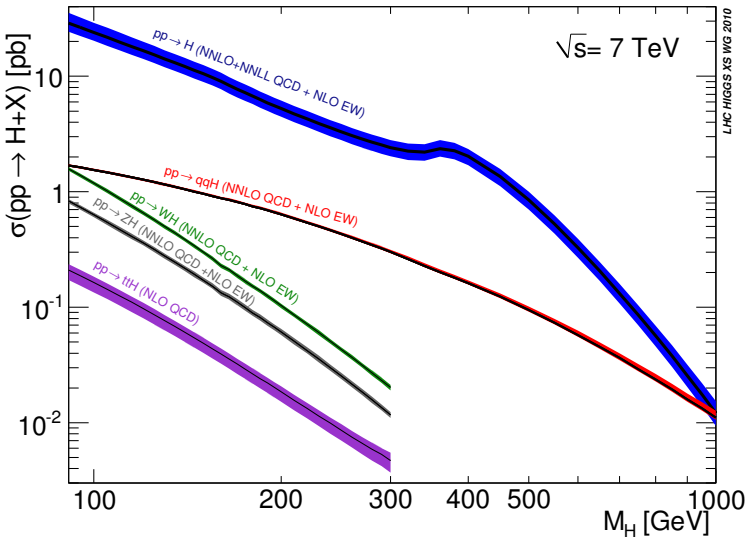

Figure 3.2: The SM Higgs production cross section with its theoretical uncertainties, as a function of M_H at LHC with 7 TeV of centre of mass energy [52]. The gluon gluon fusion channel (blue); the vector boson fusion (red); the associated production with W and Z bosons (green and grey respectively) and the associated production with $t\bar{t}$ pairs (purple).

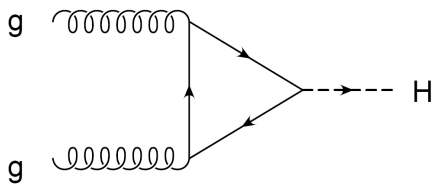

Figure 3.3: The one loop diagram, for Higgs production by gluon fusion.

probability amplitude as

$$\hat{\sigma}_{gg\to H} = \frac{1}{4F}(2\pi)\int \frac{d^3p_H}{2E_H}\delta^4(p_H - p_1 - p_2)\overline{|M_{fi}|^2} \tag{3.7}$$

where p_1, p_2 are the momenta of incoming gluons and the flux factor for two massless particles is

$$F = p_1 p_2 = \frac{\hat{s}}{2}, \tag{3.8}$$

and the phase space integration for the outgoing Higgs is equal to

$$\int \frac{d^3p_H}{2E_H}\delta^4(p_H - p_1 - p_2) = \delta(\hat{s} - M_H^2) \tag{3.9}$$

The squared probability amplitude $\overline{|M_{fi}|^2}$ is averaged over the physical initial states of the incoming particles: this gives a spin factor 1/2 and a colour factor $\frac{1}{(N_c-1)^2} = 8$, for each of the two gluons:

$$\overline{|M_{fi}|^2} = \left(\frac{1}{2}\frac{1}{(N_c-1)^2}\right)^2 |M_{gg\to H}|^2. \tag{3.10}$$

The squared matrix element $|M_{gg\to H}|^2$ is evaluated by the loop in Fig. 3.3, and it gives

$$|M_{gg\to H}|^2 = \left(\frac{\alpha_s}{\pi}\right)^2 \frac{M_H^4}{v^2} \left|\sum_Q A_Q^H(\tau_Q)\right|^2 \tag{3.11}$$

where v is the vacuum expectation value (see section 1.2), $\tau_Q = \frac{4M_Q^2}{M_H^2}$ where M_Q is the quark mass and the function $A_Q^H(\tau_Q)$ is

$$\begin{aligned} A_Q^H(\tau) &= \tau\big(1-(1-\tau)f(\tau)\big) \\ f(\tau) &= \begin{cases} -\arcsin^2\frac{1}{\sqrt{\tau}} & \tau \geq 1 \\ \frac{1}{4}\left(\log\left(\frac{1+\sqrt{1-\tau}}{1-\sqrt{1-\tau}}\right) - i\pi\right)^2 & \tau \leq 1 \end{cases} \end{aligned} \tag{3.12}$$

Collecting all together, we finally obtain [6]

$$\hat{\sigma}_{gg\to H} = \frac{\alpha_s^2}{\pi}\frac{M_H^4}{256v^2\hat{s}}\delta(\hat{s}-M_H^2)\left|\sum_Q A_Q^H(\tau_Q)\right|^2 \tag{3.13}$$

The Higgs-quark coupling is proportional to the quark mass, thus the biggest contribution in the sum $\sum_Q A_Q^H$ is given by the top quark. Furthermore, assuming the *large-M_t approximation* (i.e. $M_t \gg M_H$ or equivalently $\tau \to \infty$), we can expand the function $A_{top}^H(\tau)$ in terms of τ^{-1}

$$A_{top}^H(\tau) = \frac{2}{3} + \frac{7}{45}\frac{1}{\tau} + o(\tau^{-2}) \simeq \frac{2}{3}, \tag{3.14}$$

in this large-M_t approximation we obtain a simplified expression for the production cross section:

$$\hat{\sigma}_{gg\to H} = \frac{\alpha_s^2}{\pi}\frac{M_H^4}{576v^2\hat{s}}\delta(\hat{s}-M_H^2). \tag{3.15}$$

In the large-M_t approximation, the heavy quark loop is contracted to a point and we approximate it as an effective gluon-gluon-Higgs coupling. To include this interaction in the Lagrangian in a gauge invariant form, we have to add the following term

$$\mathcal{L}_H = -\frac{1}{4} g_H F^a_{\mu\nu} F^{a\mu\nu} H, \tag{3.16}$$

where g_H is the effective Higgs coupling constant and the factor $\frac{1}{4}$ is explicit to get vertices without combinatorial factors, where $F^a_{\mu\nu}$ is the gluon field strength tensor as Eq. (1.2). Expanding the gluon field strength tensor we obtain the ggH effective coupling

$$-\frac{1}{4}g_H\left(\partial_\mu G^a_\nu - \partial_\nu G^a_\mu\right)^2 H, \tag{3.17}$$

which leads to the following interaction vertex

$$V_2^H = ig_H\delta^{ab}\left(g^{\mu\nu}p_1p_2 - p_1^\nu p_2^\mu\right). \tag{3.18}$$

Expanding Eq. (3.16) we obtain three-gluon and four-gluon terms as well, leading to three-gluon-Higgs and four-gluon-Higgs effective couplings. In the limit of Higgs coupling g_H going to zero, the Higgs contribution goes to zero and the effective vertices turn into standard QCD.

Comparing the effective vertex of Eq. (3.16) with the exact cross section in Eq. (3.13) and the expansion in Eq. (3.14) we can extract the effective Higgs coupling

$$g_H = \frac{\alpha_s}{3\pi v}\left(1 + \frac{7}{3}\tau^{-1} + \dots\right) \tag{3.19}$$

thus the expression of Eq. (3.15) can be rewritten as

$$\hat{\sigma}_{gg\to H} = g_H^2\frac{M_H^4\pi}{64\hat{s}}\delta(\hat{s} - M_H^2). \tag{3.20}$$

The large-M_t approximation reduces the number of loops by one, considerably simplifying the computation of *higher order corrections*. The idea of effective coupling can be extended to higher perturbative orders generalizing the expression in Eq. (3.16) as follows

$$\mathcal{L}_H = -\frac{1}{4}g_H\left(1 + \frac{\alpha_s}{\pi}\Delta_{NLO} + \left(\frac{\alpha_s}{\pi}\right)^2\Delta_{NNLO} + \dots\right)F^a_{\mu\nu}F^{a\mu\nu}H, \tag{3.21}$$

where the Δ coefficients correspond to the higher order perturbative corrections.The NLO and NNLO corrections have been computed in Ref. [7] and Refs. [10, 11] respectively.

The production rate for $gg \to H$ has been computed to NLO in the large-M_t approximation [7, 8] and with the full (t and b) quark mass dependence [9]. The NLO corrections, due to diagrams as the ones in Fig. 3.4, increase the LO result of about $80-100\%$ leading to a significant change of the theoretical predictions. Moreover the LO and NLO uncertainties bands do not overlap, thus casting doubts on the reliability of the perturbative expansion (see Fig. 3.6). Anyhow, the prediction obtained by the effective Lagrangian approximation at NLO and the full QCD-NLO calculation are in good agreement up to $M_H = 1$ TeV, covering the entire Higgs mass range at the LHC (as shown in Fig. 3.5). The reason for this good agreement is that QCD corrections to $gg \to H$ are dominated

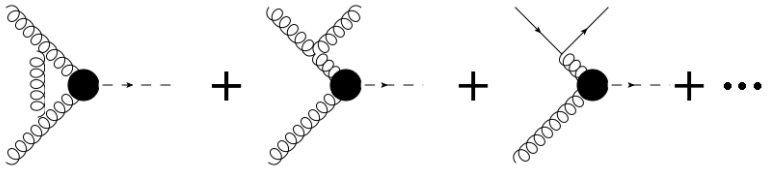

Figure 3.4: Diagrams contributing to the virtual (left) and real (center and right) QCD corrections at the NLO for the process $gg \to H$. The black dot stands for the LO effective vertex for $gg \to H$ and has to be substituted with the quark loop in a full NLO calculation.

by relatively soft gluon emissions and such radiation is weakly sensitive to the mass of the heavy quark circulating in the loop [53]. The NNLO corrections have been evaluated in the large-M_t approximation [12, 13, 14, 15]. The total cross section increases by about 25% at the LHC (with 7 GeV of CME) with respect to the NLO result and in this case the uncertainty bands overlap, thus indicating the NNLO prediction is more reliable.

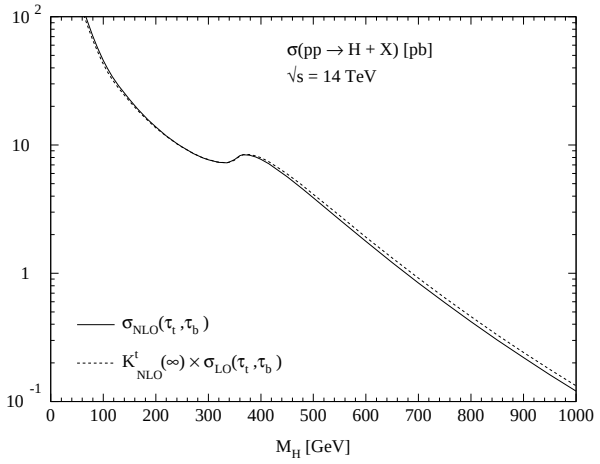

Figure 3.5: From Ref. [10], comparison of exact and approximate NLO predictions (in the large-M_t approximation) for the total cross section for Higgs production, as function of the Higgs mass.

The contributions from multiple soft gluon emission have been calculated by *threshold resummation at the next-to-next-to-leading-log*[1] (NNLL) [54], and their effects increases the predictions by about 8%. Finally also electroweak corrections were considered in Ref.

[1] We will provide a brief overview of the resummation procedure in the next chapter.

[55]. A comparison of the best available theoretical predictions at the (NNLO+NNLL)-QCD with NNLO-QCD+NLO-EW is shown in Fig. 3.7.

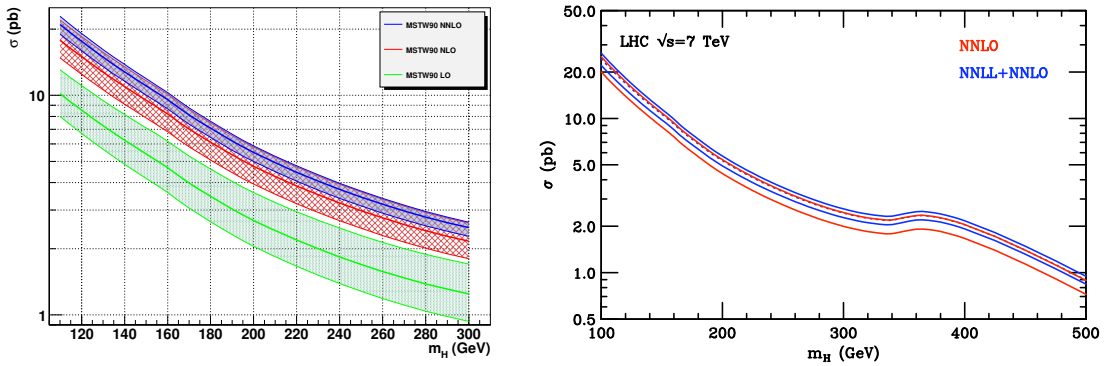

Figure 3.6: On the left [56]: the total Higgs production cross section at the LHC $\sqrt{s} = 7$ TeV, with perturbative uncertainties calculated at various perturbative orders. On the right [57]: the same predictions at NNLO compared with the threshold resummation result at NNLL+NNLO.

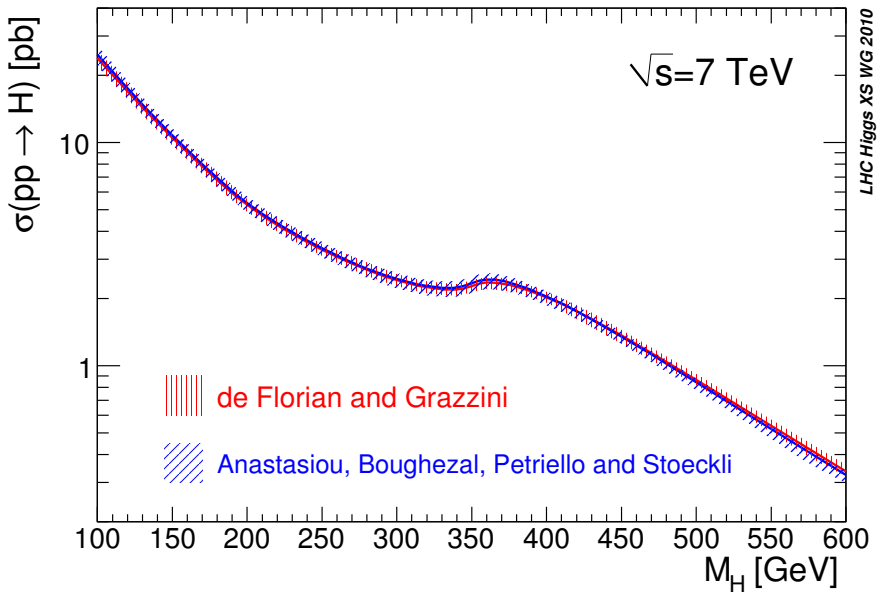

Figure 3.7: Comparison of the best theoretical predictions for the Higgs production cross section (including the uncertainty bands) as function of its mass [52].

3.2.2 Overview on other Higgs production channels

There are other important Higgs production mechanisms at hadron colliders, that can be useful in order to detect the Higgs boson and to study its properties.

The *Vector Boson Fusion* mechanism occurs as the scattering between two (anti)quarks mediated through the exchange of a weak boson in the t-channel and the Higgs boson is radiated by the vector boson (V^*), as shown in Fig. 3.8. This is a very promising channel

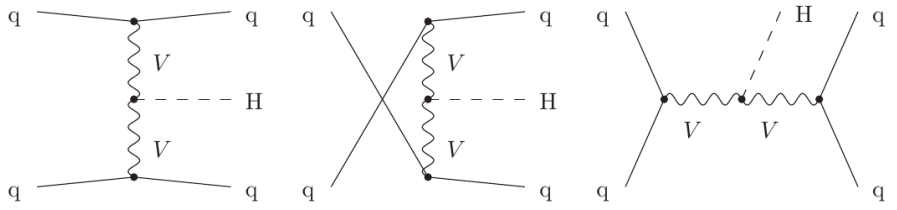

Figure 3.8: The tree level Feynman diagrams for the Vector Boson Fusion fusion $qq \to qqV^*V^* \to qqH$, in the $t-$, $u-$ and $s-$channel.

at the LHC for various reasons. The two quarks tend to be produced with a large rapidity interval between them and thus they offer a quite distinctive signature in the detectors. The cross section is about 20% of the gluon fusion one and becomes comparable to the latter in the high mass range ($M_H \gtrsim 500$ GeV). The theoretical prediction has a small uncertainty, of the order of about 5%. The LO cross section has been computed in Ref. [58], then the full NLO EW+QCD calculation can be found in Ref. [59, 60, 61] and the prediction has a scale uncertainty of about 5%. An estimate of the NNLO QCD corrections can be found in Ref. [62]: it indicates a small perturbative uncertainty of the order of about 1-2%. These phenomenological features make this a key process for precise measurement of the Higgs boson mass and couplings at the LHC. In particular it is an ideal channel for the measurement of the HWW and HZZ couplings.

The *Associated production with W and Z* vector bosons (also called Higgs-strahlung mechanism) is given by Drell-Yan vector boson production, followed by an Higgs emission by the vector boson ($q\bar{q} \to V^* \to VH$), see Fig. 3.9. This channel is considered mainly by exploiting the two decay channels $H \to WW$ and $H \to b\bar{b}$, both accompanied with the Drall-Yan vector boson decaying into leptons (in order to obtain a more clear experimental signature).

The cross section has been computed at LO in Ref. [63]; the NLO and the bulk of NNLO QCD corrections can be obtained using the available results from the Drell-Yan calculations [59, 64]. Also the NLO EW corrections have been calculated [65], but the combination of the two NLO results is a non trivial task [66].

Associated production with $t\bar{t}$ pairs (also called Higgs bremsstrahlung off top quarks).

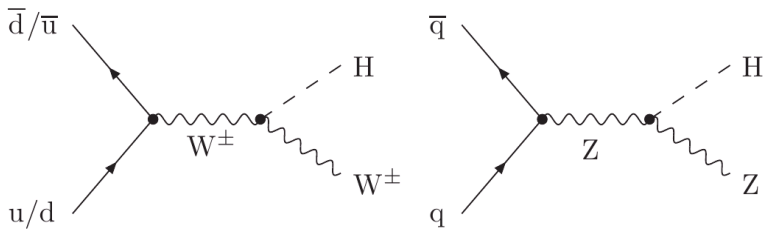

Figure 3.9: Leading order Feynman diagrams for the associated production with V^* (Higgs-strahlung mechanism).

In this process a $t\bar{t}$ pair is created by the annihilation of a $q\bar{q}$ or gg pair, and the Higgs boson is emitted by the (anti)top quark, see Fig. 3.10.

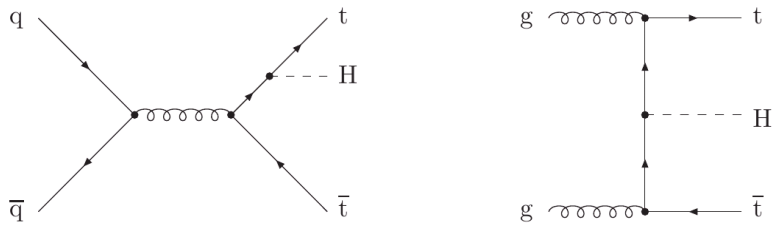

Figure 3.10: Leading order Feynman diagrams for the associated production with $t\bar{t}$ quark pairs.

The LO cross section was calculated in Ref. [67] and the result has a large theoretical uncertainty; the NLO QCD correction have been calculated in Ref. [68], the resulting prediction moderately increases the total cross section (at the LHC by at most $\sim 20\%$), and (more importantly) significantly decreases the theoretical uncertainty. The measurement of the $t\bar{t}H$ production rate can provide relevant information on the top-Higgs Yukawa coupling.

The associated production with a top quark pair, in combination with Higgs decay to bottom quark pair, has a long history. At some point it was expected to be the leading discovery channel for a light Higgs boson [69], but afterwards it was left out due to a (too) low signal-to-background ratio [70]. Recently a boosted analysis [71] was introduced. It was shown that studying fat jets substructure can reveal its heavy-particle origin. Hence boosted analysis could provide to this search channel reasonable statistical significance and (most importantly) allow an important reduction of systematics sensitivity.

3.3 Higgs boson decay modes

The Higgs boson can directly decay into pairs of all massive particles and through loops even into pairs of massless photons and gluons.

If the Higgs particle will be discovered, it will be important to study several Higgs decay channels in order to measure the corresponding couplings and to compare them with the SM predictions. The strength of the Higgs boson interaction grows with the particle mass (as shown in Table 1.1): as a consequence the Higgs decays predominantly into W and Z vector bosons and b, t heavy quarks, when kinematically allowed. The branching ratios for the main decay modes are shown in Fig. 3.11.

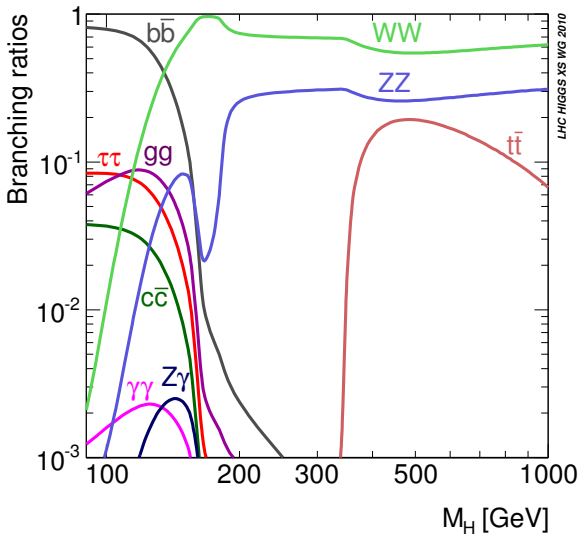

Figure 3.11: Branching ratios of the dominant decay modes as function of the Higgs boson mass [51, 52].

Higgs decay into two fermions: leptons and heavy quarks

We start considering fermion decays that can be classified into electroweak and strong decays. The first ones are more useful because they lead to a clean signature in the detectors (we recall that at hadron colliders there is a huge production of strong interacting particles, that at the end manifest themselves to jets).

At the LO [72] the Feynman diagram is the same for all fermion-decays as Eq. 3.22. The only difference is in the coupling (proportional to the squared mass of the fermions) and in the colour factor: $N_c = 3$ for quarks and $N_c = 1$ for leptons.

$$\Gamma_{H \to f\bar{f}} = \frac{N_c^2 \, g^2 \, M_H \, M_f^2}{32\pi \, m_W^2} \left(1 - \tau_f\right)^{3/2} \tag{3.22}$$

where $\tau_f = \frac{4M_f^2}{M_H^2}$.

Electroweak corrections to this formula are known [73] and QCD corrections are known at the NLO [73], NNLO [74] and up to three loops [75].

From a phenomenological point of view none of the fermionic decay channel is promising for the Higgs discovery. The $b\bar{b}$ decay channel starts to be considered in the low Higgs mass range [76], thanks to the branching ratio almost close to one and the improved statistical techniques. In future, increasing the integrated luminosity, the $b\bar{b}$, $\mu^+\mu^-$ and $\tau^+\tau^-$ decays could be useful in order to test the Higgs couplings that are sensitive to new physics signals (especially SuperSymmetry [77]).

Higgs decay in two gluons

The Higgs decay into gluons suffers of the same experimental problems as the quarks decay, and also it has a quite small branching ratio over the entire Higgs mass range. It is interesting to consider it, because it can be calculated from the gluon fusion calculation for the Higgs production. In this case, the two calculations have the same Feynman diagram and thus the same squared matrix element and the differences are only in the phase space, the colour-spin average and flux factors. Thus we can write:

$$\hat{\sigma}_{gg\to H} = \frac{8\pi^2}{N_g^2\, M_H}\delta(\hat{s} - M_H^2)\,\Gamma_{H\to gg} \tag{3.23}$$

where $N_g = 8$ is the number of gluons, and using the definition of Eq. (3.12) we obtain the LO decay width:

$$\Gamma_{H\to gg} = \frac{G_F\alpha_s^2 M_H^3}{36\sqrt{2}\pi^3}\left|\sum_Q A_Q^H(\tau_Q)\right|^2 \tag{3.24}$$

QCD corrections turn out to be very large: at NLO [7, 8] the decay width is shifted by about $60-70\%$ upwards in the intermediate Higgs mass range. Three loop QCD corrections have been evaluated [75] and they increase the NLO prediction by about $\sim 10\%$: they signal a stabilisation of the perturbative result and suggest a reliable theoretical prediction.

Higgs decay in two photons

As for the Higgs decay into gluons, the Higgs decay into photons is mediated by heavy fermion loop and also by W boson loop. The partial decay width can be written as [78]

$$\Gamma_{H\to\gamma\gamma} = \frac{G_F\alpha^2 M_H^3}{128\sqrt{2}\pi^3}\left|\sum_Q n_f e_f^2 A_Q^H(\tau_Q) - A_W^H(\tau_W)\right|^2 \tag{3.25}$$

where $n_f = 3$ is the number of flavours and e_f is the fermion electric charge, $\tau_i = 4m_i^2/M_H^2$ where m_i is the mass of heavy particle in the loop, A_f^H is defined as usual Eq. (3.12) and the A_W^H is the W contribution

$$A_Q^H(\tau) = \left(1 + \frac{3}{2}\tau + \frac{3}{2}\tau(2-\tau)f(\tau)\right) \tag{3.26}$$

Note that fermion and W contributions interfere destructively. In the intermediate Higgs mass range the W loop dominates and for $M_H \sim 600$ GeV they nearly cancel. Despite this decay channel is quite suppressed, it is one of the most important in the Higgs search in the low mass region (around $M_H \sim 120$ GeV), thanks to excellent resolution of the ATLAS and CMS detectors.

Two-loop [79] and three-loop [80] QCD corrections have been calculated giving very accurate predictions with small theoretical uncertainties. At NLO, QCD corrections consist only of virtual corrections by gluon exchange inside the triangle (charge conjugation invariance and colour conservation forbid radiation of a single gluon).

A similar decay is the $H \to Z\gamma$; it can be calculated [81, 82] in complete analogy with the di-photon case, but from the experimental point of view this decay channel is not very much considered at least for the Higgs boson discovery.

Higgs decay into vector bosons

One of the most important decay channels is the Higgs decay into two vector bosons, such as W^+W^- or Z^0Z^0, because this is EW decay and it is dominant in the high mass region.

The LO [83] partial width into vector boson is expressed as follows

$$\Gamma_{H\to VV} = \delta_V \frac{G_F M_H^3}{8\sqrt{2}\pi}\sqrt{1-x}(1 - x + \frac{3}{4}x^2) \tag{3.27}$$

where $x = 4M_V^2/M_H^2$. The factor δ_V is equal to 1 for W^+W^- and to 1/2 for Z^0Z^0, and it is due to the identity of final state particle in the case of Z^0Z^0 decay.

QCD corrections are known up to three loops [84] and enhance the decay width of about 20%; also EW corrections are known up to one loop level [73] and amount to about 5%.

Unfortunately also vector bosons cannot be directly observed in the detectors and we have to consider their decays. Below the threshold the Higgs decaying into off shell gauge bosons pairs play a significant role. For these decays analytic expressions are available in Ref. [82] and they are encoded in the Monte Carlo program `PROPHECY4F` [85] that provides the LO and NLO partial widths for any possible 4fermion final state, including the complete NLO QCD and electroweak corrections and all interference at LO and NLO.

3.4 Main search strategies at hadron colliders

The SM Higgs production cross section (Fig. 3.2) is dominated, over all the Higgs boson mass range, by the gluon gluon fusion process. On the other hand (from Fig. 3.11) it is clear that the branching ratios change dramatically by varying the Higgs boson mass. Then it is necessary to have different strategies for the Higgs identification depending on its mass.

The naive idea that the search is dictated by the Higgs decay rate is not always working. In an experimental analysis, one wants to be able to separate the signal from background events and this means that the signature of a given search mode needs to be clean. The decay products must be unambiguously identifiable and their kinematic properties well measurable. Typically, fully hadronic Higgs decays are abundant at the LHC and the Tevatron, but one prefers electroweak decays, that, even if produced with lower rate, are easier to separate from the background.

With this in mind, we can identify the most promising channels for Higgs searches depending on the Higgs mass range (for a more detailed discussion see for example Ref.[86]).

Low-mass Higgs: $M_H \lesssim 140$ GeV

The $H \to b\bar{b}$ decay is dominant in the low-mass range $M_H \lesssim 140$ GeV, but it is almost un-exploitable at hadron colliders due to the huge amount of background (the direct $b\bar{b}$ production cross section is ~ 10 orders of magnitude bigger!). If the Higgs boson production is associated to other identifiable particles (as in the cases of Higgsstrahlung and perhaps Vector boson fusion) it helps to reduce the QCD background. Unfortunately the production rates in these channels are rather small. Thus significant integrated luminosity needs to be accumulated in order make the $b\bar{b}$ decay a significant channel for Higgs searches.

The next channel at low masses is the $H \to \tau\tau$ mode. The τ leptons decay either hadronically ($\sim 85\%$) either to detectable leptons ($\sim 15\%$). The comparison signal/background makes this channel difficult for Higgs searches. It can be useful if enough integrated luminosity will be accumulated.

The main search mode in this low mass region is the *two photon decay* $H \to \gamma\gamma$. Although the branching ratio is very small this channel is very clean. The signature is two well identified photons and this provides a clean though small peak in the invariant mass distribution.

Part of this thesis is devoted to obtain an accurate prediction for photon distributions in this decay channel ($H \to \gamma\gamma$), that could lead to improve the statistical significance.

Intermediate-mass Higgs: $140\ \text{GeV} \lesssim \text{M}_\text{H} \lesssim 180\ \text{GeV}$

In the intermediate-mass range $140\ \text{GeV} \lesssim \text{M}_\text{H} \lesssim 180\ \text{GeV}$, the decay $H \to WW$ dominates because the branching ratio is almost one and practically the Higgs boson decays exclusively in this mode. The W bosons decay both leptonically and hadronically. The fully hadronic decay is almost unexploitable again due the enormous QCD background. The semi-leptonic decay (one W decays leptonically and the other one hadronically) have a signature consisting of 2 jets, one lepton and missing energy due the undetected neutrino. In case of Higgs boson production through the vector boson fusion the two forward jets produced in the initial state helps to discriminate Higgs events from the backgrounds, but again this channel is suppressed by smaller production rate [87]. The golden search channel in this Higgs mass range is when both the W decay leptonically $H \to W^+W^- \to l^+\nu l^-\nu$. In this case the signature consists of two well identified leptons plus missing energy, leading to unbalanced momentum in the transverse momentum plane. This channel has two opposite features: it is the most useful to make experimental exclusions at hadron colliders (the first Higgs exclusion at the Tevatron was made in this channel [88]), but in case of Higgs discovery it is very hard to use it to measure the Higgs mass due the missing energy. This decay ($H \to W^+W^- \to l^+\nu l^-\nu$) is also subject of study, in this thesis.

High-mass Higgs: $M_H \gtrsim 180\ \text{GeV}$

Although also in the high-mass region $M_H \gtrsim 180$ GeV, the dominant decay is $H \to WW$, the Higgs is massive enough to create two Z bosons. The Z boson can decay either leptonically or hadronically. In case of both Z boson decaying into detectable leptons (muons or electrons) we can fully reconstruct the invariant mass of the system (as in the $H \to \gamma\gamma$ case). Thus even with smaller branching ratio, if compared with the $H \to WW$ one, this is considered a *gold plated* channel at high mass.

This decay channel is subject of study in this thesis as well; in particular we will study the differential lepton distributions for the decay modes: $H \to ZZ \to \mu^+\mu^-e^+e^-$ and $H \to ZZ \to e^+e^-e^+e^-$.

Finally, both the decay channels $H \to W^+W^- \to l^+\nu l^-\nu$and $H \to ZZ \to 4l$ are also useful for the Higgs searches in the low mass range.

Chapter 4

Transverse momentum spectrum of the Higgs boson

In order to search for the Higgs boson and to study its properties, the theoretical knowledge of the total production cross section is not enough. This is a general feature of high energy particle physics, because the total cross section is only an ideal quantity and it is not directly measurable in real detectors. It is impossible to build a detector that can reveal all the particles: first the detector has a certain efficiency that depends on the materials, technology, software analysis, etc.. and also it has a finite geometrical acceptance: as we can see in Fig. 4.1 the detector can reveal the particle A passing through the detecting materials, but the particle B that is produced almost in the direction of the colliding protons escapes from the detector and it is not revealed. Each detector has some blind regions and it cannot access the particles produced in such regions. From the experimental point of view differential cross sections are more useful, since they allow to take into account this problem and can be quantitatively measured.

Moreover, differential distributions as a function of other variables (angles, momenta, etc.) provide further information on the process, allowing to test specific features of the particles (such as spin, parity, couplings, charges...) or their interactions. For example by studying 4-jets events at LEP, if the jets are ordered by energy, $E_1 > E_2 > E_3 > E_4$, we arrive at the definition of the angular correlation variable called Bengtsson-Zerwas angle:

$$\chi_{\mathrm{BZ}} = \frac{(\mathbf{p}_1 \times \mathbf{p}_2) \cdot (\mathbf{p}_3 \times \mathbf{p}_4)}{|\mathbf{p}_1 \times \mathbf{p}_2| \cdot |\mathbf{p}_3 \times \mathbf{p}_4|} \tag{4.1}$$

where $\mathbf{p}_i$, i = 1, . . . , 4 are the energy-ordered momenta of the four partons (jets). In Fig. 4.2 LEP measurements of χ_{BZ} are compared with the predictions of QCD and of an abelian model with three quark colors, but no three-gluon coupling. The data provide evidence that QCD is indeed the correct theory to describe this process.

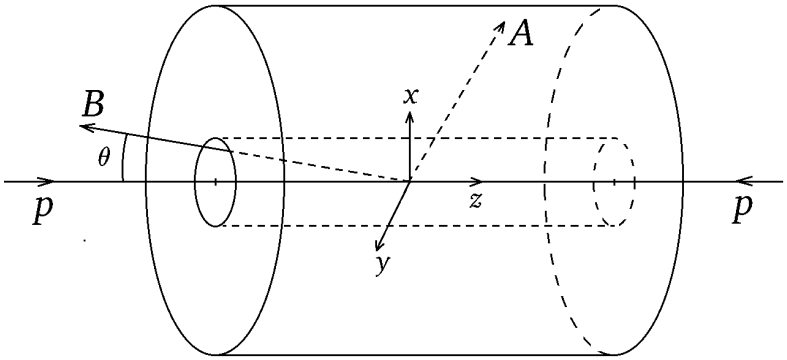

Figure 4.1: The typical geometry of a high energy particle detector. The particle A is produced in a direction that can be measured in the detector, instead the particle B escapes without been revealed.

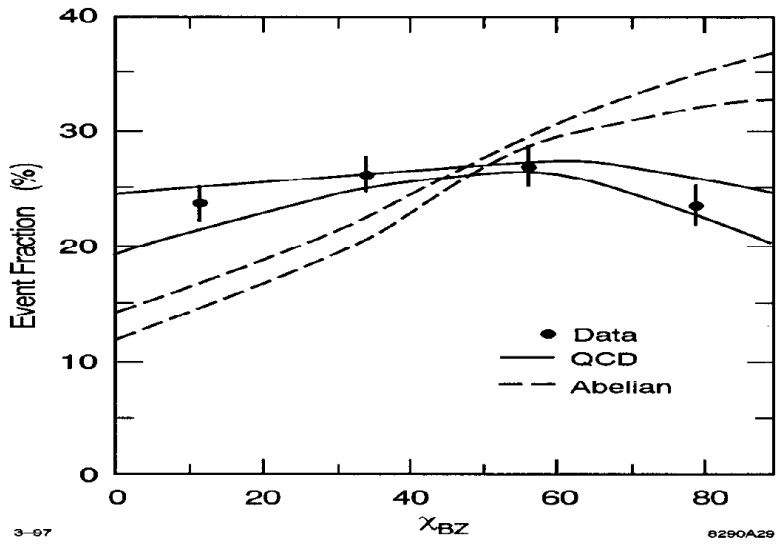

Figure 4.2: Distribution of $\chi_{\rm BZ}$ measured by the L3 collaboration [89]. The predictions for QCD and the abelian model are shown as bands indicating the theoretical uncertainties.

In order to describe the full kinematic of a particle we need its four-momentum, e.g. its energy and the three spatial momenta (E, p_x, p_y, p_z). In hadron colliders such as Tevatron and the LHC, the colliding particles are un-polarised, thus the processes are cylindrical symmetric. The particle spatial momenta can be described in cylindrical coordinates as (p_T, θ, p_z) where we choose the z axis as the beam pipe direction, $p_T = \sqrt{p_x^2 + p_y^2}$ is the modulus of the momentum in the transverse plane xy and $\phi = \arctan(p_y/p_x)$ is the azimuthal angle in the transverse plane. Thanks to the cylindrical symmetry of the

problem, for most of the processes we can forget the ϕ variable and consider only the kinematical distributions in the variables (p_T, p_z). In the literature and in the following of this thesis, the transverse momentum p_T is often called q_T or k_T.

The transverse momentum is Lorentz invariant under boosts in the z direction and it is thus useful when changing the frame between the rest frame of the partonic collision and the laboratory frame. On the contrary the p_z depends on the frame and it is thus convenient to define the *rapidity* y as

$$y = \frac{1}{2} \ln \frac{E + p_z}{E - p_z} = \tanh^{-1} \frac{p_z}{E}. \tag{4.2}$$

Under a boost with velocity β in the z direction the rapidity transforms as

$$y \to y - \tanh^{-1} \beta, \tag{4.3}$$

hence the shape of rapidity distributions dN/dy is Lorentz-invariant. For $p \gg m$ or for massless particles, we can expand the Eq. (4.2) in terms of θ (where $\cos\theta \equiv p_z/p$), obtaining

$$y = \frac{1}{2} \ln \frac{\cos^2(\theta/2) + m^2/(4p^2) + \dots}{\sin^2(\theta/2) + m^2/(4p^2) + \dots} \simeq -\ln \tan\left(\frac{\theta}{2}\right) \equiv \eta \tag{4.4}$$

η is by definition the *pseudorapidity* and the distributions on the η variable are Lorentz-invariant.

In order to describe the Higgs boson production, we retain the full kinematical information through the double differential transverse momentum and rapidity distribution. When dealing with the Higgs boson decay, the same distributions are useful as well, and also more elaborate observables that we will define in the next chapters.

4.1 Production: rapidity and PDFs

The rapidity distribution for Higgs boson production $d\sigma/dy$ is shown in Fig. (4.3).

In order to discuss the main features of the shape of the rapidity distribution, we insert the LO formula for Higgs production through gluon fusion Eq. (3.15) in the factorisation formula Eq. (2.30). Thus we can rewrite Eq. (2.31) as follows

$$x_i x_j = \left(\frac{M_H^2}{s}\right) \equiv \tau, \tag{4.5}$$

where at the LHC $\tau \sim (10^{-3}\text{–}10^{-4}) \ll 1$. In other words, the constraint $\delta(\hat{s} - M_H^2)$ implies that the two parton distribution functions are evaluated at values of the Bjorken x such that

$$x_j = \frac{\tau}{x_i}. \tag{4.6}$$

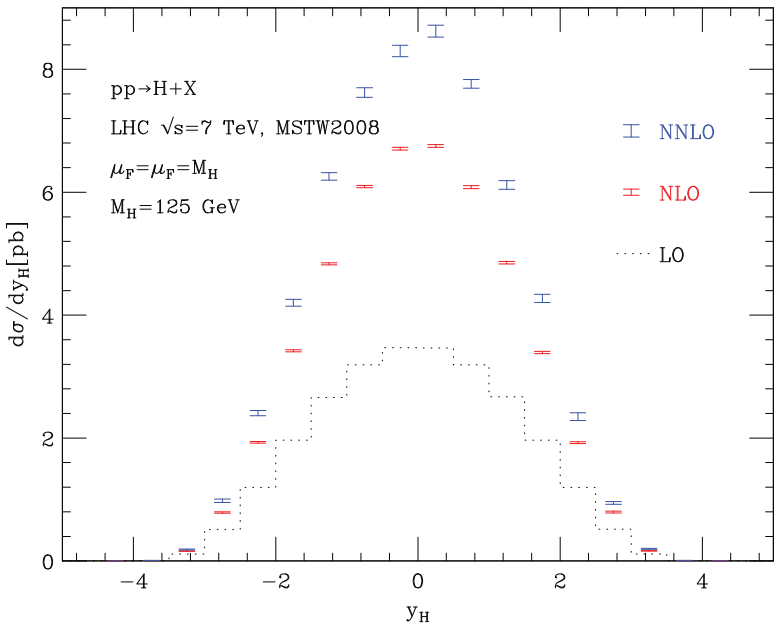

Figure 4.3: The rapidity distribution for Higgs boson production at various perturbative orders, obtained by the `HNNLO` numerical code [90, 91]. In this example we show the spectra at the LHC for $\sqrt{s} = 7$ TeV and $M_H = 125$ GeV calculated with MSTW2008 PDFs.

As we can see from Fig. 2.5, the PDFs $f_i(x)$ vanish in the limit $x \to 1$ whereas for $x \to 0$ they are strongly enhanced. However the vanishing in $x \to 1$ is stronger than the enhancement in the small x region:

$$\lim_{x\to\tau} f_i(x) f_j(\tau/x) = 0. \tag{4.7}$$

The gluon PDFs product is instead maximised is the region $x_1 \sim x_2$.

On the other hand, we can calculate the Higgs rapidity y_H starting from the particle momenta in the high energy limit. In the CME frame the hadron momenta can be written as $P_{1/2} = (E, 0, 0, \pm p_z) \simeq E(1, 0, 0, \pm 1)$ and the parton momenta are respectively $p_{1/2} \simeq x_{1/2} E(1, 0, 0, \pm 1)$. The Higgs momentum is thus $p_H = p_1 + p_2 = E(x_1 + x_2, 0, 0, x_1 - x_2)$ and inserting this expression in Eq. (4.2) we obtain the Higgs rapidity as function of the Bjorken variables $x_{1/2}$

$$y_H = \frac{1}{2} \ln \frac{x_1}{x_2}. \tag{4.8}$$

Comparing the results in Eqs. (4.6,4.7,4.8) it is clear that the Higgs rapidity distribution is maximised in the central region $y \simeq 0$ (or equivalently $x_1 \sim x_2$) and suppressed at high values of $|y|$ ($x_i \ll x_j$). Furthermore Eq. (4.8) is antisymmetric under exchange $x_1 \leftrightarrow x_2$

and as a consequence the Higgs rapidity distribution is symmetric for $y_H \leftrightarrow -y_H$ both in pp and $p\bar{p}$ collisions.

Finally if we set $x_j = 1$ in Eq. (4.5) and using Eq. (4.8) we obtain the kinematical limit for the Higgs rapidity

$$y_H^{max} = \frac{1}{2} \ln \frac{s}{M_H^2} = \ln \sqrt{\frac{s}{M_H^2}}. \tag{4.9}$$

For example, if we consider $M_H = 125$ GeV as in Fig. 4.3 we have the LO rapidity limit: $y_H^{max} = \ln(7000/125) \simeq 4.025\ldots$

Considering *higher perturbative orders*, the behaviour of the rapidity distribution is essentially driven by the PDFs. Its shape is mildly dependent on radiative corrections as we can see in Fig. 4.4, where we show the normalized rapidity distributions at LO, NLO and NNLO.

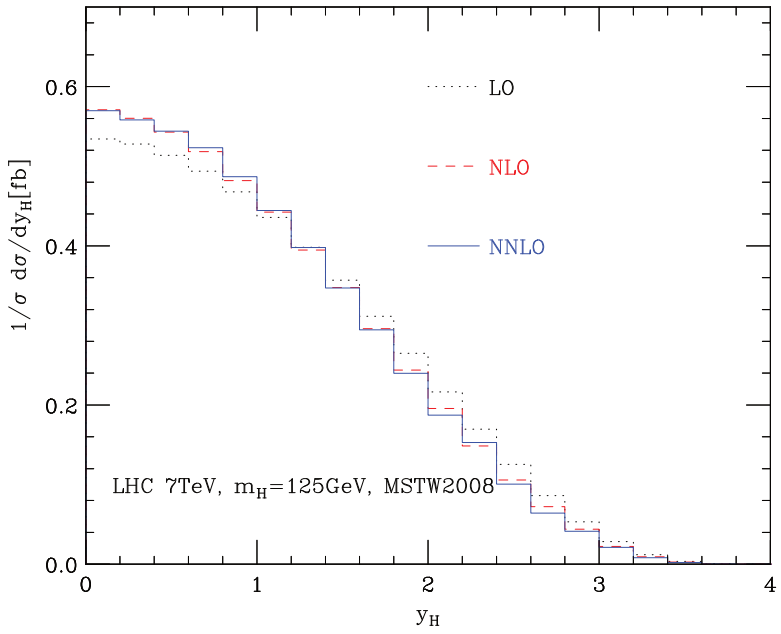

Figure 4.4: The normalized rapidity distribution for Higgs boson production at the LO, NLO and NNLO, obtained by the `HNNLO` numerical code [90]. In this example we show the LHC spectra, at 7 TeV C.M.E. for $M_H = 125$ GeV calculated with MSTW2008 PDFs.

4.2 Production: transverse momentum spectrum

Due to momentum conservation, at the LO in the gluon fusion channel the Higgs boson is produced with zero transverse momentum, while at higher orders the q_T is typically non-

zero thanks to QCD radiation from initial state partons (see Fig. 3.4). For this reason, we conventionally call LO(NLO) transverse distribution distribution the one obtained by using real terms contributing for the NLO(NNLO) total cross section.

Furthermore we know from detailed analysis that a good knowledge of the q_T distribution shape can help to improve triggering strategies [92]; also one can see that signal and background have different shapes, thus an optimised choice of experimental cuts allows an improvement of the statistical significance of data analysis. For example the Higgs q_T spectrum is expected to be harder than the $\gamma\gamma$ background one. An optimised choice of cuts allows improvement in the reconstruction of recoiling jet(s) in the calorimeters, leading to a more precise determination of interaction vertex and improving efficiency and mass resolution [93]. Analogous improvements can be obtained in the other decay channels, see for example Ref. [94]. In summary *an accurate prediction of the q_T distribution can be extremely useful in the Higgs boson search.*

As discussed in Section 3.2.1, in the large-M_t approximation the calculations are greatly simplified by using the effective field theory (EFT), in which the top quark is integrated over. In Fig. 4.5 we show the comparison between the exact and EFT predictions at LO: at low and medium q_T the two results are in very good agreement, their difference instead increases at high q_T. The physical explanation of this feature is simple. At the LO, the recoiling gluon is emitted with opposite transverse momentum with respect to the Higgs boson; at low q_T it has a large de-Broglie wavelength and thus its energy is not enough to resolve the quark loop, and an effective point-like interaction works well. On the contrary if the emitted gluon is highly energetic (gluon energy bigger than the top-mass) its wavelength is able to resolve the loop effects, that start to be important.

In any case, the LO calculations provide just an estimate of the actual result and typically the scale uncertainties are quite large. Sometimes such scale uncertainties underestimate the true theoretical uncertainty, as it happens for the total production cross section of the Higgs boson (see Fig. 3.6) and also for its transverse momentum distribution.

In order to obtain the NLO predictions a large number of Feynman diagrams have to be evaluated [95]. The phase space integration of the amplitude has been performed first numerically [96] and then analytically [97]. These calculations have been performed in the large-M_t approximation.

A comparison of the predictions for the transverse momentum differential cross section, with scale uncertainties at LO and NLO is shown in Fig. 4.6. Both the predictions decreases monotonically with increasing q_T, the scale dependence is almost $\pm 50\%$ at the LO and it is reduced to $\pm 30\%$ at the NLO, but (as for the total cross section) the scale

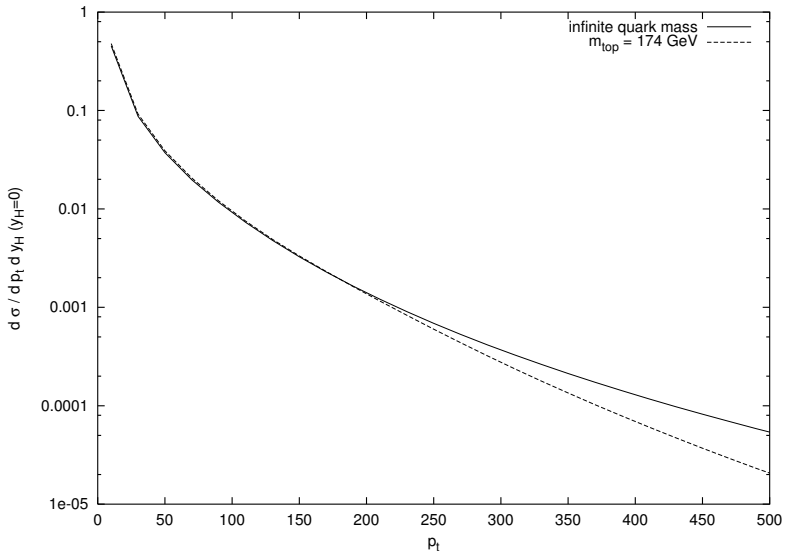

Figure 4.5: Comparison of the exact leading-order q_T spectrum with the effective theory calculation at LHC 14 TeV for $M_H = 120$ GeV, from Ref. [98].

variations at the LO hardly estimate higher order perturbative corrections. The NLO prediction is from 100% to 70% higher than the LO prediction and only in the high q_T region the error bands overlap. Note that in the intermediate and high q_T region, the prediction is quite strongly dependent on the PDFs set: in other words the LO and NLO error bands may not overlap for all the predictions obtained with different parametrisations of the PDFs.

4.3 Fixed order failure in the low q_T region

The fixed order calculations for the Higgs boson production provide a reliable tool to predict the Higgs transverse momentum spectrum for the large q_T region ($q_T \sim M_H$). However the bulk of events is expected in the low q_T region ($q_T \ll M_H$), where unfortunately the fixed order calculations loose their predictivity. In fact the emission of soft and collinear radiation from incoming partons *enhances* the coefficients of the perturbative expansion in α_s by *powers of logarithmic terms*, as we can see in Fig. 4.7. These logarithms spoil the convergence of perturbative contributions. In the low q_T limit, the differential cross section at the LO diverges to infinity; at the NLO there is an unphysical peak due to the compensation of negative leading and positive sub-leading logarithmic contributions and then the differential cross section diverges to minus infinity.

For example, in the $q_T \to 0$ limit the explicit expression for the LO differential cross

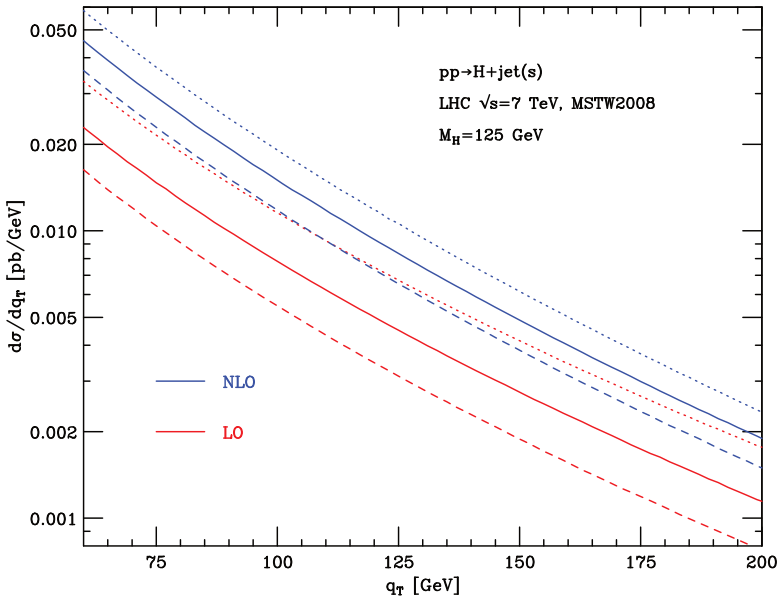

Figure 4.6: The LO (red) and NLO (blue) predictions for q_T differential cross section at LHC 7 TeV for $M_H = 125$ GeV, obtained with MSTW2008 PFDs set. The central value $\mu_F = \mu_R = M_H$ is reported with solid lines, the uncertainty bands are evaluated by scale variations: $\mu_F = \mu_R = M_H/2$ (dotted lines) and $\mu_F = \mu_R = 2M_H$ (dashed lines).

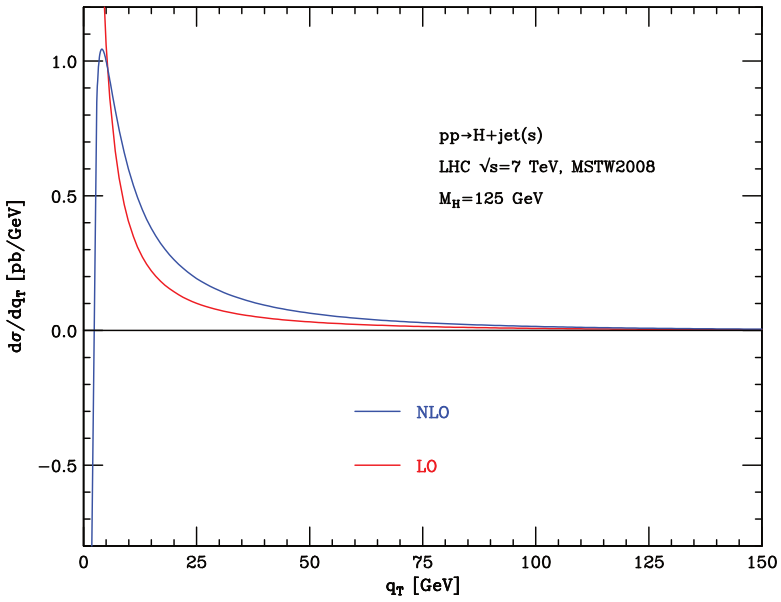

Figure 4.7: The LO and NLO predictions in low q_T region, for q_T differential cross section at LHC 7 TeV for $M_H = 125$ GeV, with MSTW2008 PDFs set.

section $gg \to Hg$ is

$$\frac{d\hat{\sigma}_{gg}}{dq_T^2} = \frac{\alpha_s}{\pi}\frac{\sigma_0}{\hat{s}}\frac{M_H^2}{q_T^2}\left[\left(2C_A \log\left(\frac{M_H^2}{q_T^2}\right) - 2\beta_0\right)\delta(1-z) + 2P_{gg}^{(0)}(z)\right] + O(q_T^2) \tag{4.10}$$

where $z = M_H^2/\hat{s}$ and $C_A = 3$, β_0 is the first coefficient of the β function (see Eq. 2.12) and $P_{gg}^{(0)}$ is the first term in the expansion of the Altarelli-Parisi splitting function (see Eq. 2.41), whose explicit expression is[1]

$$P_{gg}(z) = C_A\left[\frac{z}{(1-z)_+} + \frac{1-z}{z} + z(1-z)\right] + \delta(1-z)\frac{11C_A - 2n_f}{12}. \tag{4.12}$$

This partonic cross section is enhanced in the low q_T region by the presence of terms such as $\frac{M_H^2}{q_T^2}\log\left(\frac{M_H^2}{q_T^2}\right)$, and in general the n-th perturbative order will contain large logarithmic corrections $(\alpha_s^n/q_T^2)\log^m\left(\frac{M_H^2}{q_T^2}\right)$ with $m \leq 2n-1$. For example at the NLO, the partial compensation of the positive leading ($m = 2n-1$) and sub-leading ($m = 2n-2$) contributions gives rise to the un-physical peak of the differential distribution. Higher orders contain further powers of logarithmic terms, and the presence of these enhanced terms spoil the convergence of the perturbative series.

In order to obtain reliable predictions, these enhanced terms have to be systematically *resummed* to all orders in α_s. This procedure is typically observable-specific but allows us to consistently take into account the large logarithmic terms, thus achieving reliable physical predictions.

4.4 Resummation: general features

The resummation idea is briefly explained by the following argument: we define L as the logarithm of ratio of relevant scales involved in the process under investigation. In our case for example

$$L \equiv \log\left(\frac{M_H^2}{q_T^2}\right). \tag{4.13}$$

The standard perturbative expansion of a physical observable R is given by:

$$R = R_0\left[1 + \sum_{n=1}^{\infty}\alpha_s^n\left(a_{n,2n}L^{2n} + a_{n,2n-1}L^{2n-1} + a_{n,2n-2}L^{2n-2}\cdots + a_{n,1}L + a_{n,0}\right)\right], \tag{4.14}$$

[1] A *plus distribution* $g(x)_+$ (as in our case $1/(1-x)_+$) is defined through a sufficiently smooth test function $f(x)$, so that its integral is by definition

$$\int_0^1 dx\, f(x)g(x)_+ \equiv \int_0^1 dx\,\big(f(x) - f(1)\big)g(x); \tag{4.11}$$

an alternative definition is $g(x)_+ = g(x)\big(1 - \delta(1-x)\big)$.

where $a_{n,m}$ are the perturbative coefficients related to the terms $\alpha_s^n L^m$. In the region in which the logarithmic terms are of the order of unity (in our case when $q_T \sim M_H$) we recover the standard of fixed order expansion, where the convergence of the perturbative series is guaranteed by the small parameter α_s. On the contrary, in the region in which the logarithmic terms are large the convergence of the series is spoiled by terms as $\alpha_s^n L^{2n} \sim 1$.

The resummation procedure consists in defining an improved expansion, reorganising the perturbative series according to logarithmic classes (dominant, sub-dominant, etc.) and performing an *all-order summation* of each logarithmic class. This task can be accomplished because in most cases radiative emissions near the edge of phase space can be recursively described and thus treated to all perturbative orders.

For observables that fulfil the exponentiation, this can be achieved by working in a conjugate space, in which the kinematics for multiple soft emission factorise. In this case the Eq. (4.14) can be rewritten as follows

$$R \sim R_0 \exp\left[\sum_{n=1}^{\infty} \alpha_s^n \left(G_{n,n+1} L^{n+1} + G_{n,n} L^n + G_{n,n-1} L^{n-1} \cdots + G_{n,1} L + G_{n,0}\right)\right]. \tag{4.15}$$

In the region where the logarithmic terms dominates (where $\alpha_s L \sim 1$) we can collect terms by classes according to the following rule: $\alpha_s L^2 \sim \alpha_s^2 L^3 \sim \alpha_s^n L^{n+1}$ and $\alpha_s L \sim \alpha_s^2 L^2 \sim \alpha_s^n L^n$ and so on. Thus we rewrite Eq. (4.15):

$$\begin{aligned} R &\sim R_0 \exp\left[\alpha_s L^2\, g_1(\alpha_s L) + \alpha_s L\, g_2(\alpha_s L) + \alpha_s^2 L\, g_3(\alpha_s L) + \dots\right] \\ &= R_0 \exp\left[L\, g_1(\alpha_s L) + \; g_2(\alpha_s L) + \alpha_s\, g_3(\alpha_s L) + \dots\right] \end{aligned} \tag{4.16}$$

where the functions g_i collects the contributions from $G_{n,n+2-i}$ terms, and respectively resum all the corresponding logarithms. We define the logarithm classes according to dominant, next to dominant etc. as follows:

$$\begin{aligned} \alpha_s^n L^{n+1} &\leftrightarrow g_1 \leftrightarrow \text{Leading Logarithms (LL)} \\ \alpha_s^n L^n &\leftrightarrow g_2 \leftrightarrow \text{Next-to-Leading Logarithms (NLL)} \\ \alpha_s^n L^{n-1} &\leftrightarrow g_3 \leftrightarrow \text{Next-to-Next-to-Leading Logarithms (NNLL)} \\ &\dots \end{aligned} \tag{4.17}$$

As we can see from the first line of Eq. (4.16), the advantage of this procedure is evident: in the region where $L \gg 1$ the perturbative series convergence is controlled by powers of the small parameter $1/L$.

4.5 Transverse momentum resummation

The first all-order resummation for the transverse momentum spectrum was performed by summing all double logarithmic terms as $\alpha_s^n L^{2n}$ [99]. Then it was showed that the consistent treatment of the momentum conservation can be implemented in the impact parameter space [100], in which the kinematics of multiple soft emission factorise. Up to now the resummation formalism has been developed for colourless final state systems F such as one or more vector bosons, Higgs bosons and so forth.

In order to obtain a *colourless final state* F, the LO partonic cross section can only be $q\bar{q}$ annihilation or gg fusion, and respectively, the most important examples are the Drell-Yan process and Higgs boson production through gluon fusion. The resummation formalism was originally developed for the case of Drell-Yan by Collins, Soper and Sterman (CSS) [101], and the large logarithmic contributions were resummed at NLL [102] and then at NNLL [103]. The modifications to the formalism necessary to deal with the gluon-gluon initial state have been worked out in Ref. [104]. In the case of Higgs production the cross section was computed at NLL [16] and at NNLL [17, 18].

We start by considering the hard scattering process of two hadrons h_1, h_2 into an observed final state $F(q^2, q_T^2)$ plus a collection of unobserved particles X:

$$h_1(P_1) + h_2(P_2) \to F(q^2, q_T^2) + X, \tag{4.18}$$

where p_1, p_2 are momenta of the colliding hadrons and q^2 is the squared invariant mass of the process. Following Eq. (2.30) we write the differential cross section as (for simplicity we omit to write the explicit dependence on the variables $\mu_R, \mu_F, \alpha_s(q)$)

$$\begin{aligned}\frac{d\sigma_{h_1h_2\to F+x}(P_1,P_2,q^2)}{dq^2dq_T^2} &= \int_0^1 dx_1 \int_0^1 dx_2 \sum_{a,b} f_{a/h_1}(x_1,q)\ f_{b/h_2}(x_2,q) \\ &\quad \cdot \frac{d\hat{\sigma}_{ab\to F+X}(p_1,p_2)}{dq^2dq_T^2}\end{aligned} \tag{4.19}$$

where the index a (b) runs over the partons in the hadron h_1 (h_2) and $p_1 = x_1P_1$ ($p_2 = x_2P_2$). The hard cross section is calculated order by order in α_s according to Eq. (2.18), and its expression is

$$\frac{d\hat{\sigma}_{ab\to F+X}(p_1,p_2)}{dq^2dq_T^2} = \sum_{n=0}^{\infty}\left(\frac{\alpha_s(q)}{\pi}\right)^{n+p} \frac{d\hat{\sigma}^{(n)}_{ab\to F+X}(p_1,p_2)}{dq^2dq_T^2} \tag{4.20}$$

where p is the minimum power of α_s needed for the process to occur at LO ($p = 0$ for Drell-Yan, $p = 2$ for Higgs boson production).

Order by order the divergent terms can be isolated in $d\hat{\sigma}^{(n)}_{ab\to F+X}$ by splitting it into *singular* and *regular* parts: the singular part contains the terms proportional to $\delta(q_T^2)$

and logarithms; the regular part is free of such contributions and is less singular than q_T^{-2} for $q_T \to 0$.

$$\frac{d\hat{\sigma}^{(n)}_{ab\to F+X}}{dq^2 dq_T^2} = T^{(n,\delta)}_{ab}(q, x_1, x_2)\delta(q_T) + \sum_{m=0}^{2n-1} T^{(n.m)}_{ab}(x_1, x_2)\frac{1}{q_T^2}\ln^m\left(\frac{q^2}{q_T^2}\right) \quad (4.21)$$

$$+ \quad R^{(n)}_{ab}(q, q_T, x_1, x_2). \quad (4.22)$$

In other words now we have:

$$\frac{d\hat{\sigma}_{ab\to F+X}}{dq^2 dq_T^2} = \left[\frac{d\hat{\sigma}_{ab\to F+X}}{dq^2 dq_T^2}\right]_{\text{res}} + \left[\frac{d\hat{\sigma}_{ab\to F+X}}{dq^2 dq_T^2}\right]_{\text{fin}} \quad (4.23)$$

where the first term (res) contains all the singular terms that has to be resummed to all orders; the second term (fin) is instead finite (regular) order by order for $q_T \to 0$.

The *finite part* is exactly the difference between the full perturbative result at a given order and its divergent part (its *asymptote*). This term is not significant in the low q_T region and as opposite its importance raises in the intermediate and large q_T region. By definition the finite part of the hadronic cross section is

$$\left[\frac{d\sigma_{ab\to F+X}}{dq^2 dq_T^2}\right]_{\text{fin}} = \sum_{a,b}\int_0^1 dx_1 \int_0^1 dx_2 \; f_a(x_1, q)\; f_b(x_2, q)\left[\sum_{n=0}^{\infty}\left(\frac{\alpha_s(q)}{\pi}\right)^{n+p} R^{(n)}_{ab}(q, q_T, x_1, x_2)\right] \quad (4.24)$$

The *resummed part* embodies the contributions from the divergent terms $T^{(n,\delta)}_{ab}, T^{(n.m)}_{ab}$ and it is calculated (by a Fourier-Bessel transform) in the impact-parameter space[23]:

$$\left[\frac{d\hat{\sigma}_{ab\to F+X}}{dq^2 dq_T^2}\right]_{\text{res}} = \frac{q^2}{\hat{s}}\int \frac{d^2\boldsymbol{b}}{4\pi}\, e^{i\boldsymbol{q}_T\cdot\boldsymbol{b}}\mathcal{W}^F_{ab}(q, \boldsymbol{b}, x_1, x_2) \quad (4.26)$$

where $\boldsymbol{b}$ is the Fourier conjugate variable of $\boldsymbol{q}_T$.The bi-dimensional Fourier-Bessel transform can be simplified in case of un-polarised scattering, where we can use the cylindrical symmetry of collisions:

$$\int \frac{d^2\boldsymbol{b}}{2\pi} e^{i\boldsymbol{q}_T\cdot\boldsymbol{b}}\mathcal{W}^F_{ab}(\boldsymbol{b}) = \int_0^{+\infty} b db \mathcal{W}^F_{ab}(b)\int_0^{2\pi}\frac{d\theta}{2\pi}\, e^{ib\, q_T\, \cos\theta} = \int_0^{+\infty} b db \mathcal{W}^F_{ab}(b)\, J_0(bq_T) \quad (4.27)$$

[2]We recall that $\boldsymbol{q}_T$ and $\boldsymbol{b}$ are bi-dimensional vectors, and $q_T = |\boldsymbol{q}_T|$, $b = |\boldsymbol{b}|$. For the sake of simplicity, we generally omit to use the different notations.

[3]The impact parameter space allows to correctly take into account the kinematical constraint of transverse momentum conservation [100]. In fact, defining $\boldsymbol{q}_T^1 \ldots \boldsymbol{q}_T^n$ as transverse momenta of the emitted soft gluons, the momentum conservation constraint with the $\boldsymbol{q}_T$ of the Higgs is expressed through a Dirac delta function. In the Fourier-Bessel space such delta function factorizes, as follows

$$\delta^2(\boldsymbol{q}_T - \boldsymbol{q}_T^1 \cdots - \boldsymbol{q}_T^n) = \int \frac{d^2\boldsymbol{b}}{2\pi}\, e^{i(\boldsymbol{q}_T - \boldsymbol{q}_T^1 \cdots - \boldsymbol{q}_T^n)\cdot\boldsymbol{b}} = \int \frac{d^2\boldsymbol{b}}{2\pi}\, e^{i\boldsymbol{q}_T\cdot\boldsymbol{b}}\prod_j e^{-i\boldsymbol{q}_T^j\cdot\boldsymbol{b}} \quad (4.25)$$

here we have used the independence of the function $\mathcal{W}_{ab}^F(\boldsymbol{b})$ on the angular variable θ and $J_0(bq_T)$ is the 0th-order Bessel function.

The factor $\mathcal{W}_{ab}^F$ is perturbative, process dependent and embodies the all-order resummation of large logarithms $\ln q^2b^2/b_0^2$ where $b_0 = 2e^{-\gamma_E}$ and $\gamma_E = 0.5772\ldots$ is the Euler number[4]. The resummed component of the hadron cross section is thus

$$\left[\frac{d\sigma_{h_1h_2\to F+X}}{dq^2dq_T^2}\right]_{\rm res} = \sum_{a,b}\int_0^1 dx_1\int_0^1 dx_2\int_0^\infty db\frac{b}{2}J_0(bq_T)f_a(x_1,b_0^2/b^2)f_b(x_2,b_0^2/b^2) \cdot\frac{M_F^2}{s}\,\mathcal{W}_{ab}^F(x_1x_2s,q,b) \tag{4.28}$$

Note that the PDFs now depend on the impact parameter b: we will discuss this important point in the next section. The $\mathcal{W}_{ab}^F$ function is usually written [101] in the following form

$$\mathcal{W}_{ab}^F(x_1x_2s,q,b) = \sum_c\int_0^1 dz_1\int_0^1 dz_2 C_{ca}^F(\alpha_s(b_0^2/b^2),z_1)C_{\bar{c}b}^F(\alpha_s(b_0^2/b^2),z_2)\delta(q^2-z_1z_2s) \cdot\sigma_{c\bar{c}}^{(LO)F}(q^2)S_c^F(q,b) \tag{4.29}$$

where $\sigma_{c\bar{c}}^{(LO)F}$ is the LO total cross section for the partonic process: $c,\bar{c} = q,\bar{q}$ for the Drall-Yan and $c,\bar{c} = g,g$ for the gluon-gluon fusion; the term S_c^F is called quark ($c = q$) or gluon ($c = g$) *Sudakov form factor*.

The main point of resummation is the possibility [99, 100, 101] of expressing the form factor in the following integral form

$$S_c^F(q,b) = \exp\left[-\int_{b_0^2/b^2}^{q^2}\frac{dk^2}{k^2}\left(A_c(\alpha_s(k^2))\ln\frac{q^2}{k^2} + B_c(\alpha_s(k^2))\right)\right]. \tag{4.30}$$

The functions $A_c(\alpha_s), B_c(\alpha_s), C_{ab}(\alpha_s,z)$ do not depend on the large logarithms $\ln(q^2b^2)$ and can be computed by perturbative expansion in powers of α_s:

$$A_c(\alpha_s) = \sum_{n=1}^\infty\left(\frac{\alpha_s}{\pi}\right)^n A_c^{(n)} \quad ; \quad B_c(\alpha_s) = \sum_{n=1}^\infty\left(\frac{\alpha_s}{\pi}\right)^n B_c^{(n)}$$
$$C_{ab}(\alpha_s,z) = \delta_{ab}\delta(1-z) + \sum_{n=1}^\infty\left(\frac{\alpha_s}{\pi}\right)^n C_{ab}^{(n)}(z). \tag{4.31}$$

These coefficients can be obtained by comparing in the small q_T region (at the same order) the perturbative expansion of the resummed expression in Eq. (4.28) with the fixed order calculation of the differential cross section. By the knowledge of the LO differential cross section it is possible to extract the $A^{(1)}$ and $B^{(1)}$ coefficients, analogously with the NLO differential cross section it is possible to extract the $A^{(2)}$ and $B^{(2)}$ coefficients and so on.

[4] b is the Fourier-conjugate variable of q_T, thus $b \sim 1/q_T$ and the limit $q_T \ll q$ corresponds to $b \gg q$.

On the other hand, the resummation at the LL is obtained through the $A^{(1)}$ term, the NLL through $A^{(2)}, B^{(1)}, C^{(1)}$ and in general the resummed calculation at the N^{n}LL order is obtained by the knowledge of $A^{(n+1)}, B^{(n)}, C^{(n)}$ coefficients.

The coefficients $A^{(1)}, A^{(2)}, B^{(1)}, B^{(2)}$ are known both for the gluon [16, 18] and quark [102, 103] cases. Only recently the $A_g^{(3)}, A_q^{(3)}$ coefficients have been computed [21], while in the past they have been assumed [22, 105] equal to the ones that appear in threshold resummation [106, 107, 108]. The general (process independent) form of the coefficients $C^{(1)F}$ is known [19]. In particular the $C_{qg}^{(1)}$ and $C_{gq}^{(1)}$ do not depend on the process, and were first computed in Ref. [103, 17].

4.6 Process-independent transverse momentum resummation

In the previous section we discussed the so called CSS resummation procedure. This formalism has been used to provide a variety of phenomenological applications to vector [109, 110, 111] and Higgs [112, 113] boson production, and also vector boson pair production at hadron colliders [114, 115, 105], and the ensuing calculations have been used quite extensively for physics studies at the Tevatron over many years.

The CSS formalism, however, suffers of some limitations. First of all both the Sudakov form factor and the coefficient functions are not universal, but *process dependent*. In particular (beyond the NLL) the coefficients $B^{(n)}, C^{(n)}$ have to be calculated for each particular process one is interested in. Moreover the PDFs in Eq. (4.28) explicitly depend on the impact parameter b, thus the inversion of the Fourier-Bessel transform involves the extrapolation of the PDFs in the non-perturbative region. Finally the expression in Eq. (4.29) is valid when $qb \gg 1$ and it is used also for small b values (i.e. in the large q_T region), where the resummation is not justified; this implies a poor control of the total cross section when the differential distribution is integrated over q_T. Different strategies have been proposed to settle these difficulties [116], but unfortunately no explicit momentum conservation in the q_T space can be achieved [100].

In the recent years, a process independent resummation formula has been presented [20] and it overcomes the above difficulties. Formula in Eq. (4.29) can be replaced by the following expression

$$\begin{aligned} \mathcal{W}_{ab}^F(x_1x_2s,q,b) &= \sum_c \int_0^1 dz_1 \int_0^1 dz_2 C_{ca}(\alpha_s(b_0^2/b^2),z_1) C_{\bar{c}b}(\alpha_s(b_0^2/b^2),z_2) \delta(q^2 - z_1z_2s) \\ &\quad \cdot \sigma_{c\bar{c}}^F(q^2,\alpha_s(q^2)) S_c(q,b)\,. \end{aligned} \tag{4.32}$$

In this *universal* formula the coefficient function C_{ca} and the Sudakov form factor S_c are process independent and the only formal difference is the replacement of the LO cross

section with the one that includes the higher order corrections:

$$\sigma^F_{c\bar{c}}(q^2, \alpha_s(q^2)) = \sigma^{(LO)F}_{c\bar{c}}(q^2) \cdot H^F_c(\alpha_s(q^2)) \tag{4.33}$$

here the function H^F_c (which depends on the process) adsorbs the process dependent terms in the Sudakov form factor and the coefficient functions; in a symbolic way we can write:

$$\left\{S^F_c, C^F_{ca}, C^F_{\bar{c}b}, \sigma^{(LO)F}_{c\bar{c}}\right\} = \left\{S, C_{ca}, C_{\bar{c}b}, \sigma^F_{c\bar{c}}\right\} \tag{4.34}$$

The function H^F_c does not contain large logarithmic terms, and thus can be expanded in powers of α_s

$$H^F_c(\alpha_s) = 1 + \sum_{n=1}^{\infty} \left(\frac{\alpha_s}{\pi}\right)^n H^{(n)F}_c \tag{4.35}$$

As stated before, the CSS resummation implies a dependence on b in the PDFs, that eventually lead them into the non-perturbative regime. In this universal resummation procedure the original dependence of the PDFs on the factorisation scale μ_F is restored. First we evaluate the PDFs and the coefficient functions at different scales, according with the evolution operator matrix $U_{ab}(z, b_0^2/b^2, \mu_F^2)$ obtained by solving the DGLAP equation (2.40) at the required perturbative accuracy:

$$f_a(x, b_0^2/b^2) = \sum_b \int_x^1 \frac{dz}{z} U_{ab}(z, b_0^2/b^2, \mu_F^2) f_b(x/z, \mu_F^2) \tag{4.36}$$

$$C_{ca}(\alpha_s(b_0^2/b^2), x, \mu_F^2) = \sum_b \int_x^1 \frac{dz}{z} C_{cb}(\alpha_s(b_0^2/b^2), z) U_{ba}(x/z, b_0^2/b^2, \mu_F^2) \tag{4.37}$$

these calculation are made in the Mellin space[5], where the convolutions become ordinary products:

$$\begin{aligned} \frac{dU_{ab,N}(\mu^2, \mu_F^2)}{d\ln\mu^2} &= \sum_c \gamma_{ac,N}(\alpha_s(\mu^2)) U_{cb,N}(\mu^2, \mu_F^2) \\ f_{a,N}(\mu^2) &= \sum_b U_{ab,N}(\mu^2, \mu_F^2) f_{b,N}(\mu_F^2) \\ C_{ca,N}(\mu^2, \mu_F^2) &= \sum_b C_{cb,N}(\mu^2, \mu_F^2) U_{ba,N}(\mu^2, \mu_F^2) \end{aligned} \tag{4.38}$$

[5]From now on, we indicate the Mellin transform of a function by the subscript N, to not be confused with n indicating the n-th term of a generic perturbative expansion.

In this formalism we have

$$\left[\frac{d\sigma^N_{h_1,h_2\to F+X}}{dq^2dq_T^2}\right]_{\rm res} = \sum_{a,b} f_{a,N}(\mu_F^2) f_{b,N}(\mu_F^2) \int_0^\infty db \frac{b}{2} J_0(bq_T)\, \mathcal{W}^F_{ab,N}(b,q,\alpha_s(q^2),\mu_F^2)$$

$$\mathcal{W}^F_{ab,N}(b,q,\alpha_s(q^2),\mu_F^2) = \sum_c \sigma^{(LO)F}_{c\bar{c}}(q^2)\; H^F_c(\alpha_s(q^2))\; S_c(q,b) \tag{4.39}$$

$$\cdot \quad \left(\sum_d C_{cd,N}(\alpha_s(b_0^2/b^2)) U_{da,N}(b_0^2/b^2,\mu_F^2)\right)$$

$$\cdot \quad \left(\sum_e C_{\bar{c}e,N}(\alpha_s(b_0^2/b^2)) U_{eb,N}(b_0^2/b^2,\mu_F^2)\right)$$

in practice the evolution operator U_{ca} "moves" the b-dependent term, from the PDFs to the coefficient functions, thus avoiding the evaluation of the PDFs in the non-perturbative region.

By doing so, the logarithmic terms form the U operators are exponentiated and treated analogously to the ones in the Sudakov form factor Eq. (4.30)

$$\begin{aligned}\mathcal{W}^F_{ab,N}(b,q,\alpha_s(\mu_R^2),\mu_R^2,\mu_F^2) &= \sum_{\{I\}} \mathcal{H}^{\{I\},F}_{ab,N}(q,\alpha_s(\mu_R^2),l_R,l_F,l_Q) \\ &\quad \cdot \exp\left\{\mathcal{G}_{\{I\},N}(b,q,\alpha_s(\mu_R^2),L,l_R,l_Q)\right\}\end{aligned} \tag{4.40}$$

Some comments on the last formula are needed. First of all, the index $\{I\}$ labels a set of flavour indices. Here we will limit ourselves to consider the case of a single species of partons. The general case simply involves a sum over exponential terms, without further conceptual steps (the general case is discussed in appendix A of Ref. [22]). The function $\mathcal{G}_{\{I\},N}$ is universal, it does not depend on the partons a, b and on the factorisation scale μ_F. In this formula we introduce some new variables:

$$l_R = \ln\frac{q^2}{\mu_R^2} \quad ; \quad l_F = \ln\frac{q^2}{\mu_F^2} \quad ; \quad l_Q = \ln\frac{q^2}{Q^2} \tag{4.41}$$

because the dependence on the renormalisation and factorisation scales is always through such logarithms. Finally we introduce a new *resummation scale* Q and its logarithm l_Q: the factorisation between logarithmic and constant terms has some arbitrariness [117] because the argument of the large logarithms can always be rescaled as

$$\ln(q^2b^2) = \ln(Q^2b^2) + \ln\frac{q^2}{Q^2} \tag{4.42}$$

as long as Q is independent of b. If $q \sim Q$ the second term in Eq. (4.42) can be neglected and the large logarithmic terms to be resummed are (slightly) different. The role of this resummation scale is now analogous to the one played by the renormalisation and

factorisation scales: the physical predictions would not depend on these scales if evaluated to all perturbative orders. However this dependence is present when the calculation is truncated to some level of perturbative accuracy. Thus we will set Q at a central value around the physical scale q and then we will estimate the uncertainties by variations of Q around this central value.

The *resummation* function $\exp(\mathcal{G}_N)$ embodies all the large logarithms and the exponent includes the complete dependence on b. It can be systematically expanded as

$$\mathcal{G}_N(L, \alpha_s(\mu_R^2), l_R, l_Q) = Lg^{(1)}(\lambda) + g_N^{(2)}(\lambda, l_R, l_Q) + \frac{\alpha_s}{\pi} g_N^{(3)}(\lambda, l_R, l_Q) + \dots \tag{4.43}$$

where $\lambda = (\beta_0/\pi) L\alpha_s(\mu_R^2)$ and the functions $g^{(n)}(\lambda)$ are defined such that $g^{(n)}(0) \equiv 0$. The $g_N^{(n)}$ functions can be easily calculated for arbitrary values of n [54]. The explicit expression of $g_N^{(1)} = g^{(1)}$ is[6]

$$g^{(1)}(\alpha_s L) = \frac{A^{(1)}}{\beta_0} \frac{\lambda + \ln(1-\lambda)}{\lambda}. \tag{4.44}$$

The function $\mathcal{H}_{ab,N}^F$ takes into account the full information on the hard-scattering process, it is free of large logarithms and can be expanded as powers of α_s (it does not depend on b and hence its evaluation does not require resummation of large logarithms):

$$\mathcal{H}_N(q, \alpha_s, l_R, l_F, l_Q) = \sigma^{(LO),F} \left[1 + \frac{\alpha_s}{\pi} \mathcal{H}_N^{F,(1)}(l_R, l_F, l_Q) + \left(\frac{\alpha_s}{\pi}\right)^2 \mathcal{H}_N^{F,(2)}(l_R, l_F, l_Q) + \dots \right]. \tag{4.45}$$

The first order coefficient $\mathcal{H}_N^{F,(1)}$ has the following expression

$$\mathcal{H}_N^{F,(1)}(l_R, l_F, l_Q) = H^{F(1)} + 2C_N^{(1)} - p\beta_0 l_R + 2\gamma_N^{(1)} l_F - \left(\frac{1}{2} A^{(1)} l_Q + \tilde{B}_N^{(1)} \right) l_Q, \tag{4.46}$$

where p is defined as in Eq. (4.20), $\tilde{B}_N^{(1)} = B_c^{(1)} + 2\gamma_{cc,N}^{(1)}$ with $B_q^{(1)} = B_{\bar{q}}^{(1)} = -3/2C_F$, $C_F = 4/3$ and $B_g^{(1)} = -1/6(11C_A + 2n_f)$. In the case of Higgs boson production ($F = H$) the second order coefficients are reported in Appendix B.

The truncation of the function $\mathcal{W}_{ab,N}^F$ (the resummed part of the differential cross section) at a given logarithmic accuracy is defined as follows: at LL we include the $\left(g^{(1)}, \sigma^{(LO),F}\right)$ contributions, at the NLL we add the contribution of $\left(g_N^{(2)}, \mathcal{H}_N^{F,(1)}\right)$, at the NNLL $\left(g_N^{(3)}, \mathcal{H}_N^{F,(2)}\right)$ and so on.

In order to obtain the *finite part* of the q_T distribution, see Eq. (4.24), we have to eliminate the divergent part in the fixed order calculations. Therefore we neglect any term proportional to $\delta(q_T^2)$ in both fixed order result and in the expansion of the resummed

[6]The explicit expression for the LL, NLL, NNLL functions $g^{(1)}$, $g_N^{(2)}$, $g_N^{(3)}$ can be found in Refs. [22].

result (at the same accuracy). Ad each perturbative order in α_s, the finite part is thus obtained as follows

$$\left[\frac{d\sigma_{a,b\to F+X}}{dq^2 dq_T^2}\right]^{N^n LO}_{\rm fin} = \left[\frac{d\sigma_{a,b\to F+X}}{dq^2 dq_T^2}\right]^{N^n LO}_{\rm fo} - \left[\frac{d\sigma_{a,b\to F+X}}{dq^2 dq_T^2}\right]^{N^n LO}_{\rm res} \tag{4.47}$$

The fixed order terms are obtained by computing the customary perturbative series for the partonic cross section at each perturbative order. The fixed order truncation of the resummed component is obtained by expanding the resummed component at the same order in α_s. In practice, to calculate the fixed order truncation of the resummed component we define the perturbative coefficients $\tilde{\Sigma}^{(n)}$ as follows

$$\begin{aligned}\mathcal{W}^F_{ab,N}(b,q,\alpha_s(\mu_R^2),\mu_R^2,\mu_F^2) &= \sum_c \sigma^{(0)}_{c\bar{c},F}(\alpha_s,M)\Big\{\delta_{ca}\delta_{\bar{c}b}\delta(1-z) \\ &+ \sum_{n=1}^{\infty}\left(\frac{\alpha_s}{\pi}\right)^n\Big[\tilde{\Sigma}^{F(n)}_{c\bar{c}\leftarrow ab}(z,L,l_R,l_F,l_Q) \\ &+ \mathcal{H}^{F,(n)}_{c\bar{c}\leftarrow ab}(z,l_R,l_F,l_Q)\Big]\Big\}.\end{aligned} \tag{4.48}$$

The perturbative coefficient $\tilde{\Sigma}^{(n)}$ are polynomial of degree $2n$ in the variable L. For example, the perturbative expansion of the first order term is

$$\tilde{\Sigma}^{F(1)}_{c\bar{c}\leftarrow ab}(z,L) = \Sigma^{F(1:2)}_{c\bar{c}\leftarrow ab}(z)L^2 + \Sigma^{F(1:1)}_{c\bar{c}\leftarrow ab}(z)L \tag{4.49}$$

where

$$\Sigma^{F(1:2)}_{c\bar{c}\leftarrow ab}(z) = -\frac{1}{2}A^{(1)}_c\delta_{ca}\delta_{\bar{c}b} \tag{4.50}$$

$$\Sigma^{F(1:1)}_{c\bar{c}\leftarrow ab}(z) = -\Big[\delta_{ca}\delta_{\bar{c}b}(B^{(1)}_c + A^{(1)}_c l_Q) + \delta_{ca}\gamma^{(1)}_{\bar{c}b,N} + \delta_{\bar{c}b}\gamma^{(1)}_{ca,N}\Big] \tag{4.51}$$

The expression for the second order coefficient $\tilde{\Sigma}^{(2)}$ can be found in Ref. [22].

4.7 Small and large b region, q_T integrated cross section and non perturbative effects

In order to obtain a more reliable transverse momentum distribution, some refinements are needed.

First, in order to reduce the impact of unjustified resummed logarithms in the large q_T region a procedure (inspired by that introduced in [118]) is used: in the function $\mathcal{G}_N$ we replace the logarithmic variable L with the new one $\tilde{L}$ defined as follows

$$L \equiv \ln\left(\frac{Q^2b^2}{b_0^2}\right) \quad\to\quad \tilde{L} \equiv \ln\left(\frac{Q^2b^2}{b_0^2}+1\right) \tag{4.52}$$

This replacement is fully legitimate, because $\tilde{L} = L + O(1/(Qb)^2)$: in the large b region (small q_T) the effect of the change is negligible, and in the low b region we have[7]

$$\tilde{L} \to 0 \quad \Rightarrow \quad \exp\{\mathcal{G}_N(\alpha_s, \tilde{L})\} \to 1\,. \tag{4.53}$$

With this replacement, using the definition in Eqs. (4.26,4.27,4.40), we obtain the following relation

$$\int_0^\infty dq_T^2 \frac{d\hat{\sigma}_F^{(\mathrm{res})}}{dq_T^2}(q_T, q, \hat{s}, \alpha_s(\mu_R^2), \mu_R^2, \mu_F^2, Q^2) = \frac{q^2}{\hat{s}}\mathcal{H}^F(q, \hat{s}, \alpha_s(\mu_R^2), l_R, l_F, l_Q) \tag{4.54}$$

which can be simply interpreted as a *unitarity constraint* on the resummation procedure: since the hard cross section is evaluated in fixed order perturbation theory, the replacement $L \to \tilde{L}$ puts a constraint on the total cross section. More precisely, the integral over q_T of the q_T spectrum at a given order, exactly reproduces the result of the total cross section at the same perturbative order

$$\int_0^\infty dq_T^2 \frac{d\hat{\sigma}_F^{(NLL+LO)}}{dq_T^2} = \sigma_F^{(NLO)} \tag{4.55}$$

$$\int_0^\infty dq_T^2 \frac{d\hat{\sigma}_F^{(NNLL+NLO)}}{dq_T^2} = \sigma_F^{(NNLO)}\,. \tag{4.56}$$

A *second* problem we have to deal with regards the Landau pole in the evolution of the QCD coupling α_s. The $g^{(n)}(\lambda)$ functions in Eq. (4.43) are singular in the limit $\lambda \to 1$, because the argument of the strong coupling reaches the non-perturbative regime and α_s diverges. Thus the q_T distribution is affected by *non-perturbative effects* (NP) associated with the large b region, and a prescription to avoid this singularity in the integration over b is needed (see Eq. 4.40).

In the original version of the resummation formalism [99, 100], saddle point methods have been used to calculate the Fourier-Bessel transform

$$\begin{aligned} b_{SP} &\simeq \frac{1}{\Lambda_{QCD}}\left(\frac{\Lambda_{QCD}}{q}\right)^p \\ p &= \frac{2A^{(1)}}{2A^{(1)} + \beta_0} \end{aligned} \tag{4.57}$$

where b_{SP} is the saddle point, $p \simeq 0.61$ for gluon and $p \simeq 0.41$ for fermion processes. For a typical hard process with hard scale $q \sim 100$ GeV the value of the saddle point is $b_{SP} \sim 0.1$ GeV^{-1}.

[7]The replacement $L \to \tilde{L}$ is made also in Eq. (4.49), hence by definition the $\tilde{\Sigma}^{(n)}$ polynomials vanish when $\tilde{L} = 0$ (i.e. for $b = 0$).

Nonetheless, in principle the Fourier-Bessel transform from b to q_T space needs the distribution in all b values. In the original CSS formulation a new non-perturbative function F^{NP} multiplying the standard W function was introduced [119, 101]

$$\mathcal{W}_{ab}^{NP}(b) \equiv \mathcal{W}_{ab}(b_*) \cdot F_{ab}^{NP}(b) \tag{4.58}$$

where $b_* = b/\sqrt{1+(b/b_{max})^2}$ and b_{max} is a small distance (typically $b_{max} \sim 0.5$ GeV^{-1}). In this formulation, for small values of b we have $b \simeq b_*$ and $\mathcal{W}_{ab}^{NP}(b) \simeq \mathcal{W}_{ab}(b)$; the advantage is that the function $\mathcal{W}_{ab}(b)$ is always evaluated far from the critical value b_{max}.

In practice, with this procedure the problems in the non perturbative region of $\mathcal{W}_{ab}(b)$ are transferred to the $F_{ab}^{NP}(b)$ function. In the CSS formulation this function can be written as

$$F_{ab}^{NP(\mathrm{CSS})}(b,q,x_1,x_2) = \exp\left[-\ln(q^2 b_{max}^2) g_1(b) - g_a(x_1,b) - g_b(x_2,b)\right] \tag{4.59}$$

The functions g_1, g_a, g_b are non-perturbative, universal and it is supposed they have to be experimentally measured at some energy. Moreover, they are assumed to vanish as $b \to 0$, so as to leave the total cross section unchanged.

The main source of NP effects is the intrinsic q_T of partons. Thus some Gaussian parameterisations have been proposed, see for example [103, 120, 111]. Kulesza and Stirling [121] introduced a purely Gaussian non-perturbative function of the form

$$F_{ab}^{NP(\mathrm{CSS})}(b) = \exp\left(-g b^2\right) \tag{4.60}$$

and the effective parameter g is fitted separately for each process at different values of q^2. This procedure allows to investigate the intrinsic q_T carried by incoming partons.

An alternative approach to avoid the Landau-pole problem is to perform a deformation of the integration contour in the complex b-space [122] in the same way as previously introduced in the threshold resummation [123]. The b-integral can be split in the complex plane, by introducing two auxiliary functions $h_1(b), h_2(b)$ (whose sum is the $J_0(b)$ Bessel function) related to the Hankel functions, defined as follows

$$\begin{aligned} h_1(b) &= -\frac{1}{\pi}\int_{-i\pi}^{-\pi+i\pi} d\theta e^{-i|b|\sin\theta}, \\ h_2(b) &= -\frac{1}{\pi}\int_{\pi+i\pi}^{-i\pi} d\theta e^{-i|b|\sin\theta}, \\ J_0(b) &= \frac{h_1(b)+h_2(b)}{2}. \end{aligned} \tag{4.61}$$

These auxiliary functions can replace the Bessel function in the Mellin transform. Their utility is that they distinguish the positive and negative phases, then the integration

contour can be deformed allowing to treat the b integral as the sum of the two contributions in the upper and lower half-plane. In our calculation we choose the two integration branches as

$$b = (\cos\phi \pm \sin\phi)|b| \tag{4.62}$$

The two integrals are finite, they can be calculated separately and hence the Mellin transform of the function $\mathcal{W}_N^F$ can be obtained. From a numerical point of view, the result turns out to be very mildly dependent on the choice of the parameter ϕ.

4.8 Double differential cross section: q_T resummation and rapidity dependence

The resummation formalism described in the previous section can be extended to include the rapidity dependence.

Thus we are interested in the same scattering process as Eq. (4.18), but now we calculate the double differential cross section in rapidity and transverse momentum [124]

$$\begin{aligned}\frac{d\sigma_{h_1h_2\to F+x}(y,q_T,M_H,s)}{dydq_T^2} &= \int_0^1 dx_1 \int_0^1 dx_1 \sum_{a,b} f_a(x_1,\mu_F^2)\ f_b(x_2,\mu_F^2) \\ &\cdot \frac{d\hat{\sigma}_{ab\to F+X}(\hat{y},q_T,M_H,\hat{s},\alpha_s(\mu_R^2),\mu_R^2,\mu_F^2)}{d\hat{y}dq_T^2}\end{aligned} \tag{4.63}$$

Comparing to the case in which the rapidity is integrated over, the resummation formulae become a bit more involved, but the structure is essentially the same. We first rewrite the partonic cross section as sum of resummed and finite parts

$$\frac{d\hat{\sigma}_{a,b\to F+X}}{d\hat{y}dq_T^2} = \left[\frac{d\hat{\sigma}_{a,b\to F+X}}{d\hat{y}dq_T^2}\right]_{\text{res}} + \left[\frac{d\hat{\sigma}_{a,b\to F+X}}{d\hat{y}dq_T^2}\right]_{\text{fin}} \tag{4.64}$$

The resummed part is calculated in the Fourier-Bessel space according to Eqs. (4.26,4.27). In the present case, it is convenient to consider *double Mellin* (N_1, N_2)-moments [125, 126] with respect to the two variables $z_1 = e^{+\hat{y}}M_H/\sqrt{\hat{s}}$ and $z_2 = e^{-\hat{y}}M_H/\sqrt{\hat{s}}$ at fixed M_H (note that $0 < z_i < 1$).

More generally [127] any function $f(y,z)$ defined on support $|y| < -\ln\sqrt{z}$ and $0 < z < 1$ can be considered as a function of two variables $z_1 = e^{+y}\sqrt{z}$ and $z_2 = e^{-y}\sqrt{z}$. Thus its (N_1, N_2)-moments $f^{(N_1,N_2)}$ can be defined as

$$f^{(N_1,N_2)} \equiv \int_0^1 dz_1 z_1^{N_1-1} \int_0^1 dz_2 z_2^{N_2-1} f(y,z) \tag{4.65}$$

where

$$y = \frac{1}{2}\ln(z_1/z_2) \qquad z = z_1 z_2. \tag{4.66}$$

Furthermore defining $\nu = i(N_2 - N_1)$ and $N = (N_1 + N_2)/2$, the Mellin transform can also be obtained as follows

$$f^{(N_1,N_2)} \equiv \int_0^1 dz z^{N-1} \int_{-\infty}^{+\infty} dy e^{i\nu y} f(y,z) \tag{4.67}$$

We thus introduce double Mellin transform $\mathcal{W}^{(N_1,N_2)}$ as follows:

$$\mathcal{W}_{ab}^{(N_1,N_2)}(b, M_H, \alpha_s) = \int_0^1 dz_1 z_1^{N_1-1} \int_0^1 dz_2 z_2^{N_2-1} \mathcal{W}_{ab}(\hat{y}, b, M_H, \hat{s}, \alpha_s) \tag{4.68}$$

and the convolution structure of the QCD factorisation formula in Mellin space is readily diagonalised by considering (N_1, N_2)-moments:

$$d\sigma^{(N_1,N_2)} = \sum_{a_1,a_2} f_{a_1}^{(N_1+1)} f_{a_2}^{(N_2+1)} d\hat{\sigma}_{a_1,a_2}^{(N_1,N_2)} \tag{4.69}$$

where $f_{a_i}^{(N_i+1)}$ are the Mellin moments of the PDFs.

The perturbative factor $\mathcal{W}_{ab}^{(N_1,N_2)}$ can indeed be organised in a more general exponential form, in close analogy to Eq. (4.40):

$$\mathcal{W}_{ab}^{(N_1,N_2)}(b, M_H, \alpha_s) = \mathcal{H}_{ab}^{(N_1,N_2)}(M_H, \alpha_s) \exp\left\{\mathcal{G}_{ab}^{(N_1,N_2)}(\alpha_s, \tilde{L})\right\} \tag{4.70}$$

The function $\mathcal{H}^{(N_1,N_2)}$ is process dependent and it can be expanded in powers of α_s as generalisation of Eq. (4.45)

$$\mathcal{H}_{ab}^{(N_1,N_2)}(M_H, \alpha_s) = \sigma^{(LO),F}(M_H, \alpha_s) \left[1 + \frac{\alpha_s}{\pi} \mathcal{H}_{ab}^{(N_1,N_2)(1)} + \left(\frac{\alpha_s}{\pi}\right)^2 \mathcal{H}_{ab}^{(N_1,N_2)(2)} + \dots\right] \tag{4.71}$$

and analogously generalising Eq. (4.43) we obtain

$$\mathcal{G}^{(N_1,N_2)}(\tilde{L}, \alpha_s(\mu_R^2)) = \tilde{L} g^{(1)}(\lambda) + g_{(N_1,N_2)}^{(2)}(\lambda) + \frac{\alpha_s}{\pi} g_{(N_1,N_2)}^{(3)}(\lambda) + \dots \tag{4.72}$$

In the case of the q_T cross section integrated over the rapidity

$$\frac{d\sigma}{dq_T} = \int dy \frac{d\sigma}{dy dq_T} \tag{4.73}$$

the double (N_1, N_2)-moments are replaced by the corresponding single-moments (setting $\nu = 0$ in Eq. (4.67) is equivalent to integrate over rapidity): the functions $\mathcal{W}^N, \mathcal{G}^N, \mathcal{H}^N$ are obtained by setting $N_1 = N_2 = N$ in $\mathcal{W}^{(N_1,N_2)}, \mathcal{G}^{(N_1,N_2)}, \mathcal{H}^{(N_1,N_2)}$. Thus *this procedure is a straightforward generalisation of the q_T resummation.*

From a practical point of view, looking at the formulas in Eq. (4.66), we can easily obtain the $\mathcal{G}^{(N_1,N_2)}, \mathcal{H}^{(N_1,N_2)}$ functions from $\mathcal{G}^N, \mathcal{H}^N$:

$$\mathcal{G}^{(N_1,N_2)} = \frac{1}{2}\left(\mathcal{G}^{N_1} + \mathcal{G}^{N_2}\right) \qquad \mathcal{H}^{(N_1,N_2)} = \sqrt{\mathcal{H}^{N_1}\mathcal{H}^{N_2}} \tag{4.74}$$

These equalities are valid in the simplified case where there is a single species of partons; the generalisation to considering more species of partons does not require any further conceptual steps: it just involves algebraic complications related to the treatment of the flavour indices (the multi-flavour case is briefly illustrated in Appendix A of Ref. [124]).

4.9 Decay products: rapidity, transverse momenta and experimental acceptances

As stated at the beginning of this chapter, we cannot directly observe the Higgs boson. Only its decay products can be revealed and measured in the detectors. Moreover the production total cross section is an ideal quantity that cannot be directly measured because detectors have always a finite acceptance. Thus it is important to provide predictions for observables that can be directly measured by the experiments. The standard way to obtain such predictions is to use general purpose Monte Carlo codes that simulate the full event: from the hadron collision, to the hard interaction, to the showering phase [128, 129]. These codes are able to simulate the full complexity of the hadronic final state, including the parton to hadron transition. They typically implement up to NLO fixed order accuracy [130, 131] and simulate the emission of several soft/collinear partons through a branching algorithm, thus obtaining an effective resummation whose accuracy is (almost) NLL.

There are also *parton level* Monte Carlo codes that are optimised for *specific processes* and can reach higher precision. For Higgs boson production through gluon fusion the `HNNLO` code simulates the Higgs boson production process up to NNLO and its decay into electroweak channels [90]. This code is widely used by the experimental collaborations at the LHC and at the Tevatron [52, 132], but it can not provide fully realistic simulations, since the final state includes at most two hard partons.

Although `HNNLO` takes into account higher order corrections up to NNLO, in some cases the predicted distributions suffer of some perturbative instabilities. The main reason is that at the LO the Higgs boson is produced with vanishing q_T, and as a consequence LO kinematic distributions may show a step like behaviour. This is a common feature of perturbative predictions and it is well understood [133]. In fact to any finite order of perturbation theory, QCD observables defined as infrared/collinear safe can still be infinite at accessible points inside phase space. Such singularities arise whenever at a given perturbative order the observable has a non-smooth behaviour at an accessible point (*critical point*). In this case the higher order corrections will suffer of instabilities close to such critical point. These divergences correspond to integrable singularities and they could in principle be removed by non-perturbative smearing effects. However

this would require non-perturbative contributions that are not power suppressed at high energies.

Another solution is to consider the resummation of soft-gluon contributions that is sufficient to smooth the distribution throughout the physical phase space, i.e. infrared finiteness is restored after resummation of divergent terms to all orders. The resulting characteristic structure is named *Sudakov shoulder*.

From the above discussion it is clear that it is important to support the `HNNLO` code by including the effects of q_T resummation. This is the main reason to work on a new program, that we will call `HRes`, that encodes such resummation.

Chapter 5

Resummed q_T spectrum of the Higgs boson: HqT predictions

This thesis is mostly devoted to the Higgs transverse momentum spectrum. As explained in previous chapter, this spectrum cannot be obtained by simply considering fixed order calculations: in order to obtain reliable predictions the transverse-momentum resummation formalism is needed. The calculation up to almost the NNLL+NLO order was implemented in the HqT public code [91].

The transverse-momentum resummation formalism described in the previous chapter and in Refs. [20, 22] is valid for a generic process in which high-mass system of non strongly-interacting particles is produced in hadron-hadron collisions. The method has been also applied to the production of single vector bosons [134], WW [135] and ZZ [136] pairs, slepton pairs [137], and Drell-Yan lepton pairs in polarised collisions [138].

In this chapter we update and extend the phenomenological analysis presented in Ref. [22]. In particular, the exact value of the NNLO hard-collinear coefficients $\mathcal{H}^{H(2)}$ was computed in Ref. [90, 139]: we calculated (and implemented in the HqT code) their Mellin transform. Moreover the recently derived NNLL coefficient $A^{(3)}$ [21] is now encoded in HqT. Another important improvement is the implementation of the resummation scale dependence (see Eq. (4.52)). Now all the scale dependences (i.e. renormalisation, factorisation and resummation scales (4.41)) are taken into account in the code.

Thus the new version of HqT provides the most advanced perturbative information that is available at present: NNLL resummation at small q_T and the fixed-order NLO calculation at large q_T, and allows more reliable studies on the scale uncertainties.

In this chapter we present numerical results for Higgs production at the Tevatron Run II and at the LHC and we perform a detailed study of the perturbative uncertainties. We also consider the normalised q_T spectrum and discuss its theoretical uncertainties.

5.1 Mellin transform of the hard coefficients $\mathcal{H}^{H,(2)}$

The Higgs spectrum is obtained at a given perturbative order by the knowledge of both the form factor $\mathcal{G}_N$ in Eq. (4.43) and the hard function $\mathcal{H}^H_{gg,N}$ in Eq. (4.45). In the first version of the `HqT` code a crude estimate of the coefficient $\mathcal{H}^{H,(2)}_{gg\to ab}(z)$ of Eq. (4.45) was given

$$\mathcal{H}^{H,(2)}_{gg\leftarrow ab}(z) \sim \delta_{ga}\delta_{gb}\delta(1-z)\left[\left(\frac{19}{8}+\frac{2}{3}n_f\right)L_t + c\right] \tag{5.1}$$

where the term proportional to $L_t = \ln\frac{M_H^2}{M_t^2}$ could be obtained from the results of [15,16] and the coefficient c was estimated using the known results on the total NNLO cross section [8,9,10]. This approximation is rather crude since it keeps only the $\delta(1-z)$ contribution in the gg channel and neglects both the other terms and the contributions in the qg and qq' channels. Nonetheless, at the LHC, this approximation works remarkably well in a wide range of Higgs boson masses.

The exact expression of the $\mathcal{H}^{H,(2)}_{gg\leftarrow ab}(z)$ has been published in Ref. [139] and is reported in Appendix B.

The resummation is carried out in the Mellin space and thus the Mellin transform Eq. (2.33) of the hard coefficients[1] $\mathcal{H}^{H,(2)}_{gg\leftarrow gg}(z)$, $\mathcal{H}^{H,(2)}_{gg\leftarrow gq}(z)$, $\mathcal{H}^{H,(2)}_{gg\leftarrow qq}(z)$ has to be evaluated.

The Mellin transform in the complex variable N of quark-quark contribution is easy to calculate

$$\mathcal{H}^{H,(2)}_{gg\leftarrow qq,N} = -\frac{1}{4}\left(C_F^2\left(\frac{-1}{(N+1)^2}+\frac{4(2N-3)}{(N-1)^2}-\frac{8N+4}{N^2}\right)\right); \tag{5.2}$$

instead the quark-gluon and gluon-gluon coefficients contain terms whose Mellin transform is unknown. They are evaluated using the numerical results of Ref. [140]. The strategy is the following: some master functions are approximated by a truncated series expansion whose coefficients are given by the `MINIMAX`-method [141] with an adaptive choice of arguments z; then (by using the properties of the Mellin transform) a more complicate function is reduced to a combination of integrable functions.

For example, suppose to know both the Mellin transforms of a given function $f(z) \in C^\infty[0,1)$ and its derivative $f'(z)$, but the Mellin transform of $f(z)/(z+1)$ is unknown. Using the Mellin properties it is possible to write down the Mellin transform of $f(z)/(z+1)$ as follows

$$\int_0^1 dz z^{N-1}\frac{f(z)}{z+1} = \ln(2)f(1) - \int_0^1 dz z^{N-2}\ln(z+1)\left[(N-1)f(z)+zf'(z)\right]. \tag{5.3}$$

[1] Note the useful relation valid for the quark-(anti)quark channels:

$$\mathcal{H}^{H,(2)}_{gg\leftarrow q\bar{q}}(z) = \mathcal{H}^{H,(2)}_{gg\leftarrow q\bar{q}'}(z) = \mathcal{H}^{H,(2)}_{gg\leftarrow qq}(z) = \mathcal{H}^{H,(2)}_{gg\leftarrow qq'}(z)$$

The logarithm is approximated with the truncated expansion

$$\ln(z+1) \simeq \sum_{k=0}^{K} a_k^{(1)} z^k \tag{5.4}$$

and the coefficients $a_K^{(1)}$ are estimated with the `MINIMAX`-method.

In conclusion the Mellin transform of $f(z)/(z+1)$ can be expressed as follows

$$\int_0^1 dz z^{N-1} \frac{f(z)}{z+1} \simeq \ln(2) f(1) - \sum_{k=0}^{K} a_k^{(1)} \left[\int dz z^{N+k-2} f(z) + \int dz z^{N+k-1} f'(z) \right] \tag{5.5}$$

For example, this is an useful result in order to calculate the Mellin transform of $Li_3(z)/(z+1)$, where $Li_3(z)$ is the usual polylogarithm as Eq. (B.4). In this case, the necessary Mellin transforms are known

$$\begin{aligned} \int_0^1 dz z^{N-1} Li_3(z) &= \frac{6H_N + N(6N\zeta(3) - \pi^2)}{6N^3} \\ \int_0^1 dz z^{N-1} \frac{dLi_3(z)}{dz} &= \frac{(N-1)\pi^2 - 6H_{N-1}}{6(N-1)^2} \end{aligned} \tag{5.6}$$

where $\zeta(3) = 1.20206\ldots$ and H_N is the analytic continuation of the Harmonic numbers. An integral representation is given by Euler:

$$H_N = \int_0^1 \frac{z_N - 1}{z - 1} dz \tag{5.7}$$

and an analytical expression is

$$H_N = \gamma_E + \psi_0(N+1) \tag{5.8}$$

where $\psi_0(n)$ is the *digamma function*.

Finally we obtain our result:

$$\begin{aligned} \int_0^1 dz z^{N-1} \frac{Li_3(z)}{z+1} &\simeq \ln(2)\zeta(3) \\ &- \sum_{k=0}^{K} a_k^{(1)} \left[\frac{N-1}{N+k-1} \zeta(3) + \frac{k}{(N+k-1)^2} \left(\frac{\pi^2}{6} - \frac{H_{N+k-1}}{N+k-1} \right) \right]. \end{aligned} \tag{5.9}$$

With analogous expansions for the unknown integrals, the Mellin transforms of $\mathcal{H}_{gg,N}^H$ and $\mathcal{H}_{gq,N}^H$ are obtained and their relative numerical precision is about 10^{-7}.

5.2 The q_T spectrum of the Higgs boson at the Tevatron and the LHC

In this section we consider the improved predictions for Higgs boson production by gluon fusion at the Tevatron ($\sqrt{s} = 1.96$ TeV) and the LHC ($\sqrt{s} = 7$ TeV and 14 TeV). The presented resummed results are at NNLL+NLO accuracy[2] and they are compared with the NLL+LO results. For the Tevatron we fix $M_H = 165$ GeV; for the LHC at $\sqrt{s} = 7$ TeV and $\sqrt{s} = 14$ TeV we consider $M_H = 165$ GeV and $M_H = 125$ GeV, respectively.

The hadronic q_T cross section at NNLL+NLO (NLL+LO) accuracy is computed by using NNLO (NLO) parton distributions functions (PDFs) with $\alpha_s(\mu_R^2)$ evaluated at 3-loop (2-loop) order. This choice of the order of the parton densities and α_s is fully justified both in the small-q_T region (where the calculation of the partonic cross section includes the complete NNLO (NLO) result and is controlled by NNLL (NLL) resummation) and in the intermediate-q_T region (where the calculation is constrained by the value of the NNLO (NLO) total cross section). Recent sets of parton densities, which are obtained by analyses of various collaborations, are presented in Refs. [143, 50, 144, 145, 146].

Since the main purpose of this (and the next) chapter is the study of the q_T distribution up to the NNLL+NLO, we consider here only the PDFs sets of Refs. [50, 144, 145, 146], which provide NNLO parton densities with $n_f = 5$ (effectively) massless quarks. Moreover, to avoid multiple presentations of similar results, we use the MSTW2008 parton densities unless otherwise stated.

In Fig. 5.1 (left panels) we present the NLL+LO q_T spectrum of a Higgs boson at the Tevatron, and at the LHC with $\sqrt{s} = 7$ TeV and $\sqrt{s} = 14$ TeV. The NLL+LO result (solid lines) at the default scales ($\mu_F = \mu_R = M_H$, $Q = M_H/2$) are compared with the corresponding LO results (dashed lines). The LO finite component of the spectrum (see Eq. (4.23)) is also shown for comparison (dotted lines). We see that the LO result diverges to $+\infty$ as $q_T \to 0$. The resummation of the small-q_T logarithms leads to a well-behaved distribution: it vanishes as $q_T \to 0$, has a kinematical peak, and tends to the corresponding LO result at large values of q_T. The finite component smoothly vanishes as $q_T \to 0$ but gives a sizeable contribution to the NLL+LO result in the low-q_T region.

The results in the right panels of Fig. 5.1 are analogous to those in the left panels although systematically at one order higher. The q_T spectrum at NNLL+NLO accuracy

[2]The calculation is performed strictly in the large-M_t approximation. This is known to be a good approximation for the q_T spectrum, provided that q_T is not too large ($q_T \lesssim M_t$) [142]. For very large transverse momenta the large-M_t approximation is bound to fail, since the QCD radiation accompanying the Higgs boson becomes sensitive to the heavy-quark loop. Considering the normalized q_T spectrum, for $q_T \lesssim M_t$, corrections beyond the large-M_t approximation are expected to be at the few percent level.

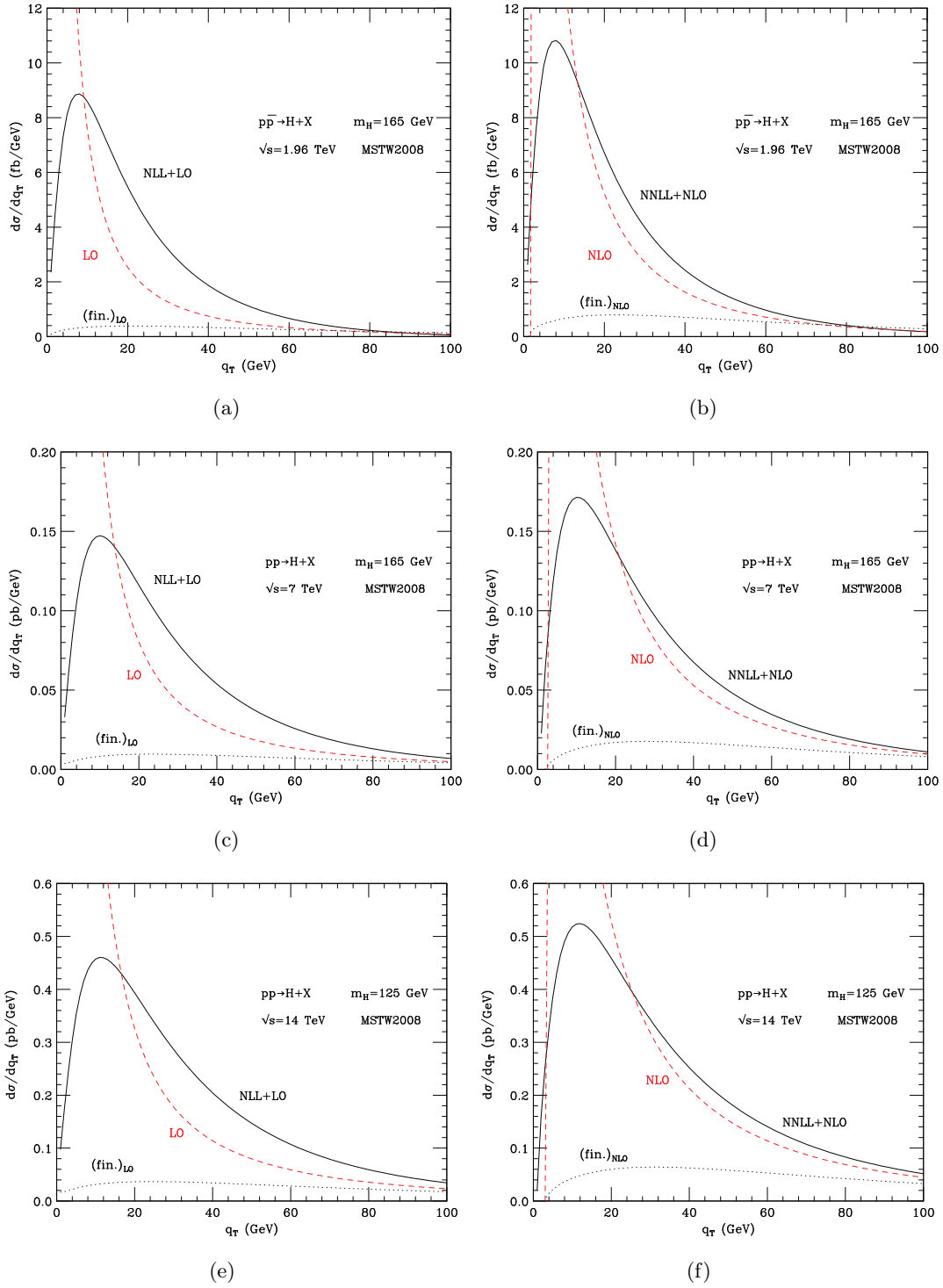

Figure 5.1: *The q_T spectrum of Higgs bosons at the Tevatron and the LHC. Results shown are at NLL+LO (left panels) and NNLL+NLO (right panels) accuracy. Each result is compared to the corresponding fixed-order result (dashed line) and to the finite component (dotted line) in Eq. (4.47).*

(solid line) is compared with the NLO result (dashed line) and with the NLO finite component of the spectrum (dotted line). The NLO result diverges to $-\infty$ as $q_T \to 0$ and, at small values of q_T, it has an unphysical peak (the top of the peak is above the vertical scale of the plot) that is produced by the numerical compensation of negative leading and positive subleading logarithmic contributions. In the region of intermediate values of q_T (say, around 50 GeV), the difference between the NNLL+NLO and NLO results gives a sizeable contribution with respect to the NLO finite component. This difference is produced by the logarithmic terms (at NNLO and beyond NNLO) that are included in the resummed calculation at NNLL accuracy. At large values of q_T the contribution of the NLO finite component noticeably increases. This behaviour indicates that the logarithmic terms are no longer dominant and that the resummed calculation cannot improve upon the predictivity of the fixed-order expansion.

Comparing the left and right panels of Fig. 5.1, we see that the size of the q_T spectrum increases at NNLL+NLO accuracy with respect to the NLL+LO accuracy. The height of the peak at NNLL+NLO is larger than at NLL+LO. The NNLO total cross section, which fixes the value of the q_T integral of our NNLL+NLO result, is larger than the NLO total cross section (by about 30% at the Tevatron and 25% at the LHC). This is due to the positive contribution of both the NNLO terms at small q_T (the $\mathcal{H}_N^{H,(2)}$ coefficient of the the $\mathcal{H}_N^H$ function and the $g_N^{(3)}$ function in the Sudakov form factor) and the NLO finite component at intermediate and large values of q_T.

Comparing Fig. 5.1(a),5.1(b) with Fig. 5.1(c), 5.1(d) and Fig 5.1(e), 5.1(f) we see that the spectrum is harder at the LHC than at the Tevatron. The peak of the NNLL+NLO curve moves from $q_T \sim 8$ GeV at the Tevatron, to $q_T \sim 10$ GeV at the LHC at $\sqrt{s} = 7$ TeV, to $q_T \sim 12$ GeV at the LHC at $\sqrt{s} = 14$ TeV.

The Higgs q_T spectra are obtained with the updated version of the numerical code `HqT`. The quantitative effect of the exact values of $\mathcal{H}^{H,(2)}$ and $A^{(3)}$ at the Tevatron and the LHC is generally small (at the level of about $1-2\%$ at the LHC at 14 TeV, $2-3\%$ at the Tevatron and at the LHC with 7 TeV). The exact values of $\mathcal{H}^{H,(2)}$ and $A^{(3)}$ have the same qualitative impact: they make the q_T-spectrum (slightly) harder.

5.3 Perturbative uncertainties of the Higgs q_T spectrum

As previously stated, another important improvement of the new `HqT` version is the implementation of the resummation scale dependence. In the previous chapters we discussed as the resummed calculation depends on the factorization μ_F, renormalization μ_R scales and on the resummation scale Q. They are useful in order to estimate the uncertainties of the predictions.

5.3.1 Separate contributions of scale uncertainties

The adopted convention to compute factorization and renormalization scale uncertainties is to consider independent variations of μ_R and μ_F by a factor of two around the central value, chosen equal to the Higgs mass ($\mu_R = \mu_F = M_H$). In order to avoid too large logarithmic contributions in the hard coefficients, the independent scale variation is constrained by the request $0.5 \leq \mu_F/\mu_R \leq 2$. For example, the cases ($2\mu_R = 2\mu_F = M_H$) or ($\mu_R/2 = \mu_F/2 = M_H$) are considered, instead ($2\mu_R = \mu_F/2 = M_H$) is excluded. Similarly, (following Ref. [22]) the resummation scale is set to $Q = M_H/2$ as central value, and the resummation scale uncertainty is estimated by considering scale variations in the range $M_H/4 < Q < M_H$.

In Fig. 5.2 we show the scale dependence of the NLL+LO (dashed lines) and NNLL+NLO (solid lines) results. In the left panels we consider variations of the renormalization and factorization scales. The bands are obtained by varying μ_R and μ_F as previously described in this section. We note that, in the region of small and intermediate transverse momenta ($q_T \lesssim 70$ GeV), the NNLL+NLO and NLL+LO bands overlap. This feature, which is not present in the case of the fixed-order perturbative results at LO and NLO, confirms the importance of resummation to achieve a stable perturbative prediction. In the region of small and intermediate values of q_T, we observe a sensible reduction of the scale dependence going from NLL+LO to NNLL+NLO accuracy. At the peak the reduction is from $\pm 20\%$ to $\pm 13\%$ at the Tevatron, and from $\pm 11\%$ to $\pm 8\%$ ($\pm 12\%$ to $\pm 7\%$) at the LHC with $\sqrt{s} = 7$ ($\sqrt{s} = 14$) TeV. Although μ_R and μ_F are varied independently, we find that the dependence on μ_R dominates at any value of q_T.

We point out that the q_T region where resummed perturbative predictions are definitely significant is a wide region from intermediate to relatively-small (say, close to the peak of the distribution) values of q_T. In particular, at very small values of q_T (e.g. $q_T \lesssim 10$ GeV) the size of non-perturbative effects is expected to be important[3], while in the high-q_T region (e.g. $q_T \gtrsim M_H$ GeV) the resummation of the logarithmic terms cannot improve the predictivity of the fixed-order perturbative expansion. The inset plots in the figure show the region from intermediate to large values of q_T. At large q_T, the NLL+LO and NNLL+NLO results deviate from each other, and the deviation increases as q_T increases. As previously stated, this behaviour is not particularly worrying since, in the large-q_T region, the resummed results loose their predictivity and should be replaced by customary fixed-order results.

In the right panels of Fig. 5.2 we consider resummation scale variations. The bands are obtained by fixing $\mu_R = \mu_F = M_H$ and varying Q between $M_H/4$ and M_H. Performing variations of the resummation scale, we can get further insight on the size of yet

[3]See the discussion at the end of this Section.

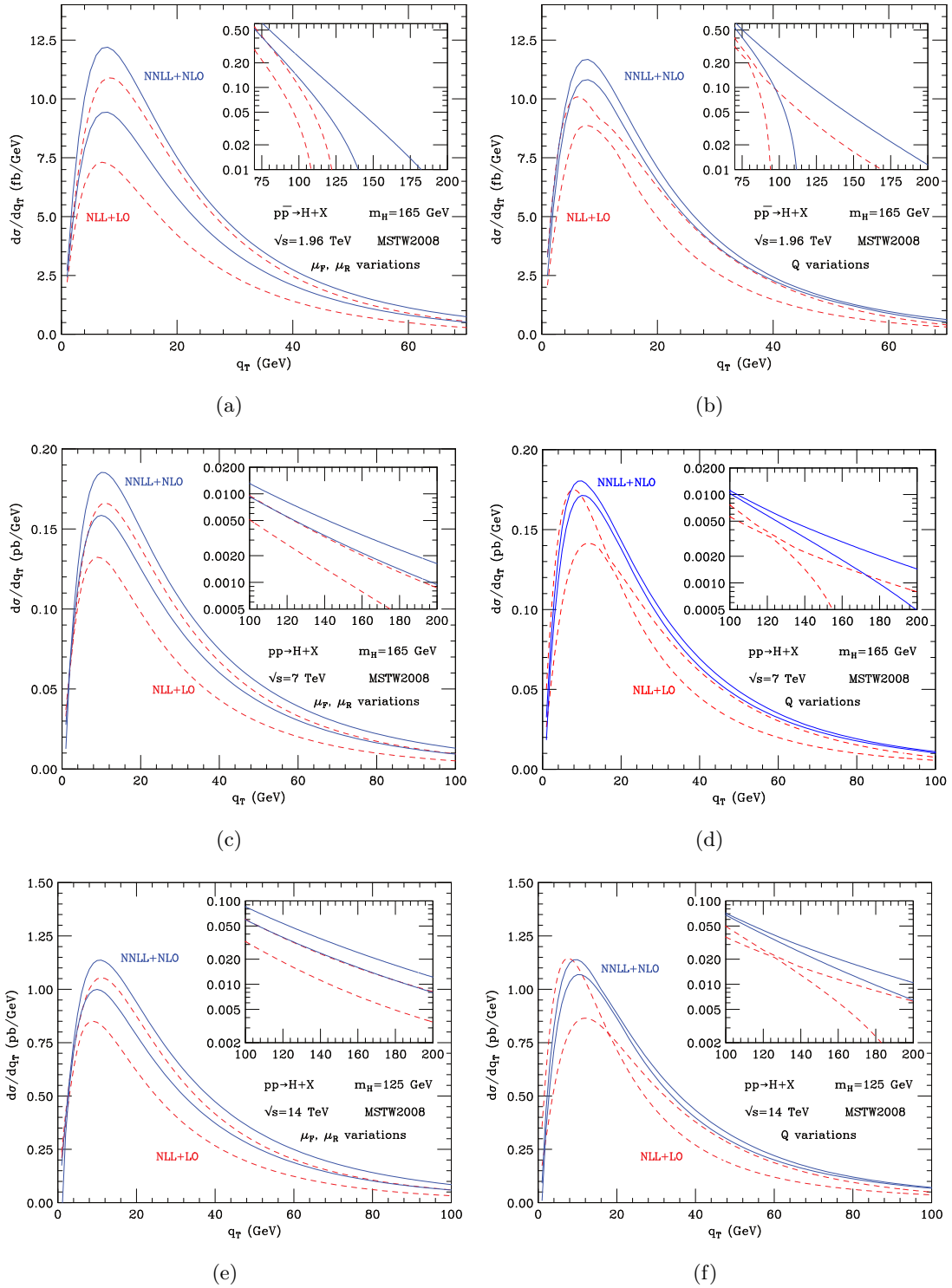

Figure 5.2: *The q_T spectrum of Higgs bosons at the Tevatron and the LHC. The bands are obtained by varying μ_F and μ_R (left panels) and Q (right panels) as described in the text.*

uncalculated higher-order logarithmic contributions at small and intermediate values of q_T. We find that, in the region of the peak, at the Tevatron the scale dependence at NNLL+NLO (NLL+LO) is about $\pm 4\%$ ($\pm 10\%$). At the LHC with $\sqrt{s} = 7$ TeV the scale dependence at NNLL+NLO (NLL+LO) is about $\pm 3\%$ ($\pm 8\%$) and at $\sqrt{s} = 14$ it is about $\pm 3\%$ ($\pm 13\%$).

Comparing the left and right panels of Fig. 5.2, we see that, in the small and intermediate q_T region, at NNLL+NLO accuracy, the factorization and renormalization scale dependence is definitely larger than the resummation scale dependence.

The integral over q_T of the resummed NNLL+NLO (NLL+LO) spectrum is in agreement (for any values of μ_R, μ_F and Q) with the value of the corresponding NNLO (NLO) total cross section to better than 1%, thus checking the numerical accuracy of the code. We also note that the large-q_T region gives a little contribution to the total cross section; therefore, the total cross section constraint mainly acts as a perturbative constraint on the resummed spectrum in the region from intermediate to small values of q_T.

5.3.2 Total perturbative uncertainties of the q_T spectrum

In Fig. 5.3 (left panels) we report the NLL+LO and NNLL+NLO total scale uncertanty bands (again the inset plots show the large-q_T region). The bands represent our best estimate of the perturbative uncertainty, and they are obtained by performing scale variations as follows. We independently vary μ_F, μ_R and Q in the ranges $M_H/2 \leq \{\mu_F, \mu_R\} \leq 2M_H$ and $M_H/4 \leq Q \leq M_H$, with the constraints $0.5 \leq \mu_F/\mu_R \leq 2$ and $0.5 \leq Q/\mu_R \leq 2$. The constraint on the ratio μ_F/μ_R is the same as used in Fig. 5.2; it has the purpose of avoiding large logarithmic contributions (powers of $\ln(\mu_F^2/\mu_R^2)$) that arise from the evolution of the parton densities. Analogously, the constraint on the ratio Q/μ_R avoids large logarithmic contributions (powers of $\ln(Q^2/\mu_R^2)$) in the perturbative expansion of the resummed form factor [4] $\exp\{\mathcal{G}_N\}$ (see Eq. (4.43)). We recall (see e.g. Eq. (19) of Ref. [22]) that the exponent $\mathcal{G}_N$ of the form factor is obtained by q^2 integration of perturbative functions of $\alpha_s(q^2)$ over the range $b_0^2/b^2 \leq q^2 \leq Q^2$. To perform the integration with systematic logarithmic accuracy, the running coupling $\alpha_s(q^2)$ is then expressed in terms of $\alpha_s(\mu_R)$ (and $\ln(q^2/\mu_R^2)$). As a consequence, the renormalization scale μ_R should not be too different from the resummation scale Q, which controls the upper bound of the q^2 integration.

A more effective way to show the perturbative uncertainties is to consider the fractional difference with respect to a 'reference' central prediction. We choose the NNLL+NLO result at central value of the scales as 'reference' result, X_C, and we show the ratio

[4] We do not apply additional constraints on the ratio Q/μ_F, since the form factor does not depend on μ_F.

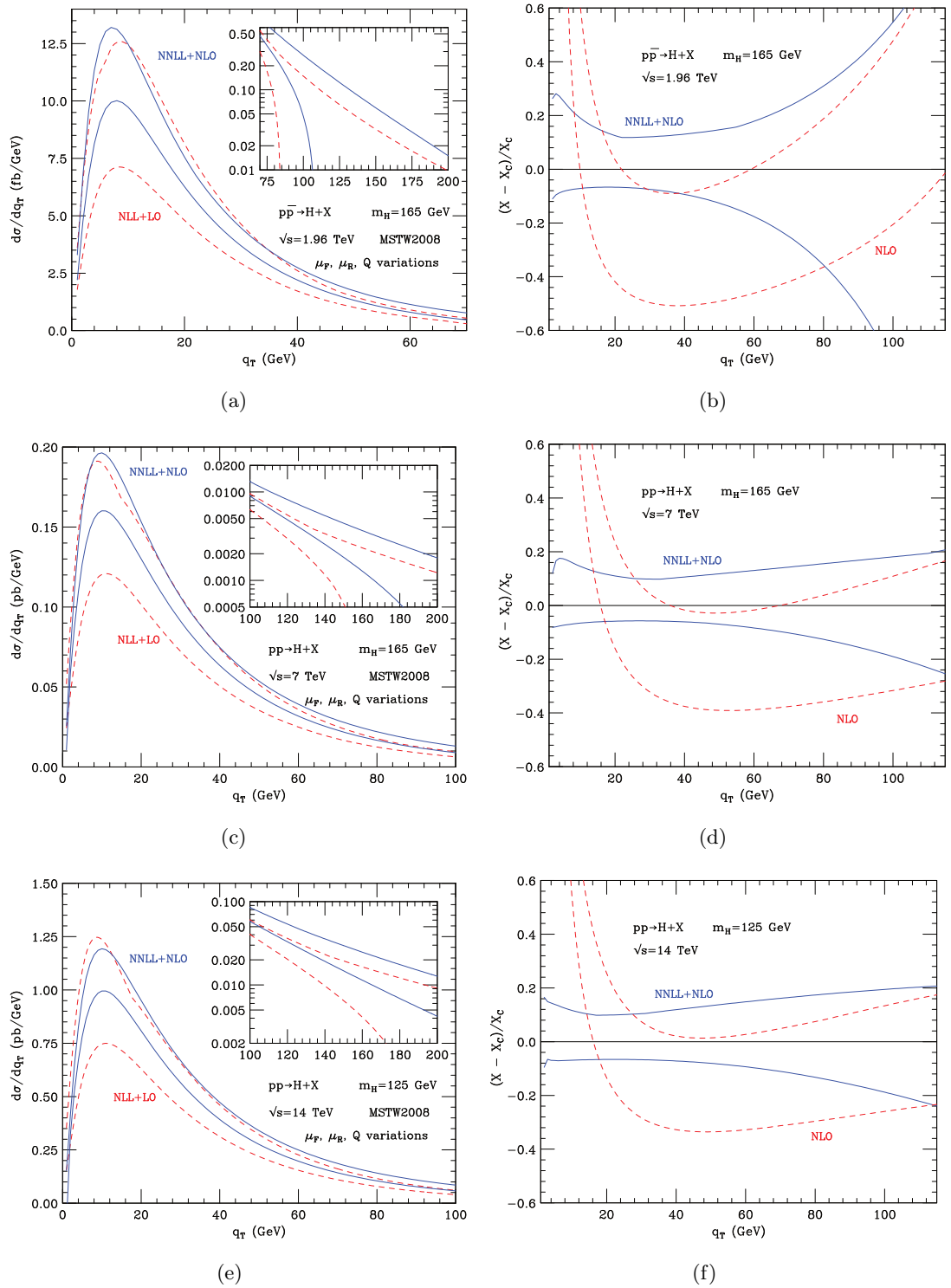

Figure 5.3: *The q_T spectrum of Higgs bosons at the Tevatron and the LHC: NNLL+NLO (solid) and NNL+LO (dashes) uncertainty bands (left panels); NNLL+NLO (solid) and NLO (dashes) uncertainty bands relative to the central NNLL+NLO result (right panels).*

$(X - X_C)/X_C$ in Fig. 5.3 (right panels). The label X refers to the NNLL+NLO results including scale variations (solid lines), and to the NLO results including scale variations (dashed lines).

We comment on the overall perturbative uncertainty band of our results in Fig. 5.3 starting from the Tevatron. The NNLL +NLO (NLL+LO) uncertainty is about $\pm 13\%$ ($\pm 28\%$) at the peak, it decreases to about $\pm 10\%$ ($\pm 23\%$) in the region up to $q_T = 30$ GeV, and becomes $\pm 18\%$ ($\pm 20\%$) at $q_T = 60$ GeV. In the region beyond $q_T \sim 80$ GeV the resummed result looses predictivity, and its perturbative uncertainty becomes large.

In Fig. 5.3(b) the scale variation band of the NLO result is compared to the NNLL+NLO band. The NLO band is obtained by varying μ_F and μ_R as for the NNLL+NLO calculation (the NLO calculation does not depend on the resummation scale Q). We see that at large values of q_T the NLO and NNLL+NLO bands overlap, and the NLO result has smaller uncertainty. As q_T becomes smaller than about 80 GeV, the NNLL+NLO has a smaller uncertainty, and the bands marginally overlap. In this region of transverse momenta, the effect of resummation starts to set in. When q_T becomes smaller and smaller, the NLO band quickly deviates from the NNLL+NLO band and the NLO result becomes unreliable.

We now consider the perturbative uncertainty at the LHC, $\sqrt{s} = 7$ TeV. The NNLL +NLO (NLL+LO) uncertainty is about $\pm 10\%$ ($\pm 22\%$) at the peak, it decreases to about $\pm 8\%$ ($\pm 19\%$) in the region up to $q_T = 30$ GeV, and becomes $\pm 10\%$ ($\pm 18\%$) at $q_T = 60$ GeV. In the region beyond $q_T \sim 120$ GeV the resummed result looses predictivity, and its perturbative uncertainty becomes large. In Fig. 5.3(d) we compare the NLO and NNLL+NLO bands. The qualitative features are similar to Fig. 5.3(b): at large values of q_T the NLO and NNLL+NLO scale uncertainty bands overlap, and the NLO result has smaller uncertainty. As q_T becomes smaller than about 120 GeV, the NNLL+NLO has a smaller uncertainty, but the bands still overlap. In the region of intermediate transverse momenta ($q_T \sim 50$ GeV), the bands marginally overlap and the NLO result underestimates the cross section. When q_T becomes smaller, the NLO band quickly deviates from the NNLL+NLO band and the NLO result becomes unreliable.

We finally consider the perturbative uncertainty at the LHC when $\sqrt{s} = 14$ TeV. The NNLL +NLO (NLL+LO) uncertainty is about $\pm 9\%$ ($\pm 25\%$) at the peak, it decreases to about $\pm 8\%$ ($\pm 19\%$) in the region up to $q_T = 30$ GeV, and moves to $\pm 12\%$ ($\pm 19\%$) at $q_T = 60$ GeV. In the region beyond $q_T \sim 150$ GeV the resummed result looses predictivity, and its perturbative uncertainty becomes large. In Fig. 5.3(f) we compare the NLO and NNLL+NLO scale uncertainty bands. The qualitative features are similar to those of Figs. 5.3(b), 5.3(d): at large values of q_T the NLO and NNLL+NLO bands overlap and the NLO result has smaller uncertainty. In the region of intermediate transverse momenta

($q_T \sim 50$ GeV), the bands marginally overlap and the NLO result underestimates the cross section. When q_T becomes smaller, the NLO result becomes unreliable.

Comparing Fig. 5.3(a),5.3(b) with Fig. 5.3(c),5.3(d) and Fig. 5.3(e),5.3(f) we see that perturbative uncertainties are larger at the Tevatron than at the LHC. We also note that our NNLL+NLO result is much more stable at the LHC than at the Tevatron, where its validity is confined to a smaller region of transverse momenta. This is not completely unexpected. At smaller values of the centre of mass energy, the production of the Higgs boson is accompanied by softer radiation, and thus the q_T spectrum is softer than at the LHC.

5.3.3 Shape uncertainty, Non Perturbative effects and PDFs dependence of the Higgs q_T spectrum

I conclude this section with a discussion on the uncertainties on the normalized q_T spectrum (i.e., $1/\sigma \times d\sigma/dq_T$). The typical procedure of the experimental collaborations is to use the information on the total cross section [52] to rescale the best theoretical predictions of Monte Carlo event generators, whereas the NNLL+NLO result of our calculation, obtained with the public program `HqT`, is used to reweight[5] the transverse-momentum spectrum of the Higgs boson obtained in the simulation. Such a procedure implies that the important information provided by the resummed NNLL+NLO spectrum is not its integral, i.e. the total cross section, but its *shape*. The sources of uncertainties on the shape of the spectrum are essentially the same as for the inclusive cross section: the uncertainty from missing higher-order contributions, estimated through scale variations, and PDF uncertainties.

One additional uncertainty in the q_T spectrum that needs be considered comes from Non-Perturbative (NP) effects. The quantitative predictions presented up to now are obtained in a purely perturbative framework. It is known [147] that the transverse-momentum distribution is affected by NP effects, which become important as q_T becomes small. A customary way of modelling these effects is to introduce an NP transverse-momentum smearing of the distribution. In the case of resummed calculations in impact parameter space, the NP smearing is implemented by multiplying the b-space perturbative form factor by an NP form factor. The parameters controlling this NP form factor are typically obtained through a comparison to data. Since there is no evidence for the Higgs boson yet, the procedure to fix the NP form factor is somewhat arbitrary. Here we follow the procedure adopted in Ref. [22], and the resummed form factor in Eq. (4.43) is multiplied by a gaussian smearing $S_{NP} = \exp\{-gb^2\}$, where the parameter g is taken

[5] A short overview of the reweighting procedure will be given in the next section.

in the range ($g = 1.67 - 5.64$ GeV^2) suggested by the study of Ref. [121][6]. The above procedure can give us some insight on the quantitative impact of these NP effects on the Higgs boson spectrum.

In Fig. 5.4 (left panels) we compare the NNLL+NLO shape uncertainty as coming from scale variations (solid lines) to the NP effects (dashed lines). The bands are obtained by normalizing each spectrum to unity, and computing the relative difference with respect to the central normalized prediction obtained with the MSTW2008 NNLO set (with $g = 0$). A comparison of Fig. 5.4(a),5.4(c),5.4(e) to Fig. 5.3(b),5.3(d),5.3(f) shows that the scale uncertainty on the normalized NNLL+NLO distribution is smaller than the corresponding uncertainty on the NNLL+NLO result. This is not unexpected: a sizeable contribution to the uncertainties shown in Fig. 5.3 comes actually from uncertainties on the total cross section, which do not contribute in Fig. 5.4. In other words, studying uncertainties on the normalized distribution allows us to assess the true uncertainty in the shape of the resummed q_T spectrum.

At the Tevatron (Fig. 5.4(a)) such scale uncertainty ranges from $+8\% - 3\%$ in the region of the peak, to $+3\% - 8\%$ when $q_T \sim 50$ GeV. At larger values of q_T the uncertainty of the NNLL+NLO resummed distribution increases consistently with the behaviour observed in Fig. 5.3(b). The inclusion of the NP effects makes the distribution harder, the effect ranging from 10% to 20% in the very small-q_T region. For $q_T \gtrsim 10$ GeV the impact of NP effects is of the order of about 5% and decreases as q_T increases. At the LHC, $\sqrt{s} = 7$ TeV (Fig. 5.4(c)) the scale uncertainty ranges from $+5\% - 3\%$ in the region of the peak to $+5\% - 4\%$ at $q_T \sim 80$ GeV. At the LHC, $\sqrt{s} = 14$ TeV (Fig. 5.4(e)) the shape uncertainty ranges from $+5\% - 3\%$ in the region of the peak to $+8\% - 9\%$ at $q_T \sim 100$ GeV. The impact of NP effects is similar at $\sqrt{s} = 7$ and 14 TeV: it ranges from about 10% to 20% in the region below the peak, is about $3 - 4\%$ for $q_T \sim 20$ GeV, and quickly decreases as q_T increases. We conclude that the uncertainty from unknown NP effects is smaller than the scale uncertainty, and is comparable to the latter only in the very small q_T region.

The impact of PDF uncertainties at 68% CL on the shape of the q_T spectrum is studied in Figs. 5.4(b),5.4(d),5.4(f). By evaluating PDF uncertainties with MSTW2008 NNLO PDFs (red band in Figs. 5.4(b),5.4(d),5.4(f)) we see that the uncertainty is at the $\pm 1 - 2\%$ level, both at the Tevatron and at the LHC. The use of different PDF sets affects not only the absolute value of the NNLO cross section (see e.g. Ref. [148]) but also the shape of the q_T spectrum. The predictions obtained with NNPDF 2.1 PDFs are in good agreement with those obtained with the MSTW2008 set and the uncertainty

[6]Note that the inclusion of this smearing factor does not change the overall normalization, since $S_{NP}(b = 0) = 1$

bands overlap over a wide range of transverse momenta. On the contrary, the prediction obtained with the ABKM09 NNLO set is softer and the uncertainty band does not overlap with the MSTW2008 band. This behaviour is not completely unexpected: when the Higgs boson is produced at large transverse momenta, larger values of Bjorken x are probed, where the ABKM gluon is smaller than MSTW2008 one. The JR09 band shows a good compatibility with the MSTW2008 result, at least at the Tevatron and at the LHC for $\sqrt{s} = 7$ TeV, where the uncertainty is however rather large. At the LHC for $\sqrt{s} = 14$ TeV the differences with the MSTW2008 result are more pronounced.

5.4 Monte Carlo event generators and QCD corrections: the reweighting technique

In Chapter 3 we discussed the importance of considering higher order QCD corrections, since, in the case of Higgs boson production through gluon fusion, they have a big impact on the production rate. Therefore these corrections should be included in a realistic analysis.

Monte Carlo (MC) event generators (such as for example PYTHIA [128], HERWIG++ [129], ...) often only incorporate LO matrix elements (or NLO for the most important processes). On the other hand fixed order QCD calculations suffer from two shortcomings. First of all parton-showers and hadronization effects can not be directly implemented. Moreover some regions of phase-space (close to kinematic boundaries) would need the resummation of the large logarithmic terms.

Different solutions to these problems are possible: merging cross-sections computed at fixed-order perturbation theory with parton-shower algorithms (POWHEG BOX [130], MC@NLO [131], ...) is possible up to NLO. But there is not a general strategy to incorporate parton shower algorithms in the known NNLO calculations.

An alternative approach is based on the so called *reweighting technique*. The strategy is to multiply LO events obtained with the MC by a probability (so-called K-factor). The K-factors are obtained such that MC events agree with certain observables computed by higher order (fixed-order or resummed) calculations. The simplest reweighting procedure is to choose constant K-factors in order to get the correct inclusive cross sections. A more realistic procedure is to choose K-factors such that MC events match certain well known distributions, e.g. in our case the K-factors can be a function of the transverse momentum of the Higgs boson, such that, after the reweighting procedure, the shape of the q_T spectrum agrees with the one predicted by HqT [149].

The MC reweighting is one of the main utilization of the HqT code. We stress that the reweighting procedure is at best an approximation, since, by definition, after reweighting,

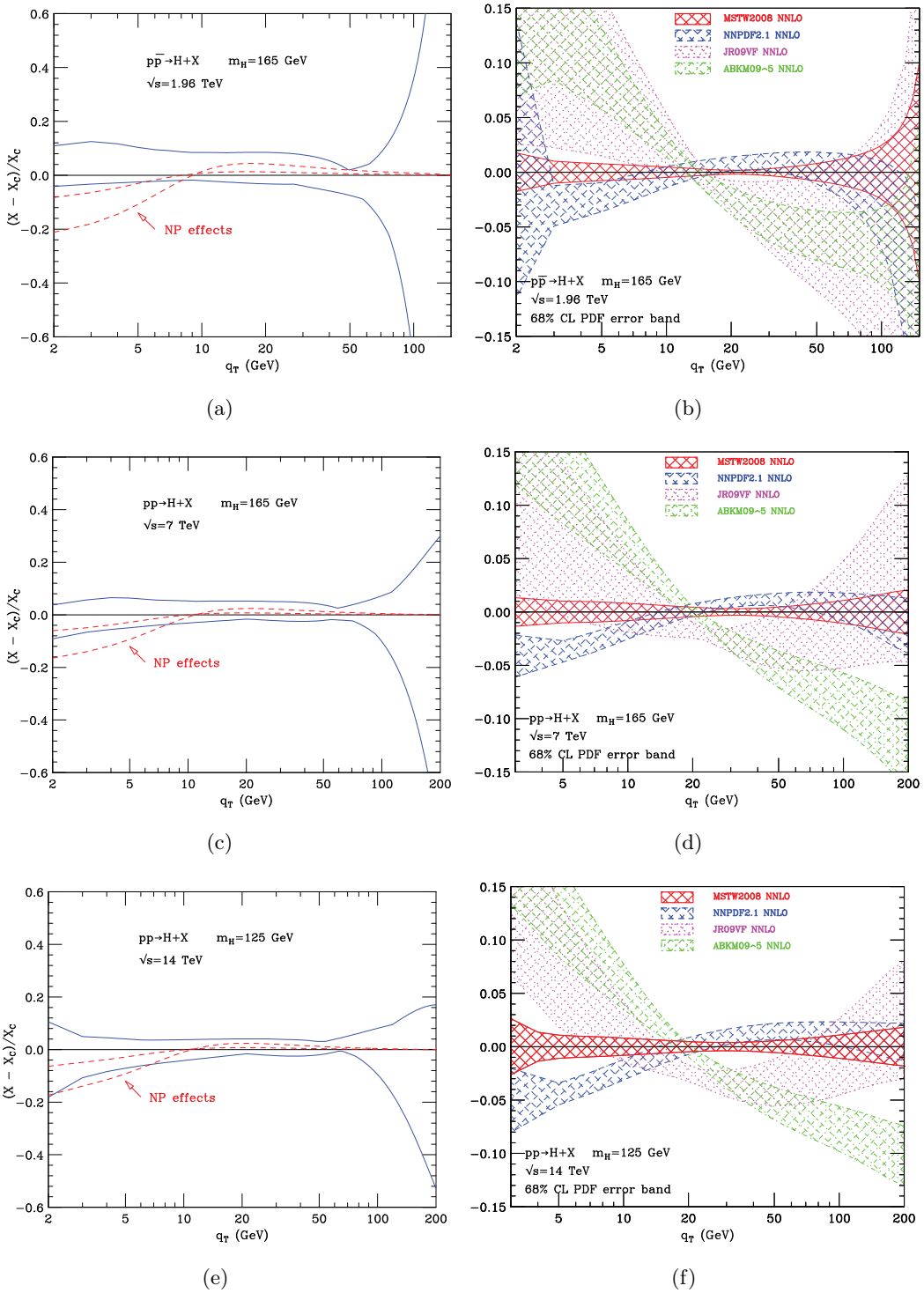

Figure 5.4: *Uncertainties in the normalized q_T spectrum of the Higgs boson at the Tevatron and the LHC. Left panels: the NNLL+NLO uncertainty bands (solid) computed as in Fig. 3 compared to an estimate of NP effects (dashed). Right panels: PDF uncertainties bands at 68% CL. All results are relative to the NNLL+NLO central value computed with MSTW2008 NNLO PDFs.*

only the Higgs q_T spectrum will match the NNLL+NLO calculations. Nevertheless, we believe that, given the simple kinematics of the process and the scalar nature of the Higgs boson, this procedure is in this case well justified.

5.5 Switching in the q_T distribution between resummed and fixed order predictions

In Chapter 4 we studied the perturbative features of the Higgs boson transverse momentum distribution. In particular I stressed the fact that the fixed order predictions are obtained by perturbative expansion and the convergence of such expansion is controlled by the small perturbative parameter α_s. Unfortunately, in the low q_T region, the convergence is spoiled by the presence of large logarithms $L \equiv \log(M_H^2/q_T^2)$. The solution is provided by resummation: a different perturbative expansion is organised and controlled by powers of $1/L$. The obtained resummed predictions are reliable in the small q_T region, but in the high q_T region the resummation procedure in not any more justified, and the quantitative impact of the resummation is still not negligible. This is confirmed by the fact that in the high q_T region the perturbative uncertainties of the resummed results increases, see Figs. 5.4 left panels.

In practice two different calculations are available and they are reliable in two different regions. The best solution is to use resummed predictions in the low and intermediate q_T region where resummation provides an improvement upon fixed order results. On the other hand, fixed order predictions should instead be used in the high q_T region, and one should find a procedure to switch between the two predictions in the intermediate and high q_T region. Unfortunately from a theoretical point of view, there is no particular point where it is clear that one of the two calculations starts to fail and it is better to use the other one.

It the new version of the HqT code we adopt the following solution. There is a point in the intermediate q_T region where the resummed and the fixed order calculations give the same prediction: we call that point *switching point* $q_T^{\rm sw}$. Then the switching procedure is achieved as follows: in the region where q_T is smaller than the switching point $q_T \leq q_T^{\rm sw}$ we use the resummed predictions and in the high q_T region $q_T \geq q_T^{\rm sw}$ we use the fixed order predictions. In Fig. 5.5 we show an example of the switching procedure. The resummed prediction is obtained at the NNLL+NLO precision and the fixed order is at the NLO.

This switching method is a possible solution, that is reasonable, but different procedures or different choices of the switching point $q_T^{\rm sw}$ are possible. For this reason the HqT code provides all the predictions: fixed order, resummed and switched, and the user can

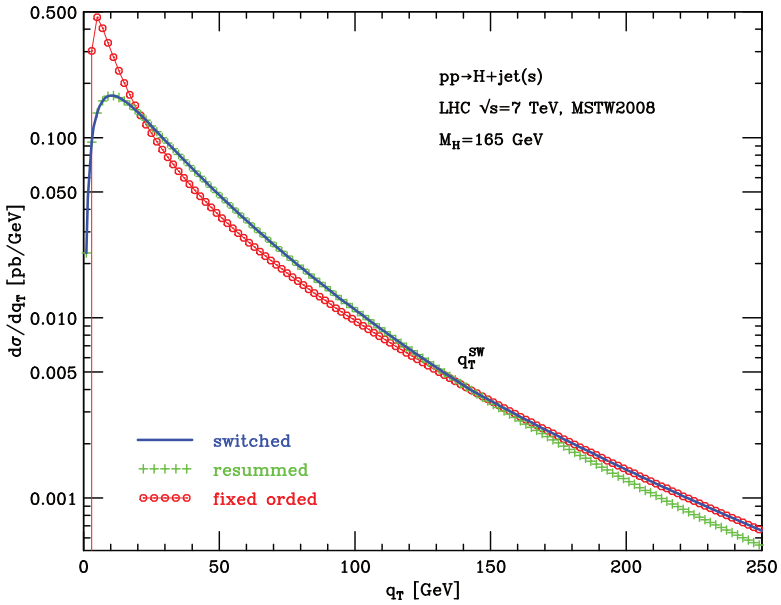

Figure 5.5: The three different predictions for the Higgs boson q_T spectrum at the LHC: in red the fixed order prediction that is reliable in the high q_T region, in green the resummed prediction reliable in the low q_T region and in blue the switched prediction that is reliable in the entire q_T range.

decide which one is more suitable for his/her needs.

A possible draw back of this proposed switching method is that the "switched" prediction is a continuous function, but its derivative has a discontinuity in $q_T^{\rm sw}$. A different switching procedure is to use a smooth interchange between the two results. In practice in the region $q_T^{\rm sw} \pm \Delta q_T$ (around the point $q_T^{\rm sw}$, where Δq_T is of the order of $20 \sim 30$ GeV) we turn off the resummed contribution with a smooth weight function $w(q_T)$, whose value is one in $q_T^{\rm sw} - \Delta q_T$ and zero in $q_T^{\rm sw} + \Delta q_T$ and its derivative is zero in both these points. In the same region, we turn on the fixed order contribution with opposite weight $1 - w(q_T)$. In practice we have

$$\begin{aligned}
[\text{switched}] &= [\text{resummed}] \quad \text{if} \quad q_T < (q_T^{\rm sw} - \Delta q_T) \\
[\text{switched}] &= w(q_T) \cdot [\text{resummed}] + (1 - w(q_T)) \cdot [\text{fix.ord.}] \quad \text{if} \quad q_T \in (q_T^{\rm sw} \pm \Delta q_T) \\
[\text{switched}] &= [\text{fix.ord.}] \quad \text{if} \quad q_T > (q_T^{\rm sw} + \Delta q_T)
\end{aligned} \tag{5.10}$$

and the weight $w(q_T)$ is a smooth function that respects the following conditions

$$\begin{aligned} w(q_T^{\rm sw} - \Delta q_T) &= 1 \\ w(q_T^{\rm sw} + \Delta q_T) &= 0 \\ w'(q_T^{\rm sw} - \Delta q_T) &= 0 \\ w'(q_T^{\rm sw} + \Delta q_T) &= 0 \end{aligned} \tag{5.11}$$

As example the weight function $w(q_T)$ can be represented by a cosine:

$$w(q_T) = \frac{\cos\left(\pi \frac{q_T - (q_T^{\rm sw} - \Delta q_T)}{2\Delta q_T}\right) + 1}{2} \tag{5.12}$$

This switching procedure is implemented in the calculation that I will discuss in the next chapter.

Chapter 6

Higgs boson signals in the electroweak decay channels

In this chapter we extend the results presented in the previous chapter by including the full kinematical information on the Higgs boson and its decay. The inclusive transverse momentum spectrum of the Higgs boson is not directly measurable at the experiments. In fact the Higgs boson is an unstable particle that (after its production) decays into other particles, that we can observe in the detectors. Hence it is important to extend the program `HqT` to include the dependence on the rapidity of the Higgs boson (as discussed in Sec. 4.8), and the most relevant Higgs decay modes. In particular the Electroweak decays are the most useful in the Higgs searches, because they are expected to have the more clear signature in the detectors. The decay calculations are implemented in a code named `HRes` that allows us to retain the full kinematical information of the decay products and also allows to apply arbitrary cuts on the momenta of the final state particles. These cuts are needed in order to correctly take into account the effects of the geometrical acceptances of the detectors. I stress that, with respect to the `HNNLO` Monte Carlo program, `HRes` includes exactly the same perturbative terms up to NNLO, plus the resummation of the logarithmically enhanced terms at small transverse momenta.

To avoid misunderstandings, here I point out the conventional notation concerning the different calculations of the Higgs boson cross section. In case of gluon gluon fusion, the Higgs boson is created through heavy quark loop, then the total cross section at the LO refers to the terms proportional to α_s^2, the NLO to α_s^3 and so on. Instead for the transverse momentum distribution $d\sigma/dq_T$, we need at least one recoiling parton emitted from the initial state gluons. Then the LO (or NLL+LO for resummed calculations) refers to the terms proportional to α_s^3, the NLO (or NNLL+NLO) refers to α_s^4 and so on. Here we are going to study the Higgs decay and we need the double differential

production cross section $\frac{d\sigma}{dq_T dy}$. The Higgs boson can be created with a not null rapidity even without initial state emission. Then it is adopted the same conventional definition as for the total cross section calculation. The summary of the definition for different calculations is shown in Tab.6.1.

	$\sigma_{gg\to H}$	$\frac{d\sigma_{gg\to H}}{dq_T}$	$\frac{d\sigma_{gg\to H}}{dq_T dy}$
α_s^2	LO	-	LO
α_s^3	NLO	LO or NLL+LO	NLO or NLL+NLO
α_s^3	NNLO	NLO or NNLL+NLO	NNLO or NNLL+NNLO
α_s^{n+2}	N^{n}LO	NLO or N^{n}LL+N$^{(n-1)}$LO	NNLO or N^{n}LL+N^{n}LO

Table 6.1: Conventional definitions for the calculation precision, for both fixed order and resummed calculations.

In order to avoid multiple presentation of similar results, here we concentrate on the case of Higgs production at the LHC (e.g. pp collisions at $\sqrt{s} = 7$ TeV). We use MSTW2008 PDFs [50][1], with densities and α_s evaluated at each corresponding order, i.e. we use $(n+1)$-loop α_s at N^{n}LL+N^{n}LO or N^{n}LO (where $n = 1, 2$ for resummed calculations and $n = 0, 1, 2$ for fixed order comparisons). Unless stated otherwise, renormalisation, factorisation and resummation scales are set to their default values $\mu_R = \mu_F = 2Q = M_H$. Finally we remind the reader that the calculation is strictly done in the large-M_t approximation.

The decay matrix elements are implemented at Born level, i.e. radiative corrections are completely neglected. The present version of the program includes the most relevant decay modes of the Higgs boson, namely $H \to \gamma\gamma$, $H \to WW \to l\nu l\nu$ and $H \to ZZ \to 4l$. Unless stated otherwise, the Higgs boson is treated in the narrow-width approximation, but we take into account vector bosons finite width effects of the vector bosons.

In order to study the effects of geometrical acceptance cuts on the predicted distributions, the simulated events are selected by such cuts.

Note that for each simulated event, the momenta of all non strongly interacting particles are known. Hence it is possible to study any observable and study any distribution related to the Higgs boson and its decay products. Here, as examples, we present and discuss only few selected results.

[1] As for the studies with `HqT`, we could use all the recent sets of PDFs [46, 143, 144, 145, 146], which are obtained by analyses of various collaborations, but again in order to avoid multiple presentation of similar results we use only MSTW2008 PDFs.

6.1 $H \to \gamma\gamma$ decay channel

We first consider the Higgs boson with mass $M_H = 125$ GeV, and decay in two photons (the $H \to \gamma\gamma$ channel). Here we show the new resummed results obtained through the `HRes` code, and we compare them with the fixed order predictions obtained by the `HNNLO` code. For each event, we classify the photon transverse momenta according to their minimum and maximum value, q_{Tmin} and q_{Tmax}. We follow studies of Ref. [150, 90, 151] to apply cuts on the photons: the photons are required to be in the central rapidity region $|\eta| < 2.5$, with $q_{Tmin} > 35$ GeV and $q_{Tmax} > 40$ GeV. We can not require the photons to be isolated[2] because we are using resummed predictions that are inclusive on the QCD radiation accompanying the Higgs boson. In other words, the Higgs transverse momentum distribution is obtained by summing the effects of *all* the QCD radiation and we can not predict the energy of each emitted parton. In any case, by studies on fixed order predictions by using the `HNNLO` code, we know that the isolation cut has a small impact on the final distributions.

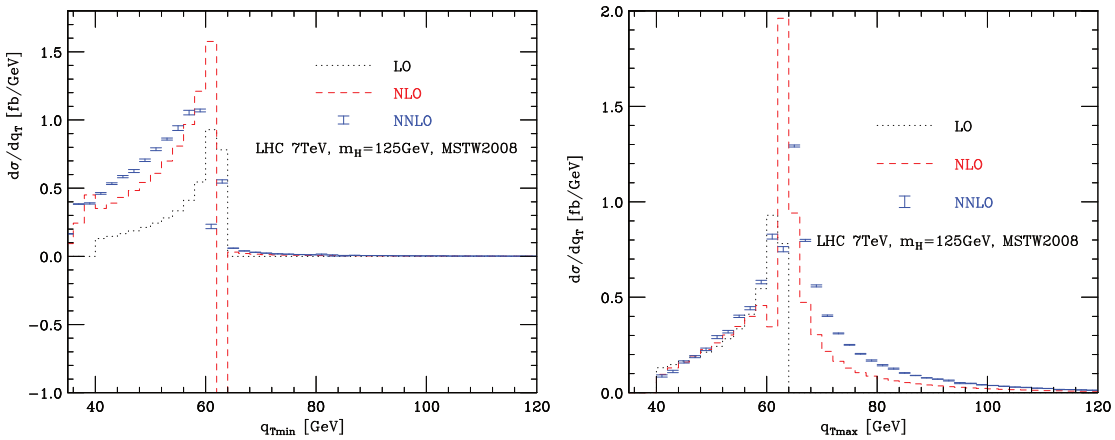

Figure 6.1: Distributions (left) q_{Tmin} and (right) q_{Tmax} for the diphoton signal at the LHC, obtained by fixed order predictions. The cross section is multiplied by the branching ratio in two photons.

In Fig. 6.1 we plot the distributions in q_{Tmin} and q_{Tmax} for the $gg \to H \to \gamma\gamma$ signal, for $M_H = 125$ GeV. These distribution are enhanced when going from LO to NLO to NNLO according to the raise of the total cross section. We note that the shape of these distributions sizeable differs when going from LO to NLO and to NNLO. In particular, at the LO the two photons are emitted with the same q_T because the Higgs boson is produced with zero transverse momentum, hence the LO q_{Tmin} and q_{Tmax} are exactly

[2] A typical isolation requirement is that the hadronic (partonic) transverse energy in a cone of radius $R = 0.3$ along the photon direction has to be smaller than 6 GeV.

identical. Furthermore the LO distribution has a kinematical boundary at $q_T = M_H/2$ (Jacobian peak). Thus higher order predictions suffer of perturbative instabilities, i.e. each higher-order perturbative contribution produces (integrable) logarithmic singularities in the vicinity of that boundary as explained in Sect. 4.9 and Ref. [133].

The same q_{Tmin} and q_{Tmax} predictions are shown in Fig. 6.2; in this case they are obtained through resummed calculations at the NLL+NLO and NNLL+NNLO accurancy respectively. As expected, resummed results do not suffer of instabilities in the vicinity of the LO kinematical boundary; the resummed distributions are smooth and the shape is rather stable when going from NLL+NLO to NNLL+NNLO. Furthermore the fixed order result is recovered out of such instability region.

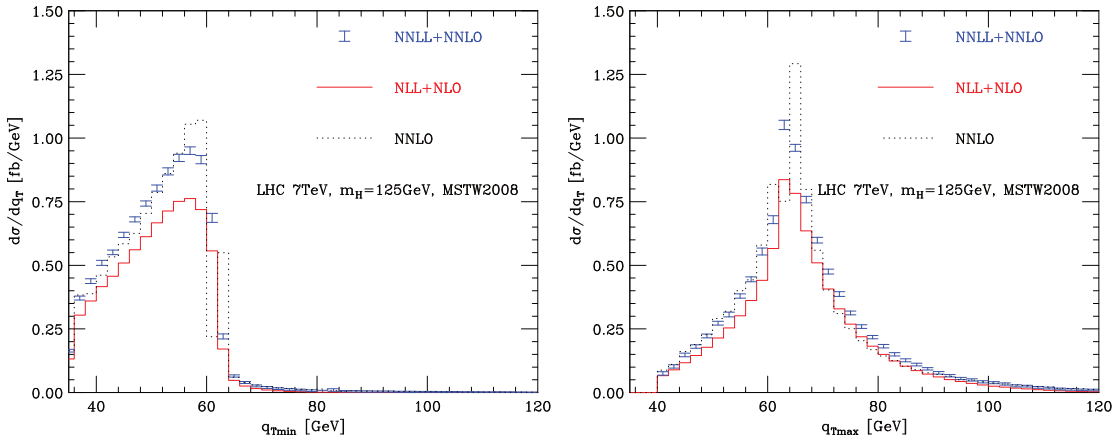

Figure 6.2: Distributions in q_{Tmin} (left) and q_{Tmax} (right) for the $H \to \gamma\gamma$ signal at the LHC, obtained at NLL+NLO and NNLL+NNLO and compared to NNLO.

Similar comments can be applied to the distribution of the average photon momentum $(q_{Tmin} + q_{Tmax})/2$, which is shown in Fig. 6.3 for both fixed order and resummed calculations.

We recall (see Eq. (4.56)) that the resummation does not affect the total cross section for the Higgs boson production. When geometrical cuts are applied on the events, their effects act in slightly different way on fixed order and resummed calculations. In Table 6.2 we compare the total and accepted cross sections, obtained by different calculations, and the effect of geometrical acceptance cuts on photon distributions are summarized. Comparing resummed and fixed order predictions, we see that there are no substantial differences on the accepted cross section.

In addition to the q_{Tmin} and q_{Tmax} distributions, from an experimental point of view, a very useful distribution is the so called $\cos\theta^*$ distribution, where θ^* is the polar angle of one of the photons in the Higgs boson rest frame. More precisely given the 4-momentum

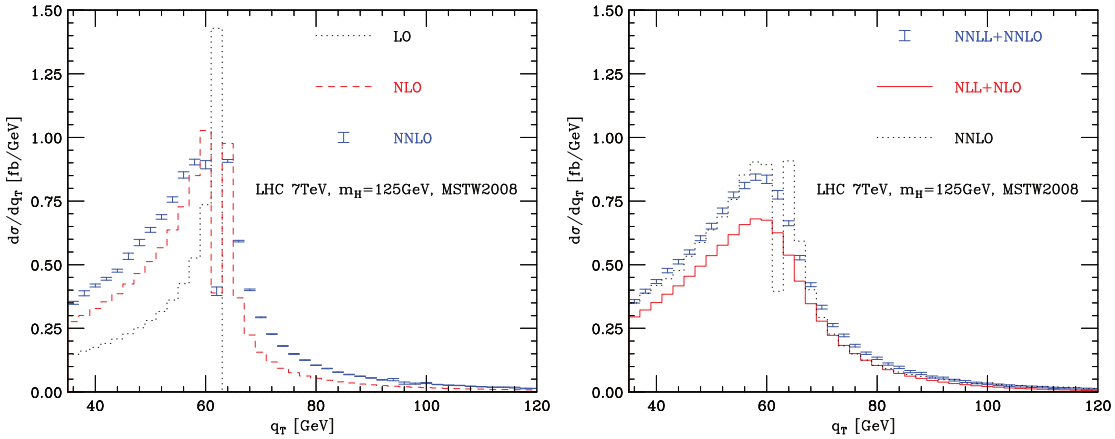

Figure 6.3: Average photon q_T from the $H \to \gamma\gamma$ signal at the LHC, obtained by the fixed order (left) and resummed (right) calculation.

Cross section	LO	NLO	NLL+NLO	NNLO	NNLL+NNLO
Total [fb]	13.1	24.0	24.0	30.3	30.3
With cuts [fb]	8.74	16.0	15.7	19.3	19.4
Efficiency %	66.6	66.6	65.5	63.5	64.1

Table 6.2: $gg \to H \to \gamma\gamma$ cross section before and after geometrical acceptance cuts.

of the photon[3] $q_\gamma = (M_H/2, \boldsymbol{q}_T, q_z)$, the $\cos\theta^*$ angle is defined as follows

$$|\cos\theta^*| = \frac{|q_z|}{M_H/2}; \tag{6.1}$$

considering the on-shell condition for the photon $(\boldsymbol{q}_T)^2 + q_z^2 = (M_H/2)^2$ and that at the LO the q_T of the Higgs boson is zero, we can invert the on-shell condition, obtaining

$$|\cos\theta^*| = \sqrt{1 - \frac{4(\boldsymbol{q}_T)^2}{M_H^2}}. \tag{6.2}$$

A cut on the photon q_T is reflected directly on such $\cos\theta^*$ distribution that is kinematically bounded at $\cos\theta^*_{cut}$. For example for $M_H = 125$ GeV and $q_T \geq 40$ GeV we obtain

$$q_T \geq q_{Tcut} = 40 \text{ GeV} \quad \Rightarrow \quad |\cos\theta^*| \leq |\cos\theta^*_{\text{cut}}| \simeq 0.768. \tag{6.3}$$

At the NLO and NNLO the Higgs transverse momentum is non vanishing and events with $|\cos\theta^*| > |\cos\theta^*_{cut}|$ are kinematically allowed. Around the LO limit $|\cos\theta^*_{cut}|$ higher-order perturbative distributions suffer of logarithmic singularities (as it happen for the

[3] We remind the reader that $\boldsymbol{q}_T$ is a bi-dimensional vector in the xy transverse plane.

photon distributions discussed above). In Fig. 6.4 we report both the distributions (normalized to unity) obtained by fixed order and the resummed calculations. We see that, as in Figs. 6.2,6.3, the resummed distributions are smooth in the region of the kinematical boundary.

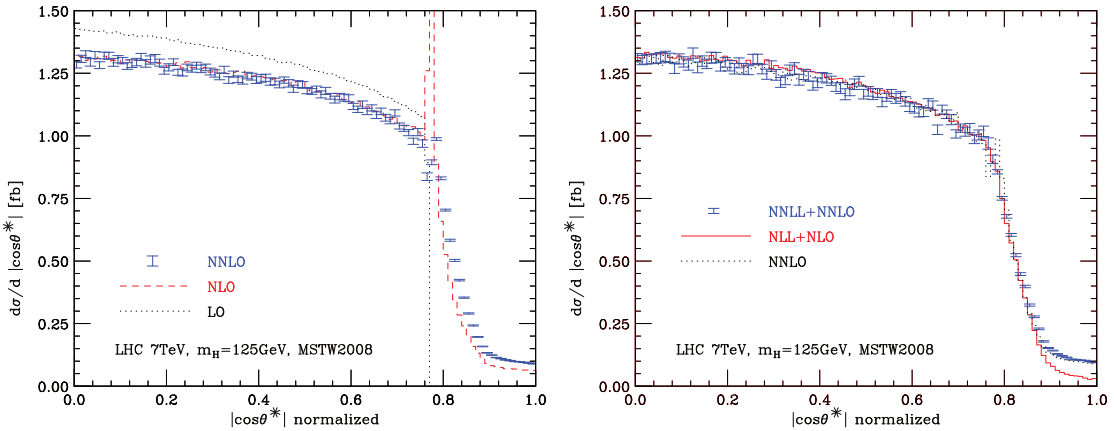

Figure 6.4: Normalised $\cos\theta^*$ distribution at the LHC. On the left: comparison of fixed order calculation that suffers of perturbative instabilities around the LO kinematical cut. On the right: resummed predictions that do not suffer of perturbative instabilities.

6.2 $H \to WW \to l\nu l\nu$ decay channel

In this section we consider the case of Higgs boson with mass $M_H = 165$ GeV. In this mass region the Higgs boson almost decays only into WW pairs (see Fig. 3.11); we consider the two vector bosons decaying leptonically $W \to l\nu$, by assuming only one final state lepton combination.

Note that the measurement of the W mass M_W in the Drell-Yan process is complicated by the fact that an invariant mass can not be reconstructed when there is a neutrino in the final state. M_W can be extracted from the differential cross section $(1/\sigma)d\sigma/dq_T$ where q_T is the transverse momentum of the decay lepton. In an ideal situation, when W is produced at rest, this differential distribution shows a clear (Jacobian) peak at $M_W/2$ and a very sharp drop at larger q_T values. In reality, the situation is complicated by the fact that the W usually has a transverse momentum (caused by QCD radiation) so that the Jacobian peak is badly speared. For this Higgs boson decay channel, two W bosons are produced, thus there are two missing neutrinos plus two measured leptons. In this case measuring the Higgs boson mass it is even more complicated than the measurement of the W boson mass. Thus a good knowledge of the lepton q_T distribution (and other distribution related to the final state leptons) plays a crucial role.

In order to isolate the possible signal some acceptance cuts are needed. Here we apply a set of *preselection* cuts taken from the studies of Refs. [149, 152]:

- the event should contain two opposite charged leptons having p_T larger than 20 GeV and in the central rapidity region $|\eta| < 2$;
- the missing p_T of the event should be larger than 20 GeV;
- the invariant mass of charged leptons should be smaller than 80 GeV;
- the azimuthal separation of the charged leptons in the transverse plane $\Delta\phi$ should be smaller than 135^o.

For each event, we classify the transverse momenta of the charged leptons according to their minimum and maximum value (as we did for the diphoton Higgs boson decay): q_{Tmin} and q_{Tmax} and in Fig. 6.5 we plot the corresponding distributions. The showed results are organised as we did for the diphoton decay: we compare the resummed NLL+NLO and NNLL+NNLO predictions with the corresponding fixed order predictions at the LO, NLO and NNLO accuracy. We see that QCD corrections (taking into account both soft and hard gluon emissions) tend to make the distributions harder. Analogous effects are observed on the transverse momentum spectrum of the W boson reported in Fig. 6.6. In particular, in order to quantitatively estimate the impact of the resummation, each figure is organised in two panels. In the upper panel we show the predictions obtained by different calculations. In the lower panel we plot (in red) the ratio NLL+NLO divided by NLO and (in blue) NNLL+NNLO divided by NNLO predictions. We note that, for both the q_{Tmin} and q_{Tmax} distributions, in the peak region the resummed predictions the ratio is reduced of $\sim 6\%$ for NLL+NLO/NLO and $\sim 2\%$ for NNLL+NNLO/NNLO. In the intermediate region the resummation has an opposite effect. The ratio is enhanced up to $\sim 60\%$ for NLL+NLO/NLO and $\sim 20\%$ for NNLL+NNLO/NNLO. Analogous effects are observed for the W boson p_T distribution.

A very important discriminating variable for the $H \to WW \to l\nu l\nu$ decay channel is the azimuthal separation of the charged leptons in the transverse plane, $\Delta\phi$. As is well known [153], for the Higgs boson signal the leptons tend to be close in angle, thus the bulk of the events is produced at small $\Delta\phi$. Our results for the $\Delta\phi$ distribution are reported in Fig. 6.7. We notice that the steepness of the distributions increases when going from LO to NLO and from NLO to NNLO, and also increases when going from fixed order to resummed predictions, i.e. from NLO to NLL+NLO and from NNLO to NNLL+NNLO. This fact can be interpreted as follows: when the Higgs boson q_T distribution is harder the final state leptons tend to be more boosted in the transverse plane and thus their transverse angular separation becomes smaller. As a consequence the steepness of the

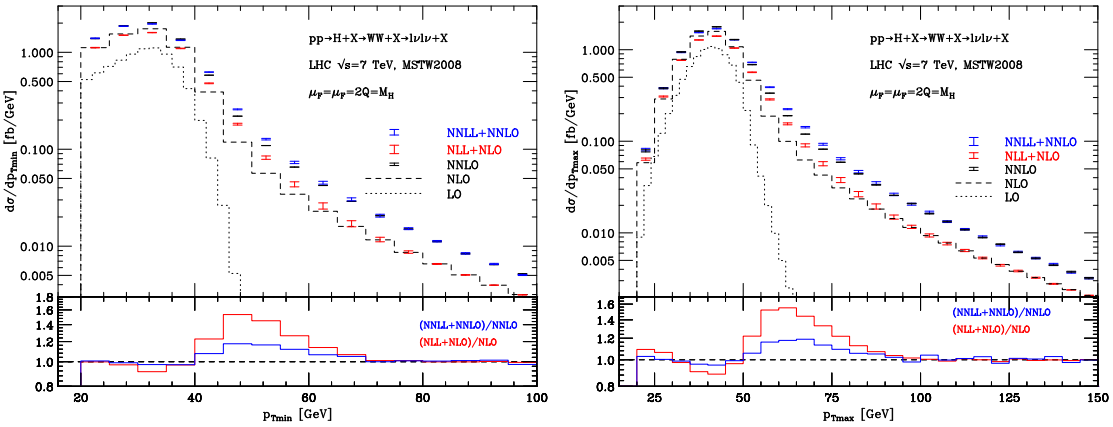

Figure 6.5: Up: transverse momentum spectra of the charged leptons (left p_{Tmin} and right p_{Tmax}) for $pp \to H+X \to WW+X \to l\nu l\nu+X$, where X is initial state QCD radiation. In black fixed order predictions at various perturbative orders, in red resummed result at the NLL+NLO and in blue the NNLL+NNLO. Preselection cuts are applied. Down: ratios of resummed versus fixed order predictions, at the same power of α_s respectively.

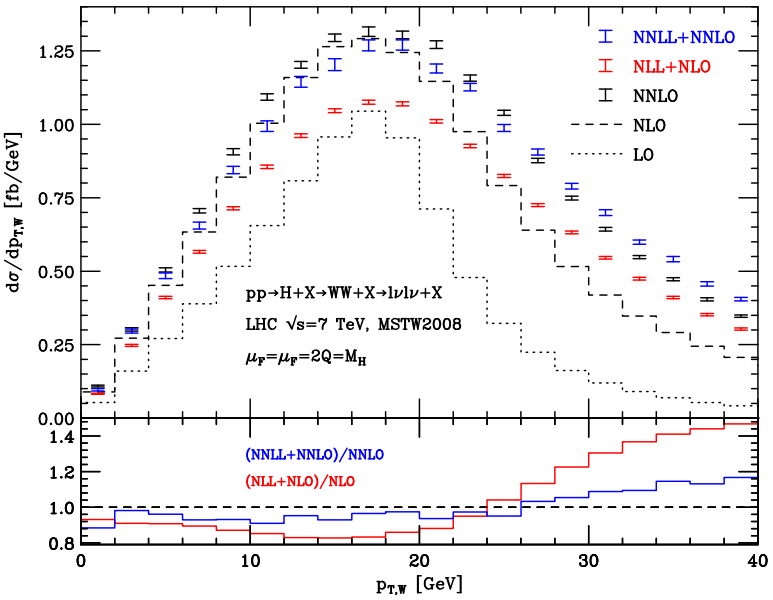

Figure 6.6: Up: transverse momentum spectra of the W boson when preselection cuts are applied. Down: the ratios between resummed and fixed order predictions.

$\Delta\phi$ distribution raises and the efficiency of cuts slightly increases with the calculation accuracy.

We know that the resummation does not affect the total cross section for the Higgs

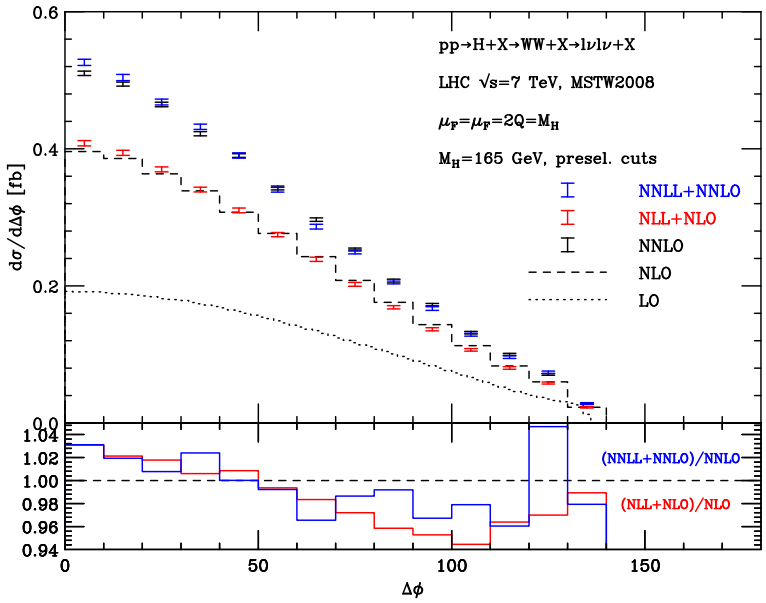

Figure 6.7: Up: the $\Delta\phi$ distribution when preselection cuts are applied. Down: the ratios between resummed and fixed order predictions; they show that the steepness of the distribution is more pronounced for resummed predictions.

boson production. When preselection cuts are applied on the events, as for the diphoton decay, they act in a slightly different way on various predictions obtained by different calculations and in Table 6.3 their effects are summarized. We see that, also in this case the inclusion of resummation does not lead to substantial differences on the accepted cross section.

Cross section	LO	NLO	NLL+NLO	NNLO	NNLL+NNLO
Total [fb]	31.1	58.4	58.4	72.9	72.9
With cuts [fb]	16.5	31.2	31.1	38.9	39.0
Efficiency %	53.0	53.4	53.2	53.4	53.5

Table 6.3: $gg \to H \to WW \to l\nu l\nu$ cross section before and after preselection cuts.

6.3 $H \to ZZ \to 4l$ decay channels

We now consider the production of an Higgs boson with mass $M_H = 200$ GeV. In this mass region the most important decay mode is $H \to ZZ \to 4l$, providing a clean four lepton signature. In particular we will concentrate on the process $pp \to H + X \to$

$ZZ + X \to 4l + X$. The two Z bosons can decay into several combinations of two lepton pairs; here we will concentrate on the $ZZ \to e^+e^-e^+e^-$ decay[4].

The calculation takes into account the appropriate interference contribution. In particular there are only two topologically inequivalent contributions: $H \to Z(k_1 + k_2)Z(k_3 + k_4) \to \big(e^+(k_1)e^-(k_2)\big)\big(e^+(k_3)e^-(k_4)\big)$ (where k_i are the lepton momenta) and $H \to Z(k_1 + k_4)Z(k_3 + k_2) \to \big(e^+(k_1)e^-(k_4)\big)\big(e^+(k_3)e^-(k_2)\big)$. The exchange of one fermion gives a minus sign, hence the two contributions partially cancel each other, but the numerical effect of such interference contribution is smaller than 1% in this mass region. The ensuing inclusive cross section is thus about a factor of two smaller than the cross section in the decay channel $H \to ZZ \to \mu^+\mu^-e^+e^-$.

We consider the following cuts, similar to the ones in Refs. [150, 152]:

- for each event, we order the transverse momenta of the leptons from the largest (p_{T1}) to the smallest (p_{T4}). They are required to fulfil the following thresholds: $p_{T1} > 30$ GeV, $p_{T2} > 25$ GeV, $p_{T3} > 15$ GeV, $p_{T4} > 7$ GeV;
- lepton should be in the central rapidity region $|y| < 2.5$;
- for each possible e^+e^- pair, the closest (m_1) and the next-to-closest (m_2) to M_Z are found; then m_1, m_2 are required to be 81 GeV $< m_1 <$ 101 GeV and 40 GeV $< m_2 <$ 110 GeV.

Note that an isolation cut on the leptons is generally required. For example, a typical cut is: the total energy E_T in a cone of radius 0.2 around each lepton should respect $E_T < 0.05 p_T$. As in the $H \to \gamma\gamma$ decay mode isolation cuts cannot be applied, because in resummed calculation we are inclusive over the QCD radiation accompanying the Higgs boson. By using the fixed order `HNNLO` code we know that the numerical effect of the isolation cuts is almost negligible. As a consequence, we anticipate that, even with the above limitation, our resummed predictions will be useful in the experimental analysis.

In Fig. 6.8 we plot the four p_T spectra of the final state leptons. We know that [152] at LO the p_{T1}, p_{T2} are kinematically bounded by $M_H/2$, whereas $p_{T3} < M_H/3$ and $p_{T4} < M_H/4$. In the vicinity of such boundaries, higher order QCD predictions may develop perturbative instabilities. On the other hand, contrary to what happens in the $H\gamma\gamma$ decay mode, the LO distributions smoothly reach their kinematical boundary and we do not observe perturbative instabilities beyond the LO. As noticed previously in this chapter, the impact of resummation is to make the transverse momentum spectra harder.

The resummation effects are more pronounced in the leading lepton transverse momentum spectrum (see Fig. 6.8(a)) and almost negligible in the softest lepton spectrum (see Fig. 6.8(d)).

[4]The `HRes` and `HNNLO` codes also allows to study the $ZZ \to \mu^+\mu^-e^+e^-$ decay.

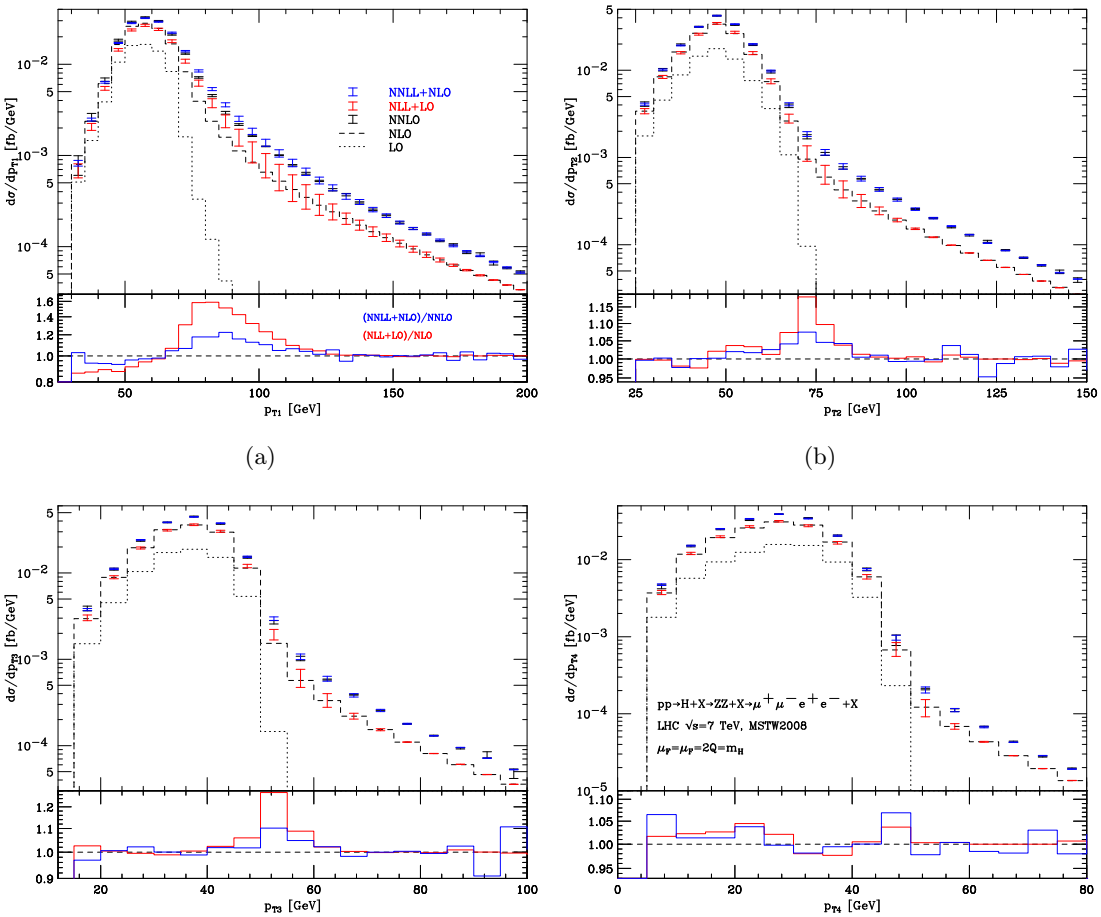

(a) (b)

(c) (d)

Figure 6.8: Up (for each plot): the transverse momentum spectra of the final state leptons for $pp \to H + X \to ZZ + X \to e^+e^-e^+e^- + X$, ordered according to decreasing p_T. They are obtained through fixed order (black) and resummed (red and blue) calculations. Down (for each plot): the ratios between resummed and fixed order predictions.

In Fig. 6.9 we show the p_T distribution of the Z boson. The comments are analogous to those for previous distributions: QCD radiation tend to make the distribution harder.

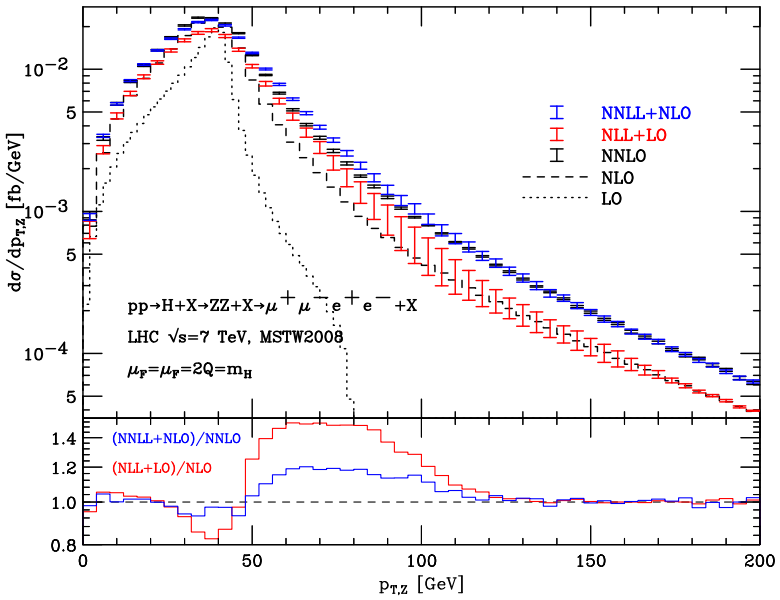

Figure 6.9: Up: the $p_{T,Z}$ distribution when preselection cuts are applied. Down: the ratios between resummed and fixed order predictions.

Finally in Tab. 6.4 we compare the effects of cuts on the inclusive cross sections. The efficiency slightly improves increasing the perturbative accuracy, but no substantial effects from resummation are observed.

Cross section	LO	NLO	NLL+NLO	NNLO	NNLL+NNLO
Total [fb]	0.511	0.976	0.976	1.22	1.22
With cuts [fb]	0.364	0.712	0.711	0.893	0.898
Efficiency %	71.1	72.9	72.8	73.1	73.6

Table 6.4: $gg \to H \to ZZ \to e^+e^-e^+e^-$ cross section before and after geometrical acceptance cuts.

Conclusion

The Standard Model of particle physics describes the known world of subatomic particles at an impressive level of accuracy. Unfortunately, the mechanism that gives masses to the elementary particles remains to be understood. The solution to this problem is based on the Spontaneous Symmetry Breaking mechanism, through which the Lagrangian remains gauge invariant, but the gauge symmetry is broken by the vacuum. Among the several possibilities to realize SSB, the one implemented in the SM requires the existence of a new particle, the so called Higgs boson. The search for the Higgs boson has been under way for decades but we now live in an exciting time for Higgs physics since the LHC experiments will soon tell us whether such a particle really exists or not.

In this thesis I studied the Higgs boson production in hadron collisions through gluon fusion and the most important Higgs decay modes.

In particular, for Higgs boson production, I have focused on the transverse momentum q_T spectrum of Higgs bosons produced in hadron collisions, and I have presented a perturbative QCD study based on transverse-momentum fixed order calculations up to the NLO combined with resummation up to the NNLL accuracy. I followed a resummation formalism that is valid for the production of a generic high-mass system of non strongly-interacting particles in hadron collisions. The formalism combines small-q_T resummation at a given logarithmic accuracy with the fixed-order calculations. It implements a unitarity constraint that guarantees that the integral over q_T of the differential cross section coincides with the total cross section at the corresponding fixed-order accuracy. This leads to QCD predictions with uniform perturbative accuracy over the region from small up to large values of q_T. At large values of q_T, the resummation formalism is superseded by customary fixed-order calculations. I have considered the Higgs boson produced by gluon fusion in $p\bar{p}$ collisions at the Tevatron and pp collisions at the LHC. I have performed a study of the scale dependence of the calculation to estimate the corresponding perturbative uncertainty. In a wide region of transverse momenta the size of the scale uncertainties is considerably reduced in going from NLL+LO to NNLL+NLO accuracy. The calculation of the q_T spectrum is implemented in the updated version of the numerical code `HqT`, that is currently being used by the Tevatron and the LHC collaborations to

correct (reweight) the transverse momentum distribution obtained through Monte Carlo simulations.

Concerning the Higgs boson decay, I have illustrated an explicit application of the resummation formalism up to NNLL+NLO accuracy for the computation of the processes $gg \to H \to \gamma\gamma$, $gg \to H \to WW \to l\nu l\nu$, $gg \to H \to ZZ \to 4l$ at the LHC. I have presented few selected results of kinematical distributions that include the effects of acceptance cuts on the final state particles. These calculations are directly implemented in a new numerical program called `HRes`. I have compared the results obtained with `HRes` with those obtained up to NNLO with the fixed order program `HNNLO`. In the quantitative studies that I have carried out, the two different computations give predictions on the accepted cross section that are in numerical agreement. The program `HRes` includes radiative corrections up to NNLO by supplementing them with soft gluon resummation at small transverse momenta, and we anticipate that it will be extremely useful in the ongoing Higgs search at the LHC. We plan to release a public version of this program in near future.

Appendix A

Acronyms

This is a list of the acronyms used in this thesis.

C.L. = Confidence Level
CME = Centre of Mass Energy
CSS = Collins-Soper-Sterman
DGLAP = Dokshitzer-Gribov-Lipatov-Altarelli-Parisi
EFT = Effective Field Theory
fin = FINite part of fixed order calculations
fo = Fixed Order calculation
IR = Infra Red
LHC = Large Hadron Collider
LL = Leading-Logarithm-accuracy
LO = Leading-Order-accuracy
MC = Monte Carlo
M_H = Higgs boson Mass
M_t = Top quark Mass
$\overline{\text{MS}}$ = modified Minimal Subtraction factorization scheme
NLL = Next-to-Leading-Logarithm-accuracy
NLO = Next-to-Leading-Order-accuracy
NP = Non Perturbative effects
PDFs = Parton Distribution Function(s)
QCD = Quantum ChromoDynamics
QFT = Quantum Field Theory
res = RESummed calculation

SSB = Spontaneous Symmetry Breaking mechanism
SM = Standard Model of elementary particles
UV = Ultra Violet

Appendix B

Hard coefficients $\mathcal{H}_{gg}^{H,(2)}$

$$
\begin{aligned}
\mathcal{H}_{gg\leftarrow gg}^{H(2)}(z) &= \left(\left(-\frac{101}{27}+\frac{7}{2}\,\zeta_3\right)C_A^2+\frac{14}{27}C_A\,n_F\right)\mathcal{D}_0(z) \qquad \text{(B.1)}\\
&+\left(C_A^2\left(\frac{3187}{288}+\frac{7}{8}L_t+\frac{157}{72}\pi^2+\frac{13}{144}\pi^4-\frac{55}{18}\zeta_3\right)+C_A\,C_F\left(-\frac{145}{24}-\frac{11}{8}L_t-\frac{3}{4}\pi^2\right)\right.\\
&\quad+\frac{9}{4}C_F^2-\frac{5}{96}C_A-\frac{1}{12}C_F-C_A\,n_F\left(\frac{287}{144}+\frac{5}{36}\pi^2+\frac{4}{9}\zeta_3\right)\\
&\quad\left.+C_F\,n_F\left(-\frac{41}{24}+\frac{1}{2}L_t+\zeta_3\right)\right)\delta(1-z)\\
&\quad+C_A^2\left(\frac{(1+z+z^2)^2}{z(1+z)}\left(2\mathrm{Li}_3\left(\frac{z}{1+z}\right)-\mathrm{Li}_3(-z)\right)+\frac{2-17z-22z^2-10z^3-12z^4}{2z(1+z)}\zeta_3\right.\\
&\quad-\frac{5-z+5z^2+z^3-5z^4+z^5}{z(1-z)(1+z)}\left(\mathrm{Li}_3(z)-\zeta_3\right)+\mathrm{Li}_2(z)\,\frac{\ln(z)}{1-z}\,\frac{3-z+3z^2+z^3-3z^4+z^5}{z(1+z)}\\
&\quad+\frac{(1+z+z^2)^2}{z(1+z)}\left(\ln(z)\mathrm{Li}_2(-z)-\frac{1}{3}\ln^3(1+z)+\zeta_2\,\ln(1+z)\right)\\
&\quad+\frac{1-z}{3z}(11-z+11z^2)\mathrm{Li}_2(1-z)+\frac{1}{12}z\ln(1-z)-\frac{1}{6}\frac{\ln^3(z)}{1-z}\,\frac{(1+z-z^2)^2}{1+z}\\
&\quad+\ln^2(z)\left(\frac{(1-z+z^2)^2}{2z(1-z)}\ln(1-z)-\frac{(1+z+z^2)^2}{2z(1+z)}\ln(1+z)+\frac{25-11z+44z^2}{24}\right)\\
&\quad+\ln(z)\left(\frac{(1+z+z^2)^2}{z(1+z)}\ln^2(1+z)+\frac{(1-z+z^2)^2}{2z(1-z)}\ln^2(1-z)\right.\\
&\quad\left.\left.-\frac{72+773z+149z^2+536z^3}{72z}\right)+\frac{517}{27}-\frac{449}{27z}-\frac{380z}{27}+\frac{835z^2}{54}\right)\\
&+\quad C_A\,n_F\left(\frac{1+z}{12}\ln^2(z)+\frac{1}{36}(13+10z)\ln(z)-\frac{z}{12}\ln(1-z)-\frac{83}{54}+\frac{121}{108z}+\frac{55}{54}z-\frac{139}{108}z^2\right)\\
&+\quad C_F\,n_F\left(\frac{1+z}{12}\ln^3(z)+\frac{1}{8}(3+z)\ln^2(z)+\frac{3}{2}(1+z)\ln(z)-\frac{1-z}{6z}(1-23z+z^2)\right),
\end{aligned}
$$

$$
\begin{aligned}
\mathcal{H}^{H(2)}_{gg\leftarrow gq}(z) &= C_F^2\Bigg(\frac{1}{48}(2-z)\ln^3 z-\frac{1}{32}(3z+4)\ln^2 z+\frac{5}{16}(z-3)\ln z \\
&\quad+\frac{1}{12}\left(\frac{1}{z}+\frac{z}{2}-1\right)\ln^3(1-z)+\frac{1}{16}\left(z+\frac{6}{z}-6\right)\ln^2(1-z) \\
&\quad+\left(\frac{5z}{8}+\frac{2}{z}-2\right)\ln(1-z)+\frac{5}{8}-\frac{13}{16}z\Bigg) \\
&+ C_F\,n_F\Bigg(\frac{1}{24z}\left(1+(1-z)^2\right)\ln^2(1-z)+\frac{1}{18}\left(z+\frac{5}{z}-5\right)\ln(1-z) \\
&\quad-\frac{14}{27}+\frac{14}{27z}+\frac{13}{108}z\Bigg) \\
&+ C_F C_A\Bigg(-\frac{(1+(1+z)^2)}{2z}\mathrm{Li}_3\left(\frac{1}{1+z}\right)+\left(\frac{1}{2}-\frac{5}{2z}-\frac{5}{4}z\right)\mathrm{Li}_3(z) \\
&- \frac{3}{4z}\left(1+(1+z)^2\right)\mathrm{Li}_3(-z)+\left(2-\frac{11}{6z}-\frac{z}{2}+\frac{z^2}{3}+\left(-\frac{1}{2}+\frac{3}{2z}+\frac{3z}{4}\right)\ln z\right)\mathrm{Li}_2(z) \\
&+ \left(\frac{z}{4}+\frac{(1+(1+z)^2)}{4z}\ln(z)\right)\mathrm{Li}_2(-z) \\
&+ \frac{\left(1+(1+z)^2\right)}{12z}\ln^3(1+z)+\frac{1}{24z}\Big(\left(1+(1+z)^2\right)\left(3\ln^2 z-\pi^2\right)-6z^2\ln z\Big)\ln(1+z) \\
&- \frac{\left(1+(1-z)^2\right)}{24z}\ln^3(1-z)+\frac{1}{48z}\left(6(1+(1-z)^2)\ln z-5z^2-22(1-z)\right)\ln^2(1-z) \\
&+ \frac{1}{72z}\left(-152+152z-43z^2+6(-22+24z-9z^2+4z^3)\ln z+9(1+(1-z)^2)\ln^2 z\right)\ln(1-z) \\
&- \frac{1}{12}\left(1+\frac{z}{2}\right)\ln^3 z+\frac{1}{48}\left(36+9z+8z^2\right)\ln^2 z+\left(-\frac{107}{24}-\frac{1}{z}+\frac{z}{12}-\frac{11}{9}z^2\right)\ln z \\
&+ \frac{1}{z}\left(4\zeta_3-\frac{503}{54}+\frac{11}{36}\pi^2\right)+\frac{1007}{108}-\frac{\pi^2}{3}-\frac{5}{2}\zeta_3+z\left(\frac{\pi^2}{3}+2\zeta_3-\frac{133}{108}\right)+z^2\left(\frac{38}{27}-\frac{\pi^2}{18}\right)\Bigg),
\end{aligned}
\tag{B.2}
$$

$$
\mathcal{H}^{H(2)}_{gg\leftarrow qq}(z) = -C_F^2\left(\frac{2(1-z)}{z}+\frac{(2+z)^2}{4z}\ln z\right), \tag{B.3}
$$

where $L_t=\ln(M_H^2/M_t^2)$ (M_t is the pole mass of the top quark) and $\mathrm{Li}_k(z)$ ($k=2,3$) are the usual polylogarithm functions,

$$
\mathrm{Li}_2(z)=-\int_0^z\frac{dt}{t}\,\ln(1-t)\,,\qquad \mathrm{Li}_3(z)=\int_0^1\frac{dt}{t}\,\ln(t)\,\ln(1-zt)\,. \tag{B.4}
$$

We see that $\mathcal{H}^{H(2)}_{gg\leftarrow gg}(z)$ contains a contribution proportional to $\mathcal{D}_0(z)\equiv\left(\frac{1}{1-z}\right)_+$. This term is of purely soft origin and it can be interpreted as an effect of soft-gluon emission at large angles. This interpretation is supported by the fact that the coefficient of $\mathcal{D}_0(z)$ coincides with the second order coefficient $\tilde{\mathcal{D}}^{(2)}$ that controls soft-gluon emission at large angles near partonic threshold (see eqs.(85) and (37) of ref.[54]).

Bibliography

[1] F. Englert and R. Brout, *Phys. Rev. Lett.*, **13**:321, (1964);
P. W. Higgs, *Phys. Rev. Lett.* **13**:508, (1964);
G. S. Guralnik, C.R. Hagen and T.W.B. Kibble, *Phys. Rev. Lett.*, **13**:585, (1964).

[2] LEP Working Group for Higgs boson searches and ALEPH and DELPHI and L3 and OPAL Collaborations (R. Barate *et al.*), *Phys. Lett.*, **B 565**:61-75, (2003);
`http://lepewwg.web.cern.ch/LEPEWWG/`

[3] Combined CDF and DØ Upper Limits on Standard Model Higgs Boson Production with up to 8.6 fb-1 of Data; e-Print:hep-ex/1107.5518.

[4] ATLAS-CONF-2011-157 CMS PAS HIG-11-023,
`http://cdsweb.cern.ch/record/1399607?ln=en`

[5] CERN Press Relase 25.11,
`http://press.web.cern.ch/press/PressReleases/Releases2011/PR25.11E.html`

[6] H. Georgi, S. Glashow, M. Machacek and P. M. Nanopoulos, *Phys. Rev. Lett.*, **40**:692, (1978).

[7] A. Djouadi, M. Spira and P. M. Zerwas, *Phys. Lett.*, **B 246**:440, (1991).

[8] S. Dawson, *Nucl.Phys.*, **B 359**:283-300, (1991).

[9] M. Spira, A. Djouadi, D. Graudenz and P. M. Zerwas, *Nucl. Phys.*, **B 453**:17, (1995).

[10] M. Kräemer, E. Laenen and M. Spira, *Nucl. Phys.*, **B 511**:523, (1998).

[11] K. G. Chetyrkin, B. A. Kniehl, M. Steinhauser and W. A. Bardeen, *Nucl. Phys.*, **B 535**:3, (1998).

[12] R. Harlander, *Nucl. Phys.*, **B 359**:283, (1991);
R. Harlander and W. Kilgore, *Phys. Rev.*, **D 64**:013015, (2001);
R. Harlander and W. Kilgore, *Phys. Rev. Lett.*, **88**:201801, (2002).

[13] S. Catani, D. De Florian and M. Grazzini, *JHEP*, **0105**:025, (2002).

[14] C. Anastasiou and K. Melnikov, *Nucl. Phys.*, **B 646**:220, (2002).

[15] V. Ravindran, J. Smith and L. van Neerven, *Nucl. Phys.*, **B 665**:325, (2003).

[16] S. Catani, E. D'Emilio and L. Trentadue, *Phys. Lett.*, **B 211**:335, (1988).

[17] R. P. Kauffman, *Phys. Rev.*, **D 45**:1512, (1992).

[18] D. de Florian and M. Grazzini, *Phys. Rev. Lett.*, **85**:4678, (2000).

[19] D. de Florian and .M. Grazzini, *Nucl. Phys.*, **B 616**:247, (2001).

[20] S. Catani, D. de Florian and .M. Grazzini, *Nucl. Phys.*, **B 596**:299, (2001).

[21] T. Becher and M. Neubert, *Eur. Phys. J.*, **C 71**:1665, (2011).

[22] G. Bozzi, S. Catani, D. de Florian and M. Grazzini, *Phys. Lett.*, **B 564**:65, (2003);
G. Bozzi, S. Catani, D. de Florian and M. Grazzini, *Nucl. Phys.*, **B 737**:73, (2006).

[23] D. de Florian, G. Ferrera, M. Grazzini, D. Tommasini, *JHEP*, **1111**:064, (2011), arXiv:hep-ph/1109.2109.

[24] S. Weinberg, *Phys. Rev. Lett.*, **19**:1264, (1967);
S. Weinberg, *Phys. Rev.*, **D5**:1412, (1972).

[25] S. L. Glashow, *Nucl. Phys.*, **22**:597, (1961);
S. L. Glashow, J. Iliopoulos and L. Maiani, *Phys. Rev.*, **D 2**:1285 (1970).

[26] A. Salam, *Originally printed in *Svartholm: Elementary Particle Theory, Proceedings Of The Nobel Symposium Held 1968 At Lerum, Sweden**, Stockholm (1968), 367-377.

[27] D. J. Gross and F. Wilczek, *Phys. Rev.*, **D 8**:3633, (1973)

[28] D. J. Gross and F. Wilczek, *Phys. Rev.*, **D 9**:980, (1974).

[29] H. D. Politzer, *Phys. Rept.*, **14**:129, (1974).

[30] K. Nakamura *et al.* (Particle Data Group), *Journal of Physics*, **G 37**, 075021 (2010 and 2011).

[31] J. Goldstone, *Nuovo Cim.*, **19**:154, (1961);
J. Goldstone, A. Salam ans S. Weinberg, *Phys. Rev.*, **127**:965, (1962).

[32] P. W. Higgs, *Phys. Rev. Lett.*, **12**:132, 91964);
P. W. Higgs, *Phys. Rev. Lett.*, **13**:508, (1964);
P. W. Higgs, *Phys. Rev.*, **145**:1156, (1966).

[33] P. W. Anderson, *Phys. Rev.*, **130**:439, (1963).

[34] K. Hagiwara *et al.*, *Phys. Rev.*, **D 66**:010001, (2002).

[35] NuTeV Collaboration, *Phys. Rev. Lett.*, **88**:091802, (2002); *Erratum-ibid.*, **90**:239902, (2003); e-Print:hep-ex/0110059v3.

[36] D. J. Bjorken and S. D. Drell, *Relativistic Quantum Fields*, (1964).

[37] M. E. Peskin and D. V. Schroeder, *An Introduction to Quantum Field Theory*, (1995).

[38] L.D. Faddeev and V.N. Popov, *Phys. Lett.*, **B 25**:29 (1967).

[39] J. C. Collins, *Renormalization*, (1993).

[40] S. Bethke, *Prog. Part. Nucl. Phys.*, **58**:351-386, (2007).

[41] T. Muta, *Foundations of quantum chromodynamics:an introduction to perturbative methods in gauge theories*, (2010).

[42] R. K. Ellis, W. J. Stirling and B. R. Webber, *QCD and Collider Physics*, Cambridge University Press, (1996).

[43] F. Bloch and A. Nordsieck, *Phys. Rev.*, **52**:54, (1937).

[44] T. Kinoshita, *J. Math. Phys.*, **3**:650, (1962);
T.D. Lee and M. Nauenberg, *Phys. Rev.*, **B 133**:1549, (1964).

[45] G. Sterman, *An introduction to quantum field theory*, Cambridge University Press, (1993).

[46] The PDF4LHC Working Group, *arXiv:hep-ph/1101.0536v1*

[47] D. Amati, R. Petronzio and G. Veneziano, *Nucl. Phys.*, **B 140**:54, (1978), **B146**:29, (1978);
R. K. Ellis, H. Georgi, M. Machacek, H. D. Politzer and G. Ross, *Nucl. Phys.*, **B 152**:285, (1979).

[48] V. N. Gribov and L. N. Lipatov., *Sov.J.Nucl.Phys.*, **15**:438, (1972);
G. Altarelli and G. Parisi, *Nucl. Phys.*, **B 126**:298, (1977);
Yu. L. Dokshitzer., *Sov.Phys. JETP*, **46**:641, (1977).

[49] H. Georgi and H. D. Politzer, *Phys. Rev.*, **D 9**:416, (1974).

[50] A.D. Martin, W.J. Stirling, R.S. Thorne and G. Watt, *Eur.Phys.J.*, **C 63**:189-285, (2009).

[51] A. Djouadi, J. Kalinowski, and M. Spira, *Comput. Phys. Commun.*, **108**:56-74, (1998);
M. Spira, *Fortschr. Phys.*, **46**:203-284, (1998); A. Djouadi, J. Kalinowski, M. Mühlleitner, and M. Spira, *arXiv:hep-ph/1003.1643*;
http://people.web.psi.ch/spira/hdecay/

[52] LHC Higgs Cross Sections Working Group, *arXiv:hep-ph/1101.0593v3.*

[53] S. Catani, D. De Florian and M. Grazzini, *JHEP*, **0201**:015, (2002).

[54] S. Catani, D. De Florian, M. Grazzini and P. Nason *JHEP*, **0307**:028, (2003).

[55] C. Anastasiou, R. Boughezal and F. Petriello, *JHEP*, **04**:003, (2009).

[56] C. Anastasiou, S. Buehler, F. Herzog, A. Lazopoulos, *arXiv:hep-ph/1107.0683v2.*

[57] M. Grazzini, talk at "*Inauguration Workshop of the LHC Higgs Cross Section Working Group*" April 12-13, 2010, Freiburg;
`http://indico.cern.ch/conferenceOtherViews.py?view=standard&confId=86819`

[58] R. N. Cahn and S. Dawson, *Phys. Rev.*, **B 136**:196, (1984).

[59] T. Han and S. Willanbrock, *Phys. Lett.*, **B 273**:167, (1991).

[60] M. Ciccolini, A. Denner and S. Dittmaier, *Phys. Rev. Lett.*, **99** 161803 (2007);
M. Ciccolini, A. Denner and S. Dittmaier, *Phys. Rev.*, **D 77** 013002, (2008).

[61] T. Figy, C. Oleari, and D. Zeppenfeld, *Phys. Rev.*, **D 68**:073005, (2003);
T. Figy and D. Zeppenfeld, *Phys. Lett.*, **B 591**:297-303, (2004).

[62] P. Bolzoni, F. Maltoni, S. O. Moch and M. Zaro, *Phys. Rev. Lett.*, **105** 011801, (2010).

[63] S. Glashow, D. V. Nanopoulos, and A. Yildiz, *Phys. Rev.*, **D18**:1724-1727, (1978);
Z. Kunszt, Z. Trocsanyi and W. J. Stirling, *Phys. Lett.*, **B 271**:247, (1991).

[64] R. Hamberg, W. L. van Neerven and T. Matsuura, *Nucl. Phys.*, **B 359**:343-405, (1991);
J. Ohnemus and W. J. Stirling, *Phys. Rev.*, **D 47**:2722-2729, (1993);
O. Brein, A. Djouadi and R. Harlander, *Phys. Lett.*, **B 579**:149-156, (2004).

[65] M. L. Ciccolini, S. Dittmaier and M. Krämer, *Phys. Rev.*, **D 68**:073003, (2003).

[66] O. Brein *et al.*, *arXiv:hep-ph/0402003*.

[67] R. Raitio and W. W. Wada, *Phys. Rev.*, **D 19**:941, (1979);
J. N. Ng and P. Zakarauskas, *Phys. Rev.*, **D 29**:876, (1984);
Z. Kunszt, *Nucl. Phys.*, **B 247**:339, (1984);
J. F. Gunion, *Phys. Lett.*, **B 261**:510-517, (1991);
W. J. Marciano and F. E. Paige, *Phys. Rev. Lett.*, **66**:2433-2435, (1991).

[68] W. Beenakker *et al.*, *Phys. Rev. Lett.*, **87**:201805, (2001);
W. Beenakker *et al.*, *Nucl. Phys.*, **B 653**:151-203, (2003);
L. Reina and S. Dawson, *Phys. Rev. Lett.*, **87**:201804, (2001);
S. Dawson, L. H. Orr, L. Reina, and D. Wackeroth, *Phys. Rev.*, **D 67**:071503, (2003).

[69] Z. Kunszt, *Nucl. Phys.*, **B 247**:339, (1984);
W. J. Marciano and F. E. Paige, *Phys. Rev. Lett.*, **66**:2433, (1991);
J. F. Gunion, *Phys. Lett.*, **B 261**:510, (1991);
E. Richter-Was and M. Sapinski, *Acta Phys. Polon.*, **B u30**:1001, (1999);
V. Drollinger, T. Müller and D. Denegri, arXiv:hep-ph/011131;
J. Cammin and M. Schumacher, ATL-PHYS-2003-024.

[70] G. L. Bayatian *et al.* [CMS Collaboration], *J. Phys.*, **G**:34-95, (2007);
G. Aad *et al.* [The ATLAS Collaboration], arXiv:0901.0512 [hep-ex].

[71] T. Plehn, G. P. Salam, M. Spannowsky, *Phys.Rev.Lett.*, **104**:111801, (2010);
A. Abdesselam *et al.*, *Eur.Phys.J.*, **C 71**:1661, (2011).

[72] L. Resnick, M. K. Sundaresan and P. J. S. Watson, *Phys. Rev.*, **D 8**:172, (1973).

[73] J. Fleisher and F. Jegerlehner, *Phys. Rev.*, **D 23**:2001, (1981);
B. A. Kniehl, *Nucl. Phys.*, **B 376**:3, (1992).

[74] A. Djouadi, M. Spira and P.M. Zerwas, *Z.Phys.*, **C70**:427-434, (1996);
A. Djouadi and P. Gambino, *Phys. Rev.*, **D 53**:4111(E), (1996).

[75] K. G. Chetyrkin, B. A. Kniehl and M. Steinhauser, *Nucl. Phys.*, **B 490**:19-39, (1997);
K. G. Chetyrkin, B. A. Kniehl and M. Steinhauser, *Phys. Rev. Lett.*, **78**:594-597, (1997).

[76] J. M. Butterworth, A. R. Davison, M. Rubin and G. P. Salam, *arXiv:hep-ph/0810.0409v1*, **ICHEP08**, (2008).

[77] A. Djouadi, *Phys. Rep.*, **459**:1, (2008).

[78] A. I. Vainshtein, M. B. Voloshin, V. I. Zakharov and M. A. Shifman, *Sov. J. Nucl. Phys.*, **30**:711, (1979).

[79] A. Djouadi, M. Spira and P.M. Zerwas, *Phys. Lett.*, **B257**:187, (1991); *Phys. Lett.*, **B311**:255, (1993).

[80] M. Steinhauser. In B. A. Kniehl (World Scientific), editor, *Proceedings of the Ringberg Workshop*, (1996).

[81] L. Bergstrom and G. Hult, *Nucl. Phys.*, **B 259**:137, (1985);
M. Spira, A. Djouadi and P. M. Zerwas, *Phys. Lett.*, **B 276**:350, (1992).

[82] M. Spira, *Fortsch. Phys.*, **46**:203, (1998).

[83] B. W. Lee, C. Quigg and H. B. Thacker, *Phys. Rev.*, **D 16**:1519, (1977).

[84] B. A. Kniel and M. Steinhauser, *Phys. Lett.*, **B 365**:297, (1996).

[85] A.Bredenstein, A.Denner, S.Dittmaier and M.M.Weber, *Phys. Rev.*, **D 74**:013004, (2006);
A.Bredenstein, A.Denner, S.Dittmaier and M.M.Weber, *Nucl. Phys. Proc. Suppl.*, **160**:131, (2006);
A.Bredenstein, A.Denner, S.Dittmaier and M.M.Weber, *JHEP*, **0702**:080, (2007).

[86] A. Djouadi, *Phys. Rep.*, **457**:1, (2008).

[87] The ATLAS Collaboration, G. Aad *et al.*, *arXiv:hep-ex/0901.0512*.

[88] CDF and DØ Collaborations, *Phys.Rev.Lett.*, **104**:061802, (2010).

[89] L3 Collaboration, *Phys. Lett.*, **B 248**:227, (1990).

[90] S. Catani and M. Grazzini, *Phys. Rev. Lett.*, **98**:222002, (2007);
M. Grazzini, *JHEP*, **02**:043, (2008).

[91] `http://theory.fi.infn.it/grazzini/codes.html`

[92] ATLAS collaboration, Tecnhical design report, *CERN-LHCC*/99-15, (1999); CMS collaboration, Tehcnical report, *CERN-LHCC*/94-38, (1994).

[93] S. Abdullin, M. Dubinin, V. Ilyin, D. Kovalenko, V. Savrin and N. Stepanov, *Phys. Lett.*, **B 431**:410, (1998).

[94] G. Davatz, G. Dissertori, M. Dittmar, M. Grazzini and F. Pauss, *JHEP*, **0405**:009, (2004).

[95] S. Dawson and R. Kauffman, *Phys. Rev. Lett.*, **68**:2273, (1992); C. Schmidt, *Phys. Lett.*, **B 413**:391, (1997).

[96] D. de Florian, M. Grazzini and Z. Kunszt, *Phys. Rev. Lett.*, **82**:5209, (1999).

[97] V. Ravindran, J. Smith and W. L. Van Neerven, *Nucl. Phys.*, **B 634**:247, (2002); C. J. Glosser and C. R. Schimdt, *JHEP*, **0212**:016, (2002) .

[98] C. J. Glosser, *Ph.D. Thesis*, *arXiv:hep-ph/0201054*.

[99] Y. L. Dokshitzer, D. Diakonov and S. I. Troian, *Phys. Rept.*, **58**:269, (1980).

[100] G. Parisi and R. Petronzio, *Nucl. Phys.*, **B 154**:427, (1979).

[101] J. C. Collins, D. Soper and G. Sterman, *Nucl. Phys.*, **B 250**:199, (1985).

[102] J. Kodaira and L. Trentadue, *Phys. Lett.*, B 112:66, (1982).

[103] C. T. Davies and W. J. Stirling, *Nucl. Phys.*, **B 244**:337, (1984).

[104] S. Catani and M. Grazzini, *Nucl. Phys.*, B 845:297-323, (2011).

[105] C. Balazs, E. L. Berger, P. M. Nadolsky and C. P. Yuan, *Phys. Rev.*, **D**:76-013009 (2007).

[106] A. Vogt, *Phys. Lett.*, **B 497**:228, (2001).

[107] C. Berger, *Phys. Rev.*, **D 66**:116002, (2002).

[108] S. Moch, A. Vogt and J. Vermaseren, *Nucl. Phys.*, **B 688**:01-134, (2004); *Nucl. Phys.*, **B 691**:129-181, (2004).

[109] C. Balazs, J. -w. Qiu and C. P. Yuan, *Phys. Lett.*, **B 355**:548, (1995).

[110] C. Balazs and C. P. Yuan, *Phys. Rev.*, **D 56**:5558, (1997).

[111] R. Brock, F. Landry, P. Nadolshy and C. P. Yuan, *Phys. Rev.*, **D 67**:073016, (2003)

[112] C. Balazs and C. P. Yuan, *Phys. Lett.*, **B 478**:192, (2000).

[113] Q. -H. Cao, C. -R. Chen, C. Schmidt and C. -P. Yuan, arXiv:0909.2305 [hep-ph].

[114] C. Balazs and C. P. Yuan, *Phys. Rev.*, **D 59**:114007, (1999); [Erratum-ibid. **D 63**:059902, (2001)].

[115] C. Balazs, P. M. Nadolsky, C. Schmidt and C. P. Yuan, *Phys. Lett.*, **B 489**:157, (2000).

[116] K. Ellis and S. Veseli, *Nucl. Phys.*, **B 511**:649, (1998);
A. Kulesza and J. Stirling,*Nucl. Phys.*, **B 555**:279, (1999).

[117] M. Dasgupta and G. P. Salam, *Eur. Phys. J.*, **C24**:213, (2002); *JHEP*, **0208**:032, (2002).

[118] S. Catani, L. Trentadue, G. Turnock and B. R. Webber, *Nucl. Phys.*, **B 407**:3, (1993).

[119] J. C. Collins and D. Soper, *Nucl. Phys.*, **B 193**:381, (1981).

[120] G. A. Ladinsky and C. P. Yuan, *Phys. Rev.*, **D 50**:4239, (1994).

[121] A. Kulesza and W. J. Stirling, *JHEP*, **0312**:056, (2003).

[122] A. Kulesza, G. Sterman and W. Vogelsang, *Phys. Rev.*, **D 66**:014011, (2002).

[123] S. Catani, M. L. Mangano, P. Nason and L. Trentadue, *Nucl. Phys.*, **B 478**:273 (1996);
E. Laenen, G. Sterman and W. Vogelsang, *Phys. Rev. Lett.*, **84**:4296, (2000).

[124] G. Bozzi, S. Catani, D. de Florian and M. Grazzini, *Nucl.Phys.*, **B 791**:1-19, (2008).

[125] S. Catani and L. Trentadue, *Nucl. Phys.*, **B 327**:323, (1989), *Nucl. Phys.*, **B 353**:183, (1991).

[126] H. Kawamura, J. Kodaira and K. Tanaka, *Nucl.Phys.*, **B 777**:203-225, (2007).

[127] G. Sterman and W. Vogelsang, *JHEP*, **0102**:016, (2001).

[128] T. Sjöstrand, S. Mrenna, P. Skands, *JHEP*:05-0.26, (2006).

[129] G. Corcella, I.G. Knowles, G. Marchesini, S. Moretti, K. Odagiri, P. Richardson, M.H. Seymour and B.R. Webber, *JHEP*,**0101**:010, (2001);
G. Marchesini, B.R. Webber, G. Abbiendi, I.G. Knowles, M.H. Seymour and L. Stanco, *Computer Phys. Commun.*, **67**:465, (1992).

[130] P. Nason, *JHEP*, **0411**:040, (2004);
S. Frixione, P. Nason and C. Oleari, *JHEP*, **0711**:070, (2007);
S. Alioli, P. Nason, C. Oleari and E. Re, *JHEP*, **1006**:043, (2010).

[131] S. Frixione and B.R. Webber, *JHEP*, **0206**:029, (2002).

[132] Higgs Working Group Summary Report, arXiv:0803.1154v1 [hep-ph].

[133] S. Catani and B.R. Webber, *JHEP*, **9710**:005, (1997).

[134] G. Bozzi, S. Catani, G. Ferrera, D. de Florian and M. Grazzini, *Nucl. Phys.*, **B 815**:174, (2009);
G. Bozzi, S. Catani, G. Ferrera, D. de Florian, M. Grazzini, *Phys. Lett.*, **B 696**:207, (2011).

[135] M. Grazzini, *JHEP*, **0601**:095, (2006).

[136] R. Frederix and M. Grazzini, *Phys. Lett.*, **B 662**:353, (2008).

[137] G. Bozzi, B. Fuks and M. Klasen, *Phys. Rev.*, **D 74**:015001, (2006).

[138] H. Kawamura, J. Kodaira, H. Shimizu and K. Tanaka, *Prog. Theor. Phys.*, **115**:667, (2006);
H. Kawamura, J. Kodaira and K. Tanaka, *Nucl. Phys.*, **B 777**:203, (2007); *Prog. Theor. Phys.*, **118**:581, (2007); *Phys. Lett.*, **B 662**:139, (2008).

[139] S. Catani and M. Grazzini, arXiv:1106.4652 [hep-ph].

[140] J. Blümlein, *Comput. Phys. Commun.*, **133**:76-104, (2000);
J. Blümlein and S. Kurth, *Phys. Rev.*, **D 60**:014018, (1999);
J. Blümlein and V. Ravindran, *Nucl. Phys.*, **B 716**:128, (2005);
J. Blümlein and S. O. Moch, *Phys. Lett.*, **B 614**:53, (2005).

[141] Maple V, *Release 5*, Waterloo Maple Inc.; `mathematica 3.0`, Wolfram Research Inc.

[142] Baur, U., Glover, E. W. N. and van der Bij, *Nuclear Physics*, **B 318**: 106-136, (1989).

[143] H. -L. Lai, M. Guzzi, J. Huston *et al.*, *Phys. Rev.*, **D 82**:074024, (2010);
R. D. Ball, L. Del Debbio, S. Forte *et al.*, *Nucl. Phys.*, **B 838**:136, (2010);
F. D. Aaron *et al.* [H1 Collaboration], *Eur. Phys. J.*, **C 64**:561, (2009).

[144] S. Alekhin, J. Blumlein, S. Klein, S. Moch, *Phys. Rev.*, **D 81**:014032, (2010).

[145] P. Jimenez-Delgado, E. Reya, *Phys. Rev.*, **D 80**:114011, (2009).

[146] R. D. Ball *et al.* [The NNPDF Collaboration], arXiv:1107.2652 [hep-ph].

[147] Y. L. Dokshitzer, D. Diakonov and S. I. Troian, *Phys. Lett.*, **B 79**:269, (1978).

[148] G. Watt, arXiv:1106.5788 [hep-ph].

[149] D. Davatz, G. Dissetori, M. Dittmaier, M. Grazzini and F. Pauss, *JHEP*, **0405**:009, (2004).

[150] CMS collaboration, *CMS Physics*, Technical Design Report, Vol. II Physics Performance, report CERN/LHCC 2006-021.

[151] C. Anastasiou, K. Melonikov and F. Petriello, *Phys. Rev. Lett.*, **93**:262002, (2004);
Nucl. Phys., **B 724**:197, (2005).

[152] M. Grazzini, *JHEP*, **0802**:043, (2008).

[153] M. Dittmar and H. K. Dreiner, *Phys. Rev.*, **D 55**:167, (1997).

[154] Numerical Recipes: The Art of Scientific Computing. Third Edition (2007), Cambridge University Press ISBN-10: 0521880688.

[155] G.P. Lepage, *Journal of Computational Physics*, **27**:192-203, (1978);
G.P. Lepage, *Cornell preprint*, **CLNS 80**:447, (1980).

Cover image

Real CMS proton-proton collision, candidate ZZ event, in which one Z decays to two electrons (red towers) the other to two muons (red lines): candidate event in the Standard Model Higgs Search using 2010 and 2011 data. The event shows characteristics expected from the decay of a Higgs boson, but is also consistent with background Standard Model physics processes.

Ringraziamenti

In primis vorrei ringraziare Massimiliano, per vari motivi. E' stato il mio mentore scientifico e si è prodigato molto nella correzione di questa tesi, mi ha consentito di partecipare a molte scuole e conferenze permettendomi quindi di inserirmi nella comunità scientifica nella quale lavoro. Ma il motivo principale per cui lo ringrazio, è che mi ha sempre considerato prima di tutto una *persona*. Temo sia difficile spiegare il senso profondo di questa mia affermazione, ma chi ha orecchie per intendere spero capirà.

Vorrei ringraziare Giancarlo, amico che mi ha pazientemente sopportato, e spiegato un mare di cose in fisica e codici che faticavo a comprendere. In certe situazioni avrei voluto eleggerlo santo... Anche lui ha contribuito molto e in maniera diretta alla realizzazione di questa tesi.

Devo poi ringraziare molti amici che con il loro affetto mi hanno sempre sostenuto. In particolare Francesco, Giovanni, Antonio e Massimo, sono stati così gentili da aiutarmi fin da subito: è bello ricevere aiuto da amici nel momento del bisogno, ma loro si sono offerti di aiutarmi *prima ancora di conoscerci* bene e questo vale moltissimo. Massimo devo ringraziarlo pure per i numerosi aiuti in ambito informatico. Ringrazio Dario, anche per gli infiniti suggerimenti nelle traduzioni in inglese, e Alessandra: se non fosse stato per lei, neanche avrei cominciato questo dottorato.

Infine ringrazio, anche per le varie seratone trascorse assieme, Orlando e le polacche, Stefano e la Divina Commedia, Azzurra, Spino e la piazza-piazza, *la* Vale e gli zuccherini, Leonardo e le degustazioni, Anselmo e il cocchino, Riccardo e il pollo arrosto, e Pedro.

Ora, dopo aver scritto cento e passa pagine di tesi con la massima serietà e concentrazione possibili, consentitemi di concludere con un paio di righe di delirio, le devo proprio mettere. Chiedo perdono...

```
.--. . .-.  -- . .-.-.- .-.-.- .-.-.-
.-.. .-  -- .- - . .-. .. .-  --- ... -.-. ..- .-. .- .-.-.- .-.-.- .-.-.-
. .----.  ..- -. .-  -.-. .- --. .- - .-  .--. .- --.. --.. . ... -.-. .- -.-.--

----. ..---  -- .. -. ..- - ..  -.. ..  .- .--. .--. .-.. .- ..- ... .. -.-.--
```